



# VCU

Virginia Commonwealth University  
VCU Scholars Compass

---

Theses and Dissertations

Graduate School

---

2017

## Growth of Zn-polar BeMgZnO/ZnO heterostructure with two dimensional electron gas (2DEG) and fabrication of silver Schottky diode on BeMgZnO/ZnO heterostructure.

Md Barkat Ullah  
*Virginia Commonwealth University*

Follow this and additional works at: <https://scholarscompass.vcu.edu/etd>



Part of the [Electronic Devices and Semiconductor Manufacturing Commons](#)

© Md Barkat Ullah

---

Downloaded from

<https://scholarscompass.vcu.edu/etd/4992>

This Dissertation is brought to you for free and open access by the Graduate School at VCU Scholars Compass. It has been accepted for inclusion in Theses and Dissertations by an authorized administrator of VCU Scholars Compass. For more information, please contact [libcompass@vcu.edu](mailto:libcompass@vcu.edu).

© Md Barkat Ullah 2017

All Rights Reserved

**Growth of Zn-polar BeMgZnO/ZnO heterostructure with two dimensional  
electron gas (2DEG) and fabrication of silver Schottky diode on  
BeMgZnO/ZnO heterostructure**

A dissertation submitted in partial fulfillment of the requirements for the degree of Doctor of  
Philosophy in Electrical and Computer Engineering at Virginia Commonwealth University.

by

Md Barkat Ullah

Major Director: Dr. Hadis Morkoç,  
Professor, Electrical and Computer Engineering

Virginia Commonwealth University

Richmond, Virginia

August 2017

## Acknowledgement

First of all, I would like to express my gratitude to my advisor, Professor Hadis Morkoç. It has been a lifetime privilege to have been supervised by him. Without his invaluable help, guidance, comments, and critiques with his profound knowledge in nitride and oxide semiconductors, this thesis would not have been possible. I am very much thankful to him for all the efforts that he has made for my personal development as a researcher. Words fail to express my gratitude towards him for changing my life in every aspects.

I am also grateful to Professor Ümit Özgür not only for his valuable suggestions and constant support but also for his exceptional ability to elucidate any complex topic. I am also very much thankful to Prof. Vitaliy Avrutin for his help and guidance during the research. This thesis wouldn't be complete without his endless help and thoughtful discussion. I also appreciate the helpful comments and suggestions from my other committee members, Prof. Shiv Khanna and Prof. Michael Reshchikov.

I have a deep appreciation to Professor Pierre Ruterana, CNRS, France, for his remarkable help to realize the polarity inversion of ZnO. I'm also thankful to Dr. Emilis Šermukšnis for his invaluable noise and CV measurements and discussions over the email. I would also like to acknowledge Dr. Janos Volk, Hungary, for his encouragement during this time.

I am grateful to my colleague, Dr. Mykyta Toporkov and Dr. Romualdo Ferreyra, for their mentoring and guidance in semiconductor growth and fabrication. I would like to acknowledge

Dr. Kai Ding, and Dr. Natalia Izyumskaya, Tanner Nakagawara, Dr. Shopan Hafiz, without whose help I most likely would not been able to finish most of my experiments.

I would like to thank U.S. Air Force Office of Scientific Research for the financial support without which I would not have been able to perform the research in VCU. Again, I'm thankful to my advisor Professor Hadis Morkoç and VCU for maintaining the financial support and collaborations.

Finally, and most importantly, I would like to thank my parents, siblings and friends for their love, support and motivation. I would like to acknowledge my fellow Bangladeshi graduate students in VCU, especially Dilip K. Paul and Lamia Nahar, who supported me in a number of ways to focus on my research.

## Table of Contents

List of Figures .....	vii
List of Tables .....	xii
Abstract .....	ii
Executive summary.....	xv
Chapter 1. Introduction.....	19
1.1 Growth of ZnO by Molecular Beam Epitaxy:.....	21
1.2 Polarity consideration of ZnO:.....	23
1.3 ZnO based ternaries and quaternary:.....	25
1.4 ZnO based heterostructures with Two Dimensional Electron gas (2DEG): .....	28
1.5 Metal-semiconductor Schottky diode: .....	33
1.5.1 Schottky-Mott model: .....	33
1.5.2 Image force lowering: .....	36
1.5.3 Thermionic field emission: .....	36
1.5.4 Recombination: .....	37
1.5.5 Schottky barrier inhomogeneity:.....	38
1.6 Organization of this thesis.....	39
Chapter 2. Polarity control of ZnO on (0001) GaN/sapphire template .....	41
2.1 Introduction: .....	41
2.2 Growth technique: .....	42

2.3	Polarity control of ZnO on GaN: .....	43
2.4	Strain control of ZnO on GaN:.....	47
Chapter 3. Quaternary BeMgZnO by P-MBE .....		51
3.1	Introduction: .....	51
3.2	O-polar BeZnO and BeMgZnO on c-sapphire.....	53
3.3	Growth kinetics of O-polar BeMgZnO on (0001) GaN/sapphire template .....	55
3.3.1	Growth kinetics of BeMgZnO at temperature range 450° -500 °C:.....	56
3.3.2	Thermodynamic limitation of Mg and Be incorporation:.....	66
Chapter 4. Zn polar BeMgZnO / ZnO heterostructure with 2DEG:.....		70
4.1	Introduction: .....	70
4.2	Calculation of sheet carrier density:.....	72
4.3	Experimental results:.....	75
Chapter 5. Electrical characterization of BeMgZnO/ZnO heterostructure.....		79
5.1	Schottky diode on BeMgZnO: .....	79
5.1.1	Fabrication of Ag/Be <sub>0.02</sub> Mg <sub>0.26</sub> ZnO Schottky diode: .....	82
5.1.2	Temperature dependent properties of BeMgZnO Schottky Diodes: .....	86
5.2	Capacitance-voltage (CV) measurement and carrier confinement of two dimensional electron gas:.....	95
5.3	Hot electron energy relaxation time: .....	99
Chapter 6. Conclusion .....		102

List of Reference.....	105
Vita.....	111



## List of Figures

Figure 1: Growth rate of ZnO layers against Zn beam flux. <sup>25</sup> .....	23
Figure 2: Schematic of atomic arrangement of ZnO on c-plane sapphire with (a) a 1-nm-thick MgO buffer layer, and with (b) an MgO buffer layer thicker than 3 nm <sup>30</sup> .....	24
Figure 3: Bandgap versus a lattice parameter for group-IIA oxides.....	26
Figure 4: Cross-sectional view of heterojunction field effect transistor. Two dimensional electron gases form at the interface. The bandgap of the barrier has to be higher compared to the channel layer to confine the electron at the interface .....	29
Figure 5: The ball-and stick diagram of a ZnO tetrahedron with a homogeneous in-plane tensile strain showing a net polarization in the opposite (left) and along (right) the growth direction for Zn polar and O polar material.....	30
Figure 6: The ball-and-stick diagram of a ZnO tetrahedron with a homogeneous in-plane tensile (left) and compressive (right) strain showing a net polarization in the [000-1] and [0001] directions, respectively. ....	31
Figure 7: Strain in the Be <sub>x</sub> Mg <sub>y</sub> Zn <sub>1-x-y</sub> O layer on ZnO template as a function of Be and Mg contents. The negative and positive signs represent the compressive and tensile strain, respectively. ....	32
Figure 8 A metal n-type semiconductor pair before (a) and after (b) contact with no surface/interface states. The metal work function is greater than that for the semiconductor ( $\phi_m$ 34	
Figure 9: Band diagram in two dimensions of an inhomogeneous Schottky contact under an applied forward bias V.....	38

Figure 10 Growth rate of ZnO films as a function of VI/II ratio during LT-ZnO growth. The solid curve is a guide to the eye..... 44

Figure 11 :  $5\ \mu\text{m} \times 5\ \mu\text{m}$  AFM images of (a) O polar and (b) Zn polar ZnO. (c) and (d) show the respective images for  $1\ \mu\text{m} \times 1\ \mu\text{m}$  area..... 45

Figure 12: (a) Weak beam TEM micrograph,  $g=0002$ , and (b) HAADF image of ZnO/GaN heterointerface of the sample nucleated with VI/II = 6.0. The dots represent the Ga and Zn atoms in GaN and ZnO lattice respectively. The line represents the change in stacking sequence in GaN and ZnO lattice. Bright vertical lines in the weak beam image (a) are threading dislocations propagating from GaN. .... 47

Figure 13: (a) Semi-logarithmic plot of XRD triple axis  $2\theta-\omega$  diffraction patterns along the [0002] direction. From bottom to top, VI/II ratio in the LT-ZnO layer increases from 0.55 to 3.0 at a constant Zn flux of  $J_{\text{Zn}} = 0.1\ \text{\AA}/\text{s}$ . Dash line represents the Bragg angle for bulk ZnO in [0002] direction. Solid circles indicate the ZnO peak positions. Residual strain (b) measured along the c direction and (b) calculated in the biaxial plane of ZnO as a function of VI/II ratio during LT-ZnO growth. The negative and the positive sign in y-axis denote the compressive and tensile residual strain, respectively. Straight lines are used to guide the eye. .... 48

Figure 14: Bandgap vs a lattice parameter for BeMgZnO, BeZnO and MgZnO. Dashed lines are linear interpolation between wurtzite binaries..... 52

Figure 15:(a) Cross-sectional TEM image of  $\text{Be}_{0.10}\text{Zn}_{0.90}\text{O}/\text{ZnO}$  structure. (b) Stacking faults and possible second-phase inclusions and (c) high-angle grain boundaries..... 54

Figure 16: (a) Cross-sectional TEM image of  $\text{Be}_{0.07}\text{Mg}_{0.30}\text{Zn}_{0.63}\text{O}/\text{ZnO}$  structure showing a large density of threading dislocations ( $\sim 10^{10} \text{ cm}^{-2}$ ). (b) HRXRD  $2\theta$ - $\omega$  scans of 0002 reflection from  $\text{Be}_{0.10}\text{Zn}_{0.90}\text{O}/\text{ZnO}$  and  $\text{Be}_{0.07}\text{Mg}_{0.30}\text{Zn}_{0.63}\text{O}/\text{ZnO}$  structures. .... 55

Figure 17: The Double axis  $2\theta$ - $\omega$  scans of the 0002 reflection for the samples grown using different Zn to Be and Mg flux ratios at (a) 475 °C and (b) 500 °C compared with that for reference sample A, which was grown at 450 °C. Figure (c) shows the triple axis scan of the single crystalline BeMgZnO grown at temperature range 450 °C to 500 °C. .... 60

Figure 18: Left and right column shows the RHEED image taken along [1-100] azimuthal direction after 20 min and 60 min growth of  $\text{Be}_x\text{Mg}_y\text{Zn}_{1-x-y}\text{O}$  respectively. Figure (a) & (b) are for the sample A grown at  $T_g = 450$  °C, figure (c) to (h) are for  $T_g = 475$  °C (samples B1, B2, and B3) and figure (i) to (n) are for  $T_g = 500$  °C (samples C1, C3, and C4). Zn to (Be + Mg) flux ratios ( $J_r$ ) are indicated on each figure. .... 65

Figure 19: 15 K PL spectra from quaternary samples grown at (a) 475°C and (b) 500°C along with reference sample A grown at 450°C. As examples, insets show the deconvolution of spectra into three Gaussian peaks for (a) sample B2 and (b) sample C2. Figure (c) shows the effect of Zn / (Be + Mg) ratio on the integrated intensity of different emission peaks. Rectangular and circular symbols represent series B and series C samples, respectively. Solid lines are used as guides to the eye ..... 67

Figure 20: Polarization induced sheet charge density and directions of the piezoelectric and spontaneous polarization of Zn polar (a) BeMgZnO / ZnO, (b) MgZnO / ZnO and O-polar (c) ZnO / BeMgZnO, (d) ZnO/ MgZnO heterostructure ..... 73

Figure 21: Calculated 2DEG sheet charge density of Zn-polar HFET structures with  $\text{Be}_x\text{Mg}_y\text{Zn}_{0.97-y}\text{O}$  with  $x = 0-3$  and  $\text{Mg}_y\text{Zn}_{1-y}\text{O}$  barriers as a function of Mg composition. .... 75

Figure 22: Hall-effect measurement of (a) electron mobility and (b) sheet concentration of two dimensional electron gas for  $\text{Be}_x\text{Mg}_y\text{ZnO}/\text{ZnO}$  samples shown in Table I over the temperature range from 13K to 293K. .... 77

Figure 23: Comparison 2DEG sheet carrier density determined for Zn-polar  $\text{Be}_x\text{Mg}_y\text{Zn}_{1-x-y}\text{O}/\text{ZnO}$  with that in both Zn- (Tampo et al.<sup>88</sup>) and O polar  $\text{Mg}_y\text{Zn}_{1-y}\text{O}/\text{ZnO}$  heterostructures (Ullah et al<sup>98</sup>)..... 77

Figure 24: Free energy of formation per Oxygen atom for variety of metals as a function of metal work function ..... 80

Figure 25: I-V relationship of Ag Schottky diodes on  $\text{Be}_x\text{Mg}_y\text{Zn}_{1-x-y}\text{O}/\text{ZnO}$  samples..... 84

Figure 26: Temperature dependent current-voltage (I-V) measurement of Ag/ $\text{Be}_{0.02}\text{Mg}_{0.26}\text{MgO}$  Schottky diode at temperature range from (a) 80 K to 400K for sample B (b) 85 K to 457 K. for sample C and (c) 300 K-375 K for sample D. .... 87

Figure 27: Temperature dependence of the (a) ideality factor and (b) barrier height for the Ag/ $\text{BeMgZnO}/\text{ZnO}$  Schottky diode..... 88

Figure 28: Barrier height versus  $q/2kT$  plot for Ag/ $\text{Be}_{0.02}\text{Mg}_{0.26}\text{ZnO}/\text{ZnO}$  heterostructure. Mean barrier height and standard deviation were found from the intercept and slop of the straight line. .... 90

Figure 29: Richardson plot (square) of  $\ln J_0 T^2$  vs  $q/kT$  and a modified Richardson plot (circle) of  $\ln J_0 T^2 - q^2 \sigma^2 / 2kT^2$  vs  $q/KT$  together with a linear fit to determine ..... 91

Figure 30: Calculated temperature dependence of the ideality factor for the case when the current through the junctions is dominated by the TFE with characteristic energy values  $E_{00}$  according to equation 24 (solid lines) for the Ag/BeMgZnO studied. The filled circles show the experimental temperature dependence values of the ideality factor obtained from I–V characteristics given in Figure 27(a)..... 93

Figure 31: Calculated I-V-T curves using the TFE/FE model (dashed line) for  $E_{00} = 50$  meV obtained from Figure 30. Solid line shows the experimentally found I-V-T curves. .... 94

Figure 32: C-V concentration profile of  $N_{C-v}$  vs penetration depth of  $Be_xMg_yZnO/ZnO$  heterostructure shown in Table..... 97

Figure 33: The dependence of excess noise temperature on power per electron for BeMgZnO/ZnO heterostructure with 2DEG ..... 99

Figure 34: Electron energy relaxation time versus electron density per unit volume (blue symbol- GaN based 2DEG, green symbol-BeMgZnO/ZnO heterostructure with 2DEG, brown symbol- bulk ZnO)..... 100

## List of Tables

Table I: $\text{Be}_x\text{Mg}_y\text{Zn}_{1-x-y}\text{O}$ growth temperature ( $T_g$ ), Zn ( $J_{\text{Zn}}$ ), Mg ( $J_{\text{Mg}}$ ), and Be ( $J_{\text{Be}}$ ) metal fluxes and their ratios, $J_r = \frac{J_{\text{Zn}}}{(J_{\text{Be}} + J_{\text{Mg}})}$ and growth rate of the quaternary samples included in this study.....	57
Table II: c lattice parameters, energy (EPL) of the dominant PL peak measured at 15 K, optical bandgaps ( $E_g$ ) and Be and Mg compositions for the crystalline $\text{BeMgZnO}$ samples .....	61
Table III: Comparison of c lattice parameters, PL emission energies and optical bandgaps of the crystalline $\text{Be}_{0.03}\text{Mg}_y\text{Zn}_{0.97-y}\text{O}$ alloys discussed here with relevant reported $\text{MgZnO}$ thin films of similar Mg composition.....	62
Table IV: a lattice parameters, elastic (C) and piezoelectric (e) constants, spontaneous polarization (PSP) of $\text{BeO}$ , $\text{MgO}$ and $\text{ZnO}$ .....	74
Table V: Structure parameters and electronic properties of $\text{Be}_{0.02}\text{Mg}_y\text{ZnO}/\text{ZnO}$ heterostructure for sample A, B and C .....	76
Table VI: $\text{Be}_x\text{Mg}_y\text{Zn}_{1-x-y}\text{O}/\text{ZnO}$ samples studied for Ag Schottky diode with their electron mobility, 2 DEG sheet carrier concentration, Schottky contact area, barrier height and ideality factor at room temperature.....	83
Table VII: Effective mass of II-oxides semiconductor and calculated Richardson constant using Eqn 3 .....	85

## Abstract

Title of dissertation: GROWTH OF Zn POLAR BeMgZnO/ZnO HETEROSTRUCTURE WITH TWO DIMENSIONAL ELECTRON GAS (2DEG) AND FABRICATION OF SILVER SCHOTTKY DIODE ON BeMgZnO/ZnO HETEROSTRUCTURE

By Md Barkat Ullah, Ph.D

A dissertation submitted in partial fulfillment of the requirements for the degree of Doctor of Philosophy in Electrical and Computer Engineering at Virginia Commonwealth University.

Virginia Commonwealth University, 2017

Major Director: Dr. Hadis Morkoç, Professor, Electrical and Computer Engineering

This thesis focuses on growth of Zn polar BeMgZnO/ZnO heterostructure on GaN/sapphire template with two dimensional electron gas (2DEG) for the application of UV photodetector/emitter and high speed electronics. The motivation of using BeMgZnO as a barrier layer originates from the need to reach plasmon-LO phonon resonance in order to obtain minimum longitudinal optical (LO) phonon lifetime.

Presence of 2DEG was realized in BeMgZnO/ZnO heterostructure only when the Zn polarity was achieved during the nucleation growth of ZnO on GaN/sapphire template. It was found that, polarity of ZnO on (0001) GaN/sapphire template can be controlled by the oxygen to Zn ratio used during the nucleation growth.

To obtain high structural and optical quality of BeMgZnO quaternary alloy, growth kinetics of BeMgZnO layer has been studied at the temperature range from 450°C-500°C. We have achieved the growth of single crystal Be<sub>0.03</sub>Mg<sub>0.15</sub>ZnO alloy at 500 °C, more than 100°C higher compared to what reported in literature, on the (0001) GaN/sapphire template through the control of Zn/(Be+Mg) flux ratio. We have also observed a thermodynamic limitation of Mg

incorporation into the wurtzite BeMgZnO alloy where the excess Mg adatom accumulated in the growing surface as a MgO rich cluster.

Two dimensional electron gas with high ( $1.2 \times 10^{13} \text{cm}^{-2}$ ) sheet carrier density was achieved at the  $\text{Be}_{0.03}\text{Mg}_{0.41}\text{ZnO}/\text{ZnO}$  interface through strain engineering by incorporating Be into MgZnO ternary alloy. To obtain the similar sheet carrier density it would require above 60% of Mg in MgZnO/ZnO heterostructure with reduced structural quality. A systematic comparison of sheet carrier density has been made with the already reported results from Zn polar MgZnO/ZnO heterostructure as well as with the theoretical calculation.

Silver Schottky diode on  $\text{Be}_{0.02}\text{Mg}_{0.26}\text{ZnO}/\text{ZnO}$  heterostructure with barrier height 1.07 eV and ideality factor 1.22 was obtained with 8 order of rectification ratio. The temperature-dependent electrical characteristics were studied by using temperature dependent current-voltage (I-V) measurements. Richardson constant value of  $34.8 \text{ Acm}^{-2}\text{K}^{-2}$  was found experimentally which was close to the theoretical value of  $36 \text{ Acm}^{-2}\text{K}^{-2}$  known for  $\text{Be}_{0.02}\text{Mg}_{0.26}\text{ZnO}$  alloy.



## Executive summary

Zinc oxide (ZnO) based semiconductor materials are highly attractive for a wide range of optical and electronic device applications due to their direct wide bandgap ( $E_g \sim 3.3$  eV for ZnO at 300 K), large excitonic binding energy ( $\sim 60$  meV for ZnO), optical transparency in highly conductive state, and scalability to large volume native substrates. Alloying ZnO with BeO and MgO allows tuning of optical and electronic properties, inclusive of bandgap, band offsets, lattice parameters, and spontaneous polarization. However, compositions, and therefore, tunability achievable in MgZnO and BeZnO ternaries are restricted by limited solubility of BeO and MgO in wurtzite ZnO lattice and the associated phase segregation. Quaternary alloy BeMgZnO alleviates these limitations, and is attractive particularly for solar blind photodetectors, intersubband transition devices, and heterostructures with two-dimensional electron gas (2DEG) as well as light emitting devices. The aim of this thesis is to present the way to control the polarity of ZnO to obtain Zn polar BeMgZnO/ZnO heterostructure with 2DEG and device fabrication of Ag Schottky diode with temperature dependent electrical characterization.

We have achieved polarity control of ZnO grown by plasma assisted molecular beam epitaxy on Ga polar (0001)-GaN/sapphire templates simply via the oxygen-to-Zn (VI/II) ratio during the growth of a thin nucleation layer at 300 °C. Following Zn pre-exposure, the ZnO layers nucleated with low VI/II ratios ( $< 1.5$ ) exhibited Zn-polarity. Those nucleated with VI/II ratios above 1.5, exhibited O-polarity. Supported by scanning transmission electron microscopic imaging, we have unequivocally demonstrated that polarity inversion takes place without formation of any vertical inversion domains and within one monolayer of presumably non-stoichiometric GaO<sub>x</sub> formed at the ZnO/GaN interface. A direct correlation between polarity and strain sign of ZnO layers has been found. The Zn-polar ZnO layers were under tensile biaxial

strain, whereas the O-polar material exhibited compressive strain. Moreover, the amount of residual strain varied linearly with VI/II ratio used during the low-temperature nucleation layer growth. Strain control with VI/II ratio has been explained by the potential formation of Zn interstitials.

We investigated the crystal structure, growth kinetics and electrical properties of BeMgZnO/ZnO heterostructures grown by Molecular Beam Epitaxy (MBE). Transmission Electron Microscopy (TEM) studies revealed that incorporation of Mg into the BeZnO solid solution eliminates the high angle grain boundaries that are the major structural defects in ternary BeZnO. The significant improvement of x-ray diffraction intensity from quaternary BeMgZnO alloy compared to ternary BeZnO was attributed to the reduction of lattice strain, which is present in the latter due to the large difference of covalent radii between Be and Zn (1.22 Å for Zn, 0.96 Å for Be). Incorporation of Mg, which has a larger covalent radius of 1.41 Å, reduced the strain in BeMgZnO thin films and also enhanced Be incorporation on lattice sites in the wurtzite lattice. We studied the effect of substrate temperature, in the range from 450 °C to 500 °C, on the required Zn to (Be + Mg) flux ratio for plasma-assisted molecular beam epitaxy growth of O-polar  $\text{Be}_x\text{Mg}_y\text{Zn}_{1-x-y}\text{O}$  on (0001)-GaN/sapphire templates. Achievement of single-crystalline  $\text{Be}_x\text{Mg}_y\text{Zn}_{1-x-y}\text{O}$  with improved optical and structural quality required relatively high substrate temperatures which necessitated the Zn to (Be + Mg) flux ratio to be increased from 3.9 at 450 °C to 8.3 at 500 °C. This resulted in a reduction of Mg incorporation from 25% to 15% for a fixed Be content of ~3 %. With increasing Zn to (Be + Mg) ratio, 15 K photoluminescence energy for the dominant emission remained unchanged at around 3.75 eV and 3.55 eV for the samples grown at 475 °C and 500 °C, respectively. These findings readily suggest a thermodynamic limitation of Mg and Be incorporation into wurtzite  $\text{Be}_x\text{Mg}_y\text{Zn}_{1-x-y}\text{O}$  lattice,

resulting in the formation of second phase due mainly to the enhanced surface mobility of Mg adatoms, and therefore, an increase in the probability of the formation of Mg-rich clusters. Increase in the in-plane lattice parameter, deduced from the Reflection High Energy Electron Diffraction, at the onset of the phase segregation suggests formation of the wurtzite phase MgO rich alloy(s).

We have demonstrated both theoretically and experimentally that the incorporation of Be into the barrier in Zn-polar BeMgZnO/ZnO and O-polar ZnO/BeMgZnO polarization doped heterostructures allows the alignment of piezoelectric polarization vector with that of spontaneous polarization due to the change of strain sign, thus increasing the amount of net polarization. As a result, a 2DEG concentration of  $1.2 \times 10^{13} \text{ cm}^{-2}$  is achieved in the Be<sub>0.03</sub>Mg<sub>0.41</sub>Zn<sub>0.56</sub>O/ZnO heterostructure. For comparison, a 2DEG concentration of  $7.7 \times 10^{12} \text{ cm}^{-2}$  requires 2% Be and 26% Mg in the barrier, whereas the same in the MgZnO/ZnO system would require incorporation of more than 40% Mg into the barrier, which necessitates very low growth temperatures.

We explored Ag Schottky diode on quaternary BeMgZnO alloys and obtained a Schottky barrier height,  $\Phi_B = 1.07 \text{ eV}$  with an ideality factor  $n=1.22$  for a Ag/Be<sub>0.02</sub>Mg<sub>0.26</sub>ZnO circular Schottky diodes. Rectification ratio as high as 8 orders of magnitude has been obtained. Plasma exposure time, plasma power and oxygen flow rate has been optimized for surface treatment before depositing 50 nm of Ag Schottky metal. The temperature-dependent electrical characteristics of the Ag/Be<sub>0.02</sub>Mg<sub>0.26</sub>ZnO/ZnO heterostructure were studied by using temperature dependent current-voltage (I-V) measurements in the temperature range of 80-457 K. Based on the thermionic emission theory, the ideality factor (n) and the barrier height ( $\Phi_B$ ) were calculated, where the study their temperature dependence has emphasized an inhomogeneity of the barrier

height. The inhomogeneity was explained based on thermionic emission with the assumption of Gaussian distribution. A deviation from the theoretical Richardson constant value was observed which was modified by taking the temperature dependence of barrier height into consideration. The modified Richardson plot gave Richardson constant value of  $34.8 \text{ Acm}^{-2}\text{K}^{-2}$ , close to theoretical value of  $36 \text{ Acm}^{-2}\text{K}^{-2}$  known for  $\text{Be}_{0.02}\text{Mg}_{0.26}\text{ZnO}$ .

## Chapter 1. Introduction

There has been a great deal of interest in zinc oxide semiconductor materials lately. The interest in ZnO is fueled by its prospects in optoelectronics applications owing to its direct wide band gap<sup>1</sup>  $E_g \sim 3.3$  eV at 300 K. Some optoelectronic applications of ZnO overlap with that of GaN, another wide-gap semiconductor  $E_g \sim 3.4$  eV at 300 K which is widely used for production of green, blue-ultraviolet, and white light-emitting devices. However, ZnO has some advantages over GaN among which are the availability of fairly high-quality ZnO bulk single crystals and a large exciton binding energy  $\sim 60$  meV. The large exciton binding energy of  $\sim 60$  meV paves the way for an intense near-band-edge excitonic emission at room and higher temperatures, because this value is 2.4 times that of the room-temperature RT thermal energy  $k_B T = 25$  meV. There have also been a number of reports on laser emission from ZnO-based structures at RT and beyond. It should be noted that besides the above-mentioned properties of ZnO, there are additional properties which make it preferable over other wide-band-gap materials: its high energy radiation stability and amenability to wet chemical etching.<sup>2</sup> Several experiments confirmed that ZnO is very resistive to high-energy radiation,<sup>3,4</sup> making it a very suitable candidate for space applications. ZnO is easily etched in all acids and alkalis, and this provides an opportunity for fabrication of small-size devices.

ZnO has recently found other applications as well, such as fabrication of transparent thin-film transistors, where the protective covering preventing light exposure is eliminated since ZnO-based transistors are insensitive to visible light. Also up to  $2 \times 10^{21} \text{ cm}^{-3}$  charge carriers can be introduced by heavy substitutional doping into ZnO. By controlling the doping level electrical properties can be changed from insulator through n-type semiconductor to metal while maintaining optical transparency that makes it useful for transparent electrodes in flat-panel displays and solar cells and transparent antenna. Recently it has been reported<sup>5</sup> that ZnO heavily doped with gallium (GZO), which can be produced in the form of thin films with conductivity comparable to that of ITO. In order to study the efficacy of GZO transparent antennas, a printed planar-dipole antenna was designed and fabricated. The antenna operated in the 2.4 GHz Industry science and measurement (ISM) band with a return loss of approximately 13 dB.

ZnO also has much simpler crystal-growth technology, resulting in a potentially lower cost for ZnO-based devices. The ZnO bulk crystals have been grown by a number of methods, as has been reviewed recently,<sup>2</sup> and large-size ZnO substrates are available.<sup>6,7</sup> High-quality ZnO thin films can be grown at relatively low temperatures (less than  $700^\circ\text{C}$ ). In order to reduce the strains and dislocation density in epitaxial ZnO and related films, closely lattice-matched substrates are favored for growth. Sapphire substrates are commonly used for ZnO heteroepitaxial growth, primarily on the (0001) orientation (basal or c plane), and also on the (11-20) *a* plane. Single-crystal ZnO films have been grown on sapphire with a high degree of surface flatness, which is essential for device fabrication. The ZnO layers have been grown on sapphire by using a variety of growth techniques, including PLD,<sup>8</sup> MOCVD,<sup>9</sup> and MBE.<sup>10,11</sup> Because of the large lattice mismatch between ZnO ( $a = 0.3250 \text{ nm}$  and  $c = 0.5213 \text{ nm}$ ) and the underlying sapphire ( $a = 0.4754 \text{ nm}$  and  $c = 1.299 \text{ nm}$ ), even after a  $30^\circ$  in-plane rotation to

reduce the mismatch, as-grown ZnO films usually display large mosaicity, high residual carrier concentrations in the  $10^{17}\text{cm}^{-3}$  range, and low mobilities (less than  $100\text{ cm}^2\text{ V}^{-1}\text{ s}^{-1}$  at room temperature) as compared to an electron concentration of  $\sim 10^{15}\text{ cm}^{-3}$  and Hall mobility of  $\sim 200\text{ cm}^2\text{ V}^{-1}\text{ s}^{-1}$  typical for bulk single crystals,<sup>11-13</sup> making their use for optoelectronic applications a challenge. GaN templates on sapphire, owing to their high structural quality, are attractive alternatives for ZnO while offering only a moderate lattice mismatch of 1.8%.

### 1.1 Growth of ZnO by Molecular Beam Epitaxy:

Among the other thin film growth technique, the main advantage of molecular-beam epitaxy (MBE) is its precise control over the deposition parameters and in situ diagnostic capabilities. With the feedback from reflection high-energy electron diffraction (RHEED), the growth mode of ZnO epilayers can be monitored in real time dynamically. For ZnO thin-film deposition by MBE, Zn metal and  $\text{O}_2$  are usually used as the source materials. High-purity Zn metal is evaporated from an effusion cell, where the cell temperature can be varied to examine the effect of the Zn flux on the growth rate and material properties. The oxygen radical beam, which can be generated by a rf plasma source<sup>14</sup>, is directed on the film surface to obtain high-oxidation efficiency. When the O plasma is used, the chamber pressure during growth is in the  $10^{-5}$ -Torr range. The II/VI ratio can be tuned through the Zn cell temperature as well as rf power and  $\text{O}_2$  flow rate of the plasma source. For high-quality ZnO films, the reported growth temperature is in the range of  $350\text{--}650\text{ }^\circ\text{C}$  with a growth rate of  $0.3\text{--}0.7\text{ nm/h}$ .<sup>11,15</sup>

Different surface chemistries of sapphire substrates can lead to different growth modes. The surface chemistry of (11-20)-oriented sapphire was alternated from O rich to Al rich by changing the pregrowth treatment from oxygen plasma to atomic hydrogen.<sup>16</sup> The two-dimensional growth was more favorable and continued longer on a hydrogen treated surface, although the initial two-

dimensional growth was eventually taken over by a three-dimensional growth for both types of pretreatments. A Ga preexposure after H and O pretreatments of the sapphire (0001) surface was adopted by Du et al. just before the ZnO growth in order to eliminate the rotational domain structures.<sup>17</sup> Nitridation of (0001) sapphire substrate was also used to improve the quality of ZnO films grown by plasma-assisted MBE.<sup>18</sup> A very thin nitrogen-polar AlN layer formed by nitridation acted as a template for the following ZnO growth, resulting in the elimination of the rotational domains which were often observed in the films grown without nitridation. On (0001) GaN/sapphire templates, the growth of Zn-polar ZnO has been reported by Hong *et al.* by using Zn pre-exposure whereas O-polar ZnO is grown under the condition of oxygen pre-exposure, the latter of which leads to Ga<sub>2</sub>O<sub>3</sub> formation on GaN<sup>19,20</sup>.

The buffer layer is another critical factor affecting the growth of ZnO layers besides substrates. ZnO growth on sapphire without a buffer layer usually changed from the 2D growth mode to 3D island growth as confirmed by the appearance of a spotty RHEED pattern<sup>15,16,21</sup>. LT buffer layers are usually grown at 250– 350 °C, and the surface morphology of the buffer layer can be improved by thermal treatment at a temperature higher than 700 °C. This is followed by growth on the main ZnO layers at a temperature in the range of 600– 650 °C.<sup>22–24</sup> The growth of ZnO on (0001) GaN substrate will be discussed in more detail in the following chapter. The II/VI ratio has been studied for its effects on the surface morphology and electrical properties. Figure 1 shows the change of growth rate with Zn/O ratio.<sup>25</sup> ZnO thin films with a MgO buffer layer were grown on c-plane sapphire substrate. ZnO layers grown under stoichiometric and O-rich flux conditions show larger hexagonal islands of 3000-nm diameter, whereas those grown under Zn-rich flux conditions show smaller hexagonal islands of 200-nm diameter. The observed surface morphology can be explained by the fact that for growth conducted on the O-polar surface, the



surface diffusion length of Zn adatoms was smaller under the Zn rich condition than under the stoichiometric or O-rich condition.

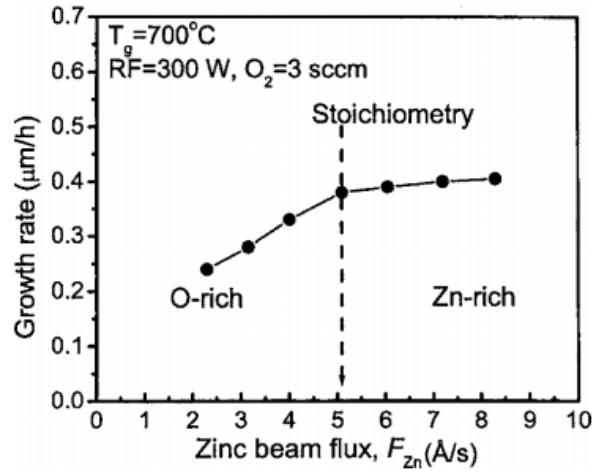


Figure 1: Growth rate of ZnO layers against Zn beam flux.<sup>25</sup>

## 1.2 Polarity consideration of ZnO:

As has been demonstrated in the case of GaN epitaxy,<sup>26–29</sup> the lattice polarity of a wurtzite-structure film has crucial effects on growth processes, material properties, and impurity doping. It is reported that the growth mechanism, surface morphology, and structural properties of ZnO layers show considerable difference between homoepitaxial growths on Zn- and O-polar surfaces. When the film is grown in the [0001] direction, Zn polarity (+c) is obtained and. Likewise when the growth is in the [000-1] direction; O polarity (-c) is obtained. Much effort has been expended to determine the effects of polarity and to find a way of controlling the polarity during growth. Kato *et al*<sup>30</sup> have established polarity control on *c*-plane sapphire by controlling MgO buffer thickness. Prior to the growth substrates are treated at elevated temperatures (800 °C). Control of the polarity of ZnO films grown on *c*-plane sapphire substrates by plasma-assisted MBE was achieved by inserting an MgO buffer layer between the ZnO film and the substrate. The thickness of the MgO buffer is the key for achieving polarity-controlled

ZnO films on nonpolar substrates. The critical thickness in polarity conversion was about 2 nm. MgO growth was Stranski–Krastanov (S–K) mode, and the growth mode transition from 2D to 3D occurred when the layer was thicker than 1 nm. The polarity conversion of ZnO is apparently caused by the difference in atomic structure between the wetting layer and the islands of MgO.

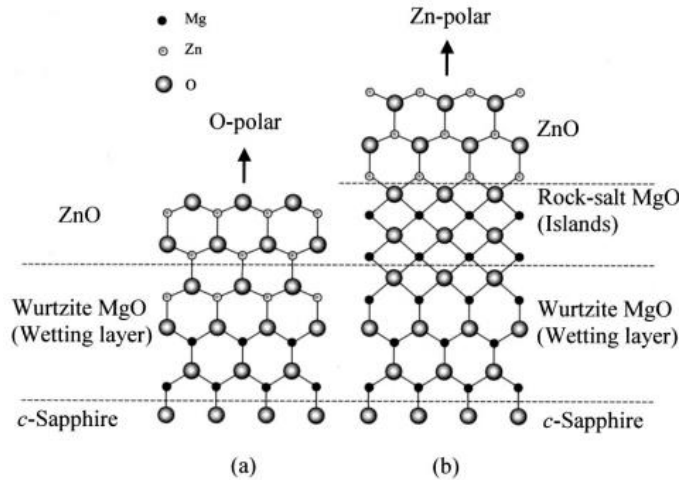


Figure 2: Schematic of atomic arrangement of ZnO on *c*-plane sapphire with (a) a 1-nm-thick MgO buffer layer, and with (b) an MgO buffer layer thicker than 3 nm<sup>30</sup>

Figure 2 shows a schematic of the atomic arrangements of ZnO on *c* sapphire with two types of MgO buffer layers. Because MgO growth occurs under O-rich flux conditions, growth mainly proceeds at the O-terminated surface. In the initial growth stage up to 1 nm, wurtzite MgO as a wetting layer grows on O-terminated sapphire. Because the topmost O atoms in wurtzite MgO have a single dangling bond, each Zn atom in contact with O atoms has three dangling bonds along the *c* axis. As a result, the ZnO film has O polarity. On the other hand, because the MgO wetting layer has compressive strain, the structure changes from wurtzite to rock-salt due to relaxation as the layer thickness increases. Eventually, when the layer thickness exceeds 3 nm, MgO islands with rock-salt structure covers the entire surface. Because the topmost O atoms in

rock-salt MgO have three-dangling bonds, each Zn atom in contact with O atoms has a single dangling bond along the  $c$  axis. As a result, the ZnO film on MgO (111) has Zn polarity.

Although ZnO films grown on sapphire have shown promising electrical and optical properties as discussed above, the crystal quality still needs improvement, since high density of defects are present at the interface and throughout the films as a consequence of a large lattice mismatch (18%) between ZnO and sapphire. On the other hand, GaN is a closely lattice-matched material to ZnO with a lattice mismatch of 1.8%. The control over the ZnO surface polarity has also been achieved on GaN substrates by plasma-assisted MBE.<sup>14,20</sup> Hong *et al*<sup>20</sup> studied the possibility of controlling the ZnO/GaN interface by employing different surface treatment procedures prior to ZnO growth. A treatment of the GaN surface by using Zn- or oxygen-plasma pre-exposures affects the subsequent ZnO growth in different ways. The Zn pretreatment provides a well-ordered GaN surface without any interface layer, while the oxygen-plasma pretreatment results in the formation of a disordered surface due to the formation of a Ga<sub>2</sub>O<sub>3</sub> interface layer. Recently, Ullah *et al*<sup>14</sup> have reported that Zn pre-exposure prior to the growth of ZnO layer does not guarantee Zn polarity material. O-polar ZnO can be grown by using high oxygen to Zn ratio during the nucleation LT ZnO growth although the GaN surface was pre-exposed with Zn. They have controlled the polarity of ZnO by controlling oxygen to Zn ratio during nucleation growth. oxygen to Zn ratio below 1.5 was required for Zn polar ZnO growth.

### **1.3 ZnO based ternaries and quaternary:**

A crucial step in designing modern optoelectronic devices is the realization of band-gap engineering to create barrier layers in High Electron Mobility Transistor (HEMT) and quantum wells in LEDs and laser devices. These heterostructures are composed of layers of different materials/compositions, and the most relevant parameters in this case are the band gaps of each

layer and the valence- and conduction-band offsets between the individual layers. Band-gap engineering in ZnO can be achieved by alloying with MgO, BeO and/or CdO, in analogy to GaN which can be alloyed with AlN and/or InN. Figure 3 shows bandgaps and in-plane lattice parameters for ZnO related family of materials. The solid line and shaded area between binaries in wurtzite phase corresponds to wurtzite ternary and quaternary alloys, respectively.

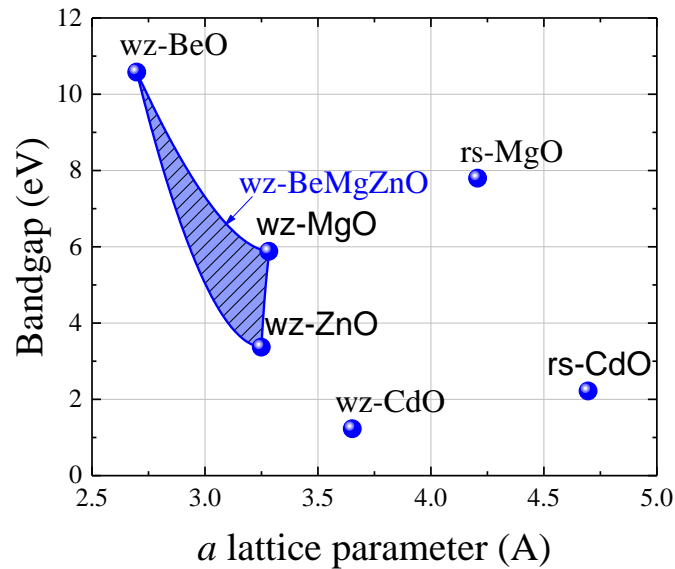


Figure 3: Bandgap versus a lattice parameter for group-IIA oxides

One of the differences between the nitride and the oxide families is that AlN and InN assume the same wurtzite crystal structure of GaN, whereas MgO and CdO assume the rock-salt structure, not the same as the ZnO wurtzite structure. Bandgap of ZnO-based solid solutions can be increased by alloying (Figure 3) with MgO (wurtzite MgO bandgap 5.88 eV)<sup>31</sup> and BeO (10.6 eV)<sup>32</sup>. However, due to the stability of MgO in cubic rock-salt lattice, phase segregation becomes a major obstacle in MgZnO alloy with high Mg content. It should be noted that preserving the wurtzite structure of wide-bandgap material is of critical importance for ZnO-based heterostructures because of large lattice and thermal-expansion mismatch of wurtzite and rock-

salt phases.<sup>33</sup> Although, bandgap tuning up to 4 eV was reported by Ohtomo *et al.*<sup>34</sup> and Sharma *et al.*<sup>35</sup> for 33% - 36% Mg, higher Mg content, and therefore wider bandgap (4.55 eV at 55% Mg<sup>36</sup>) can be achieved only at very low growth temperatures ( $T_g = 250$  °C) at the expense of inferior structural quality and poor stability against thermal treatments. Moreover, for the 4.55eV bandgap, the conduction band offset is still less than 1 eV, which is insufficient for achieving the communication wavelengths using ISBTs.

ZnO-based materials with even wider bandgap are highly desired for solar-blind UV detectors (cut-off wavelength  $< 280$  nm, i.e.  $E_g > 4.5$  eV), devices based on intersubband transitions (ISBTs), and heterojunction field effect transistors (HFET) with two-dimensional electron gas (2DEG). As an alternative to MgZnO, BeZnO was proposed<sup>37</sup> for bandgap tuning as BeO has wurtzite structure (Figure 3), thus modulating the bandgap from 3.37 eV (ZnO) to 10.6 eV (BeO). Unfortunately, due to large difference in covalent radii (1.22 Å for Zn, 0.96 Å for Be)<sup>38</sup>, BeZnO alloys with intermediate content of Be (from 35% to 70%) are unstable and tend to segregate into high and low Be content phases<sup>39,40</sup>. Consequently, the lattice constant of BeZnO remains nearly unchanged, if Be content increases above 10%, as most of the newly added Be atoms take interstitial positions instead of substituting Zn at the cation sites<sup>39,41</sup>.

In order to overcome the aforementioned shortcomings of MgZnO and BeZnO ternaries, BeMgZnO quaternary alloy has been considered,<sup>42-44</sup> where much larger covalent radius of Mg (1.41Å)<sup>38</sup> compensates the strain caused by the incorporation of Be with small covalent radius, thus opening an avenue towards achieving wider bandgap material which is lattice matched to ZnO. One of the attractive applications of the quaternary BeMgZnO alloy is the HFETs. In order to achieve efficient ZnO based HFETs the following conditions must be satisfied: high quality of ZnO layer that will serve as a medium for 2DEG layer and optimized growth conditions for the

barrier layer that will provide proper spontaneous and piezoelectric polarization for the formation of 2DEG; low specific contact resistivity ohmic contacts for source and drain electrodes; large barrier height and low leakage current Schottky contact for Gate electrode.

#### **1.4 ZnO based heterostructures with Two Dimensional Electron gas (2DEG):**

High speed computing, real time signal processing, telecommunication, imaging, and low noise and high frequency amplification require high frequency and high power device. Due to lack of gate quality dielectrics, high performance FETs (MESFET and HFET) is more popular compared to MOSFET. The limitations of doping and the proximity of the gate with respect to the conducting channel of MESFET are alleviated considerable with the advent of HFET. The main difference between HFET and MOSFET is that the conduction channel in a HFET is formed in equilibrium. In HFET, the source and drain ohmic contacts are made directly to the two-dimensional electron gas (2DEG) while the gate electrode between these two terminals modulates the current. A schematic cross-sectional diagram of HFET is shown in Figure 4. Large low field mobilities, relatively large maximum electron velocities, and large electron concentrations provided by many compound semiconductors are ideal for high performance FETs. Wide bandgap semiconductors, for example, SiC, diamond, and GaN are possible candidate for such devices. Among these, GaN has additional advantages, for example, large dielectric breakdown field, high electron mobility<sup>45-47</sup>, good thermal conductivity, the ability to grow a AlGaN / GaN heterostructure of a high density of two-dimensional electron gas using electric polarization. ZnO also has properties similar to GaN heterostructures including a higher saturation velocity<sup>48</sup>, a larger conduction band offset<sup>49</sup> ( $\Delta E_c$ ) for MgZnO / ZnO and the possibility to use bulk ZnO as substrate<sup>6</sup>.

Formation of two dimensional electron gases at the interface occurred due to the large band discontinuities and polarization induced screening charge. Polarization induces a field, which in turns causes a redistribution of weekly bound and free charges at the interface. The mobile carriers moved to where the fixed and opposite polarization charge exists. Because ZnO is large bandgap material, it tends to be n type, consequently, the mobile carriers are normally electrons donated by unintentional donors like defect and impurity or intentional dopant.

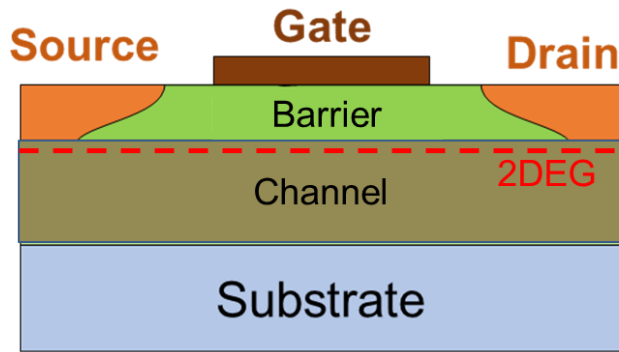


Figure 4: Cross-sectional view of heterojunction field effect transistor. Two dimensional electron gases form at the interface. The bandgap of the barrier has to be higher compared to the channel layer to confine the electron at the interface

The strain induced piezoelectric and spontaneous polarization charges have profound effects device structure. The spontaneous polarization, directed along  $[000-1]$  directions, arises when heterointerface between two oxide semiconductors with varying electronegativity is involved. The piezoelectric effect has two components. One is due to lattice mismatch strain while the other is due to thermal strain caused by the thermal expansion-coefficient difference between the substrate and the epitaxial layers. Typically, in a Ga-polarity sample the AlGaN/GaN system, the AlGaN barrier is grown on a relatively thick GaN layer to form the 2DEG. As the AlGaN has lower in-plane lattice parameter, the inherent lattice mismatch causes a biaxial tensile strain and the thermal mismatch causes a biaxial compressive strain in the growth plane. The resultant

strain induces a macroscopic electric field in the polar material. In the presence of free, weakly bound and surface charges, the thermal polarization field is screened by a redistribution of these charges.

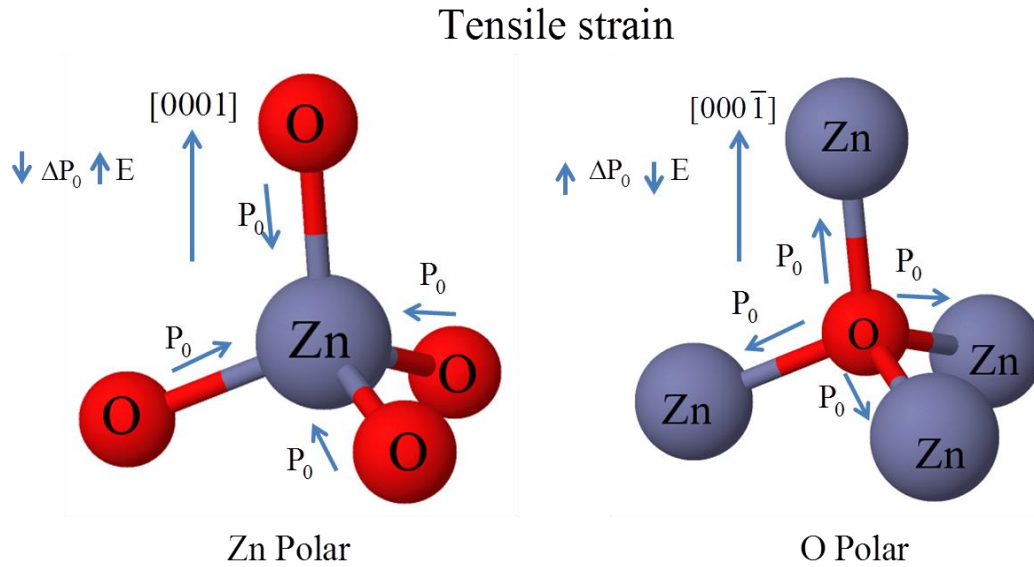


Figure 5: The ball-and stick diagram of a ZnO tetrahedron with a homogeneous in-plane tensile strain showing a net polarization in the opposite (left) and along (right) the growth direction for Zn polar and O polar material.

Depending on the surface polarity of the material, direction of the piezoelectric polarization can be opposite. As shown in Figure 5, when the bonds along c direction are from cation (Zn) to anion (O) atoms, the polarity is said to be Zn polarity, and the direction of the bonds from Zn to O along c-direction marks the [0001] direction. By a similar argument, when the bonds along the c-direction are from anion (O) to cation (Zn), the polarity is said to be O polarity, and the direction of the bonds from O to Zn along c direction marks the direction [000-1]. The direction of the piezoelectric polarization (shown in Figure 5) is opposite to the growth direction in Zn polar ZnO whereas, it is along the growth direction in O polar material. To have the accumulation of weakly bound and free electrons at the heterointerface of the channel and barrier layer, considering the structure shown in Figure 4, it is required to have Zn polarity material. To



facilitate two dimensional electron gas at the interface, the structure should be inverted where a thin channel layer, ZnO in this case, is grown on top of a thick barrier layer. Therefore, it is important to control the polarity of the structure once a particular device structure is considered.

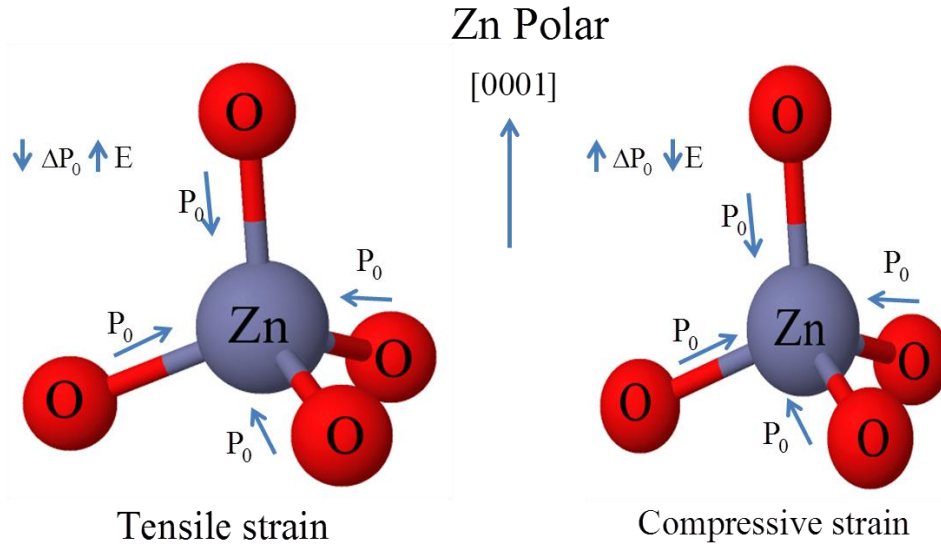


Figure 6: The ball-and-stick diagram of a ZnO tetrahedron with a homogeneous in-plane tensile (left) and compressive (right) strain showing a net polarization in the  $[000-1]$  and  $[0001]$  directions, respectively.

For a Zn-polarity film, under homogeneous in-plane tensile strain, the cumulative z-component,  $[0001]$  direction, of the polarization associated with the triple bonds decreases causing a net polarization which would be along the  $[000-1]$  direction as shown in Figure 6. When an in-plane and homogeneous compressive strain is present, the net polarization would be in the  $[0001]$  direction in the Zn-polarity case. Therefore, for the heterojunction field effect transistor (HFET) considered in Figure 4, a tensile strain in the barrier layer would direct the piezoelectric polarization charge ( $+\sigma$ ) towards the interface of heterointerface, which in returns will increase the two dimensional electron gas charge density at the interface. Moreover, as the spontaneous polarization is directed along  $[000-1]$  direction, therefore, would be summed up with the charge due to piezoelectric polarization. A compressive strain in the barrier layer would direct the

piezoelectric polarization towards the surface which would reduce the polarization charge due to the spontaneous polarization. Therefore, for the Zn-polar HFET structure, shown in Figure 4, it is important to have tensile strain in the barrier layer.

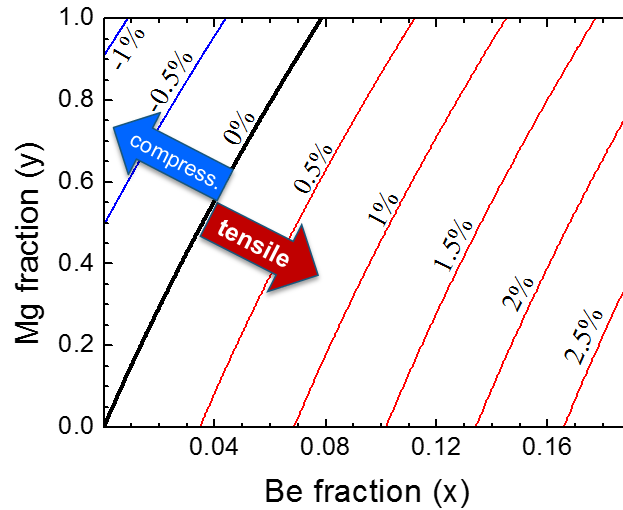


Figure 7: Strain in the  $\text{Be}_x\text{Mg}_y\text{Zn}_{1-x-y}\text{O}$  layer on ZnO template as a function of Be and Mg contents. The negative and positive signs represent the compressive and tensile strain, respectively.

As has been mentioned earlier that ZnO based IIA oxides semiconductor offers wide range of bandgap and band offset tunability. As observed from Figure 3 that both MgO and BeO has higher bandgap compared to ZnO. Interestingly, MgO has lower in-plane lattice parameter (theoretical wurtzite MgO  $a$  lattice parameter 3.32 Å [Ref. <sup>50</sup>]) compared to ZnO (3.25 Å [Ref. <sup>50</sup>]). On the other hand, BeO in-plane lattice parameter (2.698 Å [Ref. <sup>51</sup>]) is higher compared to ZnO, which opens the path of band strain engineering in  $\text{Be}_x\text{Mg}_y\text{Zn}_{1-x-y}\text{O}$  quaternary alloy system. In the BeO-MgO-ZnO system the knowledge of in-plane lattice parameters makes it possible to calculate the strain in ZnO-based heterostructures, including structures with 2DEG and quantum wells, which provides a guide for polarization charge engineering by tuning the sign and amount of piezoelectric polarization. The lattice parameter  $a$  increases and decreases

with increasing Mg and Be content, respectively. Therefore, by varying the Be and Mg content of BeMgZnO one can tune the in-plane lattice parameter  $a$  and thus control the sign and amount of strain, shown in Figure 7, in the BeMgZnO/ZnO heterostructures.

## 1.5 Metal-semiconductor Schottky diode:

It is widely believed that Schottky contact is of great importance for device performance and reliability. Improvements in reliability require a full understanding of current transport mechanism in Schottky contact, which remains an outstanding challenge in the development of electronic devices.

### 1.5.1 Schottky-Mott model:

Schottky barrier information was explained by Schottky-Mott model in terms of a space charge region on the semiconductor side of the contact which assumes no interaction between the metal and semiconductor. Since at thermal equilibrium no current is flowing, Fermi level of any two solids in contact must be same. Therefore, the Schottky barrier is created by the redistribution of electric charge between the metal and semiconductor as their respective fermi level are aligned.

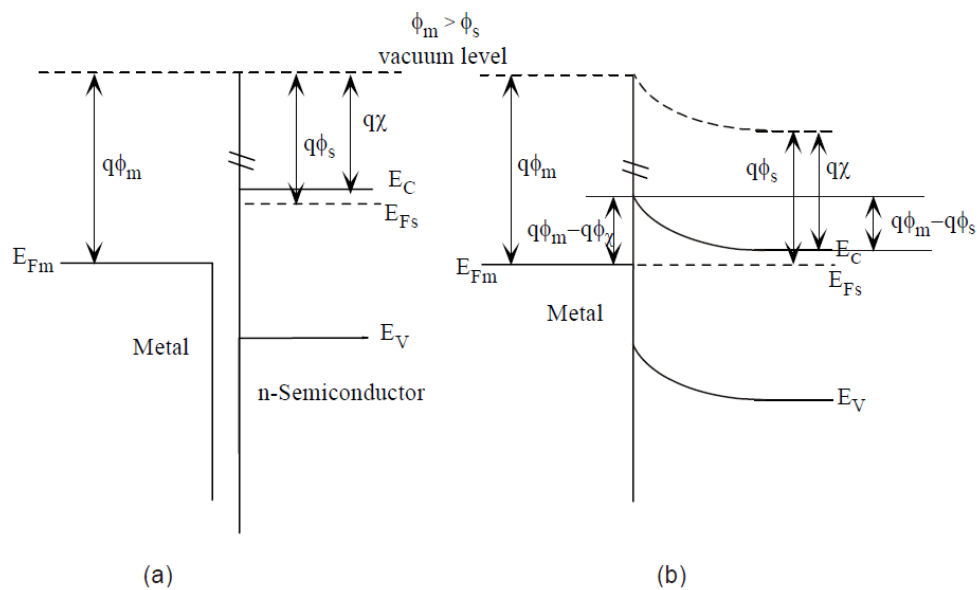


Figure 8 A metal n-type semiconductor pair before (a) and after (b) contact with no surface/interface states. The metal work function is greater than that for the semiconductor ( $\phi_m > \phi_s$ ).<sup>52</sup>

Before contact, the Fermi levels of the metal and semiconductor, referenced to the vacuum level, are  $\phi_m$  and  $\phi_s$  respectively. On contact, electrons flow from the semiconductor to the metal until the Fermi levels line up, leaving behind a depletion region of positive space charge in the semiconductor. The density of states at the metal Fermi level is so high that the transfer of charge from the semiconductor causes negligible change in its position. Hence, the depletion region lies in the semiconductor only. In the absence of interface states, the Schottky barrier height is simply the difference between the work function of the metal and the electron affinity of the semiconductor,

$$q\phi_{Bn0} = q\phi_m - q\chi (n\text{-type}) \quad 1$$

Based on equation 1, in order to achieve rectifying behavior with MSC, a metal with  $\phi_m > \phi_s$  must be chosen and higher  $\phi_m$  will result in higher Schottky barrier height  $q\phi_B$ . However, in practice simple equation 1 is rarely realized due to presence of surface contamination and defects that introduce surface state and can potentially even pin the position of Fermi level to the level of the defect. The interface states usually discussed on the basis of two assumptions: (1) interfacial layer of atomic thickness which will be transparent to electrons but can withstand potential across it, and (2) the interface states are the property of semiconductor and are independent of the metal. Considering the extreme case, when a donor-like interface trap density is very high (infinity), the barrier height becomes independent of the metal work function.

The most widely used method to determine the barrier height of a Schottky contact is to measure its current-voltage (I-V) characteristics based on the thermionic emission current conduction mechanism developed by Hans Bethe<sup>53</sup>. In this theory it is assumed that the electrons approaching the barrier are in thermal equilibrium and the emission probability is low enough

that the resulting current flow does not disturb this thermal equilibrium. In practice these conditions are met when  $\Phi_B \gg kT/q$ . The thermionic emission (TE) of electrons in either direction over a potential barrier of height  $\Phi_B$  is

$$I_0 = AA^*T^2 \exp\left(\frac{-q\Phi_B}{kT}\right) \quad 2$$

where  $A^*$  is the Richardson constant,  $k$  the Boltzmann constant, and  $T$  the semiconductor temperature. When the Schottky contact is forward biased by an external voltage  $V$ , the barrier potential is lowered to  $\Phi_B - qV$ . The electron flow from the semiconductor to metal increases and the forward current density is now

$$I_{fwd} = AA^*T^2 \exp\left(-\frac{q(\Phi_B - V)}{kT}\right) \quad 3$$

The current density flowing in the reverse direction (electron flow from the metal to the semiconductor) is independent of the applied bias voltage and is known as the saturation current  $I_0$  where,

$$I_0 = AA^*T^2 \exp\left(\frac{-q\Phi_B}{kT}\right) \quad 4$$

The net current flowing across the Schottky contact is therefore

$$I = I_{fwd} - I_0 = I_0 \left[ \exp\left(\frac{qV}{kT}\right) - 1 \right] \quad 5$$

For the applied bias voltage  $V \gg kT/q$  the -1 term in equation 5 is negligible and the current density should increase exponentially with  $V$ . When the Schottky contact is reversed biased, the barrier potential increases to the Schottky contact is reversed biased, the barrier potential increases to  $\Phi_B + qV$  which makes  $I_{fwd} \ll I_0$  and the net current density is equal to the saturation current density  $I_0$  which is independent of  $V$ .

Equation 5 represents the ideal case of pure thermionic emission over a homogeneous, defect free, Schottky barrier with no interface states. For the analysis of real  $I$ - $V$  characteristics an ideality factor is introduced into Equation 5 giving,

$$I = I_0 \left[ \exp\left(\frac{qV}{nkT}\right) - 1 \right] \quad 6$$

Values of  $n$  greater than unity are caused by non-ideal behavior which cause the Schottky contact to deviate from pure thermionic transport. The most common types of non-ideal behavior are image force lowering, field emission, lateral contact inhomogeneity and recombination which are describe below

### 1.5.2 Image force lowering:

even for perfectly homogeneous contacts with no interface states, the effective barrier height of all Schottky junctions is slightly reduced due to image force (IF) lowering. As an electron approaches the barrier, it experiences a small attractive force with the positive “image” charge that is induced in the metal<sup>54</sup>. This effect lowers the height of the barrier by an amount  $\Delta\Phi_{if}$  given by,

$$\Delta\Phi_{if} = \left[ \left( \frac{q^3 N_D}{8\pi^2 \epsilon_\infty^2 \epsilon_s \epsilon_0^3} \right) \left( \Phi_B - V - \xi - \frac{kT}{q} \right) \right]^{\frac{1}{4}} \quad 7$$

Since  $\Delta\Phi_{if}$  is a function of  $V$  and it increase with increasing reverse bias. For a given semiconductor,  $\Delta\Phi_{if}$  also depends on the effective doping concentration  $N_D$ . Since barrier lowering is only experienced by electrons approaching the interface, it only affects  $I$ - $V$  and not  $C$ - $V$  measurement. The increased ideality factor ( $n_{if}$ ) of a Schottky diode due to image force lowering is given by

$$\frac{1}{n_{if}} = 1 - \frac{\Delta\Phi_{if}}{4} \left( \Phi_B - V - \xi - \frac{kT}{q} \right)^{-1} \quad 8$$

### 1.5.3 Thermionic field emission:

A more likely process for moderately doped semiconductors is thermionic field emission (TFE), in which carriers are thermally excited to a position on the barrier which is sufficiently thin for

tunneling to occur. The width of the depletion region of a Schottky diode depends on the doping level of the semiconductor. It is inversely proportional to the square root of doping concentration ( $N_D$ ) which follows the equation

$$W_d = \sqrt{\frac{2\epsilon_s \epsilon_0 V_{bi}}{qN_D}} \quad 9$$

Therefore, in heavily doped semiconductor the barrier may be thin enough for electrons to tunnel directly through it. The tunneling parameter  $E_{00}$  can be expressed as

$$E_{00} = \frac{qh}{4\pi} \left( \frac{N_D}{m^* \epsilon_s \epsilon_0} \right)^{\frac{1}{2}} \quad 10$$

where  $m^*$  is the effective electron mass. When  $E_{00} \ll kT$  the dominant current transport process is thermionic emission, whereas when  $E_{00} \gg kT$  field emission (tunneling) becomes important. For  $E_{00} \sim kT$ , current transport will be significantly affected by thermionic field emission which causes a lowering of the effective barrier height given by

$$\Delta\Phi_{TFE} = \left( \frac{3E_{00}}{2} \right)^{\frac{2}{3}} \left( \Phi_B - \xi - \frac{kT}{q} \right)^{\frac{1}{3}} \quad 11$$

And an increased ideality factor of

$$\eta_{TFE} = \frac{qE_{00}}{kT} \coth \left( \frac{qE_{00}}{kT} \right) \quad 12$$

For semiconductor with doping concentration  $N_D < 10^{18} \text{ cm}^{-3}$ , the probability of TFE is very small. However, at very temperature, this situation can change with the presence of defect states or traps in the depletion region of the semiconductor which increase the tunneling probability as electron can first tunnel into these defect states and then through the barrier.

#### 1.5.4 Recombination:

Recombination current can occur in the depletion region which can increase the reverse saturation current due to the minority carrier. The recombination current is given by

$$J_{rc} = \frac{qN_i W_d}{2\tau} \left[ \exp\left(\frac{qV}{\eta_{rc} kT}\right) \right] \quad 13$$

where  $\eta_{rc}$  is the ideality factor for this process (which is typically 2),  $N_i$  is the minority carrier concentration, and  $\tau$  is the minority carrier life time within the depletion region.

### 1.5.5 Schottky barrier inhomogeneity:

Real Schottky contacts are likely to contain inhomogeneities that cause a spatial variation in barrier height. This fluctuation can be caused by structural defects, surface contamination, intrinsic point defects and extrinsic surface defects.

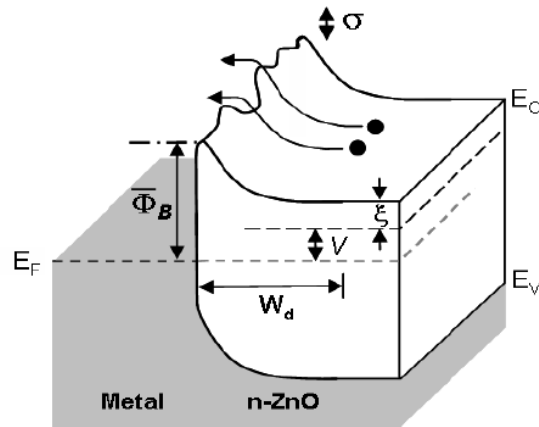


Figure 9: Band diagram in two dimensions of an inhomogeneous Schottky contact under an applied forward bias  $V$ .

Werner and Guttler<sup>55</sup> assumed a Gaussian distribution  $P(\Phi_B)$  of barrier height with a mean value of  $\bar{\Phi}_B$  and standard deviation  $\sigma$  to account the schottky barrier fluctuations caused by spatial inhomogeneities of a length scale less than the depletion region width  $W_d$ . An schematic diagram of the potential fluctuation is shown in two dimensions in Figure 9. They have found the mean barrier height and ideality factor as a function of temperature. In chapter 5, we have discussed the temperature dependence of barrier height and ideality factor for silver Schottky diode on BeMgZnO/ZnO heterostructure.



## 1.6 Organization of this thesis

This thesis focuses on growth of Zn polar BeMgZnO/ZnO heterostructure by plasma enhanced molecular beam epitaxy and device fabrication of Ag Schottky diode on BeMgZnO/ZnO heterostructure. Chapter one deals with the basic structural and optical properties of ZnO and its potential application. A brief literature review of polarity control mechanism in MBE growth technique has been presented. The advantage and disadvantage of ZnO based ternaries and quaternaries on their application as a barrier in ZnO based heterojunction field effect transistor has been discussed. A brief theory of polarization induced two dimensional electron gas and metal semiconductor Schottky diode are also presented in this chapter.

Chapter two deals with the polarity and strain control mechanism of ZnO on (0001) GaN/sapphire template by means of oxygen to Zn ratio during the nucleation growth of ZnO. X-Ray Diffractometry (XRD) along the (0002) direction was used to calculate the residual strain in ZnO films. Growth rate of the film was deduced from the interference fringes observed in  $2\theta-\omega$  XRD scan. High Angle Annular Dark Field (HAADF) analysis was carried out in a double Cs corrected JEOL ARM 200 Scanning Transmission Electron Microscope (STEM) to investigate the ZnO/GaN interface. The surface morphology was characterized using Atomic Force Microscopy (AFM).

Chapter three discusses growth of O polar BeMgZnO/ZnO heterostructure. Cross sectional TEM images showed structural improvement of BeMgZnO layer compared to BeZnO with the inclusion of Mg into the ternary lattice. The improvement in crystallinity was further supported by high resolution X-ray diffraction. Growth kinetics of BeMgZnO layer has been studied within the temperature range from 450 °C to 500 °C. Crystallinity of the quaternary samples grown within this temperature range was realized by HRXRD scan along 0002 direction. Reflection

High Energy Electron Diffraction (RHEED) was used to monitor the in-situ growth progression of quaternary samples. Photoluminescence spectra at 15 K temperature and the subsequent analysis were performed to understand the thermodynamic limitation of Mg incorporation into wurtzite BeMgZnO lattice at the elevated temperature.

Chapter 4 discusses Zn polar BeMgZnO/ZnO heterostructure with two dimensional electron gas. Sheet carrier density obtained from BeMgZnO/ZnO heterostructures with different Be and Mg composition has been compared with the theoretical calculation and reported values from MgZnO/ZnO heterostructure as well.

Chapter 5 deals with the fabrication of Ag Schottky diode on BeMgZnO/ZnO heterostructure. Current-Voltage (I-V) measurement was carried out in the temperature range of 85-457K. Based on the thermionic emission theory, the ideality factor and barrier heights were calculated. Experimentally obtained Richardson constant of  $\text{Be}_{0.02}\text{Mg}_{0.26}\text{ZnO}$  were compared with the theoretical calculation. Carrier confinement of two dimensional electron gas was investigated through Capacitance-Voltage (CV) measurement. Hot electron energy relaxation time for BeMgZnO/ZnO heterostructures, obtained from noise temperature measurement at high electric field, are compared with that of GaN based heterostructure and already reported doped bulk ZnO. All results are summarized and future work is discussed in chapter 6.

## Chapter 2. Polarity control of ZnO on (0001) GaN/sapphire template

### 2.1 Introduction:

The most frequently used substrate for epitaxial growth of ZnO thin films and heterostructures is c-plane sapphire, which has a large in-plane lattice mismatch of 18% with ZnO, and therefore, limits the material quality. Moreover, growth of high quality Zn-polar ZnO on sapphire is not well established<sup>56</sup>. GaN templates on sapphire, owing to their high structural quality, thanks to the remarkable progress achieved in the GaN-based light emitter technology, are attractive alternatives for growing Zn-polar ZnO while offering only a moderate lattice mismatch of 1.8%. On (0001) GaN/sapphire templates, the growth of Zn-polar ZnO has been reported by Hong *et al.* by using Zn pre-exposure whereas O-polar ZnO is grown under the condition of oxygen pre-exposure, the latter of which leads to Ga<sub>2</sub>O<sub>3</sub> formation on GaN<sup>19,20</sup>. Specifically, a film of single crystalline Ga<sub>2</sub>O<sub>3</sub> of ~4 nm thickness was shown to form and act as a blocking layer of metal polarity propagation from Ga polar GaN to ZnO. Additionally, no O-polar ZnO grown on GaN has been reported where the GaN was kept under continuous Zn beam exposure prior to the nucleation growth. We have reported the growth of O-polar ZnO on the (0001) GaN although it was kept under continuous Zn flux wherein the oxygen-to-zinc ratio during growth of the low-temperature ZnO nucleation layer played the pivotal role for polarity inversion. We have showed, as a corollary to previous work, that only one monolayer of non-stoichiometric GaO<sub>x</sub> at

interface is all it takes to invert the polarity. Additionally, we have demonstrated an unprecedented finding that residual strain of the resulting ZnO layers, which is related with polarity inversion, can be controlled by oxygen to zinc ratio during nucleation growth. Our results are contrary to a visceral reaction that Zn-polarity ZnO should result on Ga-polarity GaN without O pre-exposure. The sign change of strain is also extraordinary.

## 2.2 Growth technique:

ZnO films were grown by plasma enhanced molecular beam epitaxy (P-MBE). Highly resistive (60 k $\Omega$ .mm), carbon-compensated 2.5- $\mu$ m Ga-polar (0001) GaN layers prepared by metal-organic chemical vapor deposition on c-plane sapphire served as substrates. Prior to loading into the MBE system, the GaN templates were cleaned with aqua regia to remove possible metal contamination followed by immersion in a HCl : H<sub>2</sub>O = 1 : 1 solution to remove any gallium oxide (Ga<sub>2</sub>O<sub>3</sub>) from the surface. After loading the substrate to the growth chamber, GaN surface was thermally cleaned at 625 °C for 15 min followed by an exposure to Zn beam to terminate the GaN surface with Zn adatoms<sup>57</sup>. The same Zn flux of 0.1 Å/s was maintained during cool down and the growth of low-temperature (LT) ZnO nucleation layer of thickness 25 nm at T<sub>g</sub> = 300°C. During the LT ZnO growth, the oxygen-to-Zn ratio (VI/II ratio in the following discussion) was varied via varying the O flux within a wide range, from deep Zn rich (VI/II = 0.55) to deep oxygen rich (VI/II = 3) conditions. After annealing the LT-ZnO layer at 730 °C for 5 min at 1 $\times$ 10<sup>-5</sup> Torr reactor pressure with closed O-plasma shutter, ZnO growth proceeded at 670 °C. For all the samples under investigation, Zn flux and oxygen gas flow during the high temperature (HT) ZnO growth were kept at 0.25 Å/s and 0.7 sccm, respectively. 400 W RF power of the plasma cell was used for both the LT- and the HT-ZnO growth. The growth time for HT ZnO was 2 hours and total film thickness for the samples nucleated with VI/II ratio below 1.5 is

around 365 nm and for those nucleated with larger VI/II ratio is 175 nm. The  $c$  lattice parameters were deduced from X-Ray Diffractometry (XRD) along the (0002) direction which was used to calculate the residual strain in ZnO films. Growth rate of the film was deduced from the interference fringes observed in  $2\theta-\omega$  XRD scan. High Angle Annular Dark Field (HAADF) analysis was carried out in a double Cs corrected JEOL ARM 200 Scanning Transmission Electron Microscope (STEM) to investigate the ZnO/GaN interface. The surface morphology was characterized using Atomic Force Microscopy (AFM).

### 2.3 Polarity control of ZnO on GaN:

The growth rates of the HT-ZnO layers deduced from the XRD interference fringes are shown in Figure 10 as a function of the VI/II ratio during LT-ZnO growth. As seen from the figure, the growth rate of ZnO films exhibiting tensile biaxial strain (170 nm/h) is a factor of 2.25 greater than that of the films with compressive strain (75 nm/h). More importantly, the ZnO growth rate correlates with the sign of strain rather than its extent. The ratio of growth rates of the films grown on LT ZnO buffers deposited with different VI/II ratio is consistent with the growth ratio of Zn- and O-polar ZnO reported elsewhere<sup>30,58</sup>. Therefore, the reduced growth rate of ZnO films nucleated under highly oxygen-rich conditions can be caused by the inversion of surface polarity from Zn- to O-face at VI/II~1.5. Furthermore, we have performed wet etching in a very dilute solution of 0.65% HCl in water to distinguish the etching behavior. This study revealed at least 7 times higher etching rate of the films exhibiting relatively lower growth rate (O-polar) compared to the films featured by the high growth rate (Zn-polar). The observed etching rate is also consistent with etching rates of Zn- and O-polar ZnO reported in literature<sup>58,59</sup>. Therefore, one can conclude that highly oxygen-rich conditions during the nucleation of ZnO on GaN

templates in P-MBE give rise to the surface polarity inversion from Zn- to O-polar, as indicated in Figure 10.

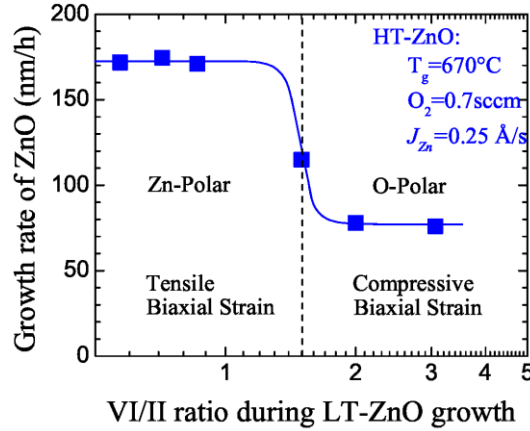


Figure 10 Growth rate of ZnO films as a function of VI/II ratio during LT-ZnO growth. The solid curve is a guide to the eye.

As to be expected, ZnO films nucleated at high and low VI/II ratios exhibit drastically different surface morphology as observed by AFM scans shown in Figure 11. Away from the transition point (VI/II = 1.5), surfaces are uniformly smooth, which explicitly implies that layers are of single polarity. However, at the transition point surface roughness increases significantly [root mean square (RMS) roughness of 5.2 nm for  $5 \mu\text{m} \times 5 \mu\text{m}$  scan, not shown], suggesting mixed polarity domains. The O-polar films (nucleated at VI/II ratio > 1.5), Figure 11 (a) and (c), exhibit hillock-like morphology with pronounced atomic terraces, while the Zn-polar layers (Figure 11 (b) and (d)) are characterized by a flat surface with large density of hexagonal pits. RMS surface roughness values for  $1 \mu\text{m} \times 1 \mu\text{m}$  scans of O-polar and Zn-polar ZnO are 0.25 nm and 2 nm, while those for the  $5 \mu\text{m} \times 5 \mu\text{m}$  scan area are 0.9 nm and 1.5 nm, respectively. As the morphology of O-polar ZnO is characterized by hexagonal hillocks, some degree of long-scale height modulation is expected, resulting in the increase of RMS value with increasing scan area,

whereas Zn polar ZnO does not exhibit this characteristic. The observed surface morphologies of Zn- and O-polar films are similar to those reported by Wang *et al* <sup>58</sup>.

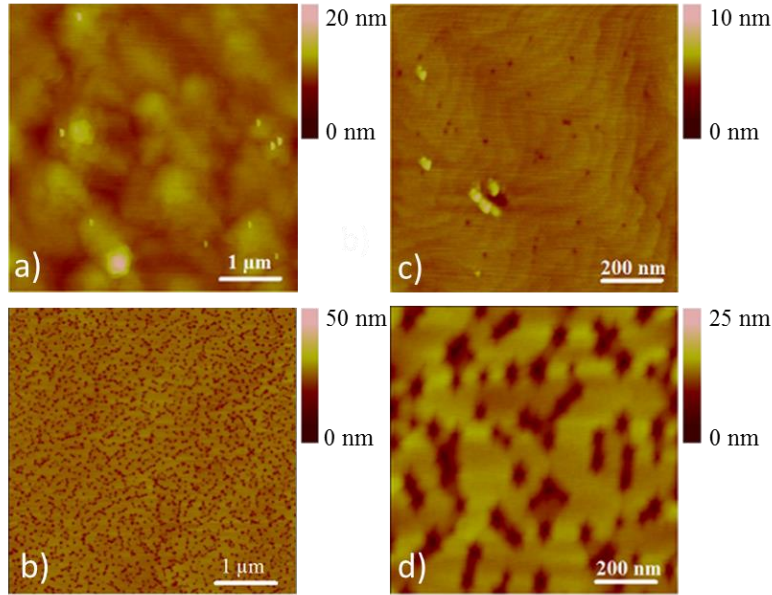


Figure 11 :  $5 \mu\text{m} \times 5 \mu\text{m}$  AFM images of (a) O polar and (b) Zn polar ZnO. (c) and (d) show the respective images for  $1 \mu\text{m} \times 1 \mu\text{m}$  area.

To verify polarity inversion we have carried out cross sectional weak beam TEM analysis (Figure 12 (a)) of a structure nucleated at  $\text{VI/II} = 6.0$ , much larger than the critical value of 1.5 above which O-polar ZnO is obtained. As seen from the image ( $g=0002$ ), no vertical inversion domains are present inside the ZnO layer (the interface position is shown by the horizontal arrows). This indicates that the polarity inversion takes place throughout the GaN surface, immediately at the GaN/ZnO interface, in agreement with AFM data revealing flat surface morphologies. A typical high angle annular dark field image of the ZnO/GaN interface is shown in Figure 12 (b), where the position of the interface is marked by the arrows. As can be seen from the change of stacking sequences, the polarity inversion takes place within one monolayer. The change in stacking sequences at inversion boundaries has been reported in earlier investigations of prismatic inversion domain boundaries in GaN/sapphire structures by high resolution TEM

<sup>60,61</sup>. In the case presented here, the change is permanent and does not depend on the focus setting. This indicates that steady state coverage of the GaN surface with Zn atoms by continuous Zn pre-exposure fails to prevent the formation of presumably one monolayer of nonstoichiometric GaO<sub>x</sub> which is sufficient to invert the polarity. Therefore, the mechanism governing this transition is different from the one proposed by Hong et al <sup>19,20</sup>, which relied on the formation of a 3-4 nm thick Ga<sub>2</sub>O<sub>3</sub> layer introducing a centrosymmetric operation and thus helping to break the metal polarity transfer from GaN to ZnO. For such a polarity reversal within one monolayer, it is difficult to think of only geometric and topological factors; it is very likely that also chemical and electronic factors are playing an important role. Therefore, in order to unveil the underlying mechanism, an extensive study of the chemical and electronic structure of GaN/ZnO interface by combining theoretical modelling <sup>62</sup> and high resolution transmission electron microscopy <sup>63,64</sup> is underway.

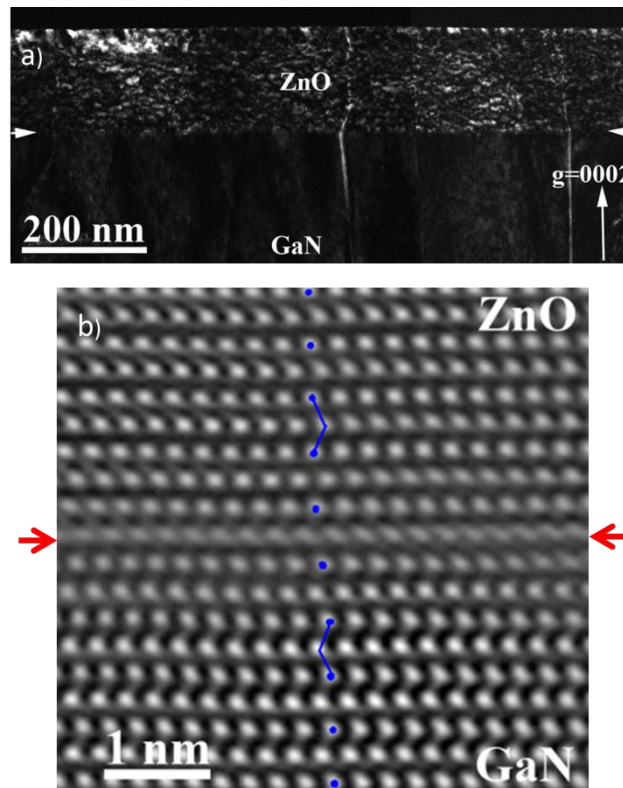




Figure 12: (a) Weak beam TEM micrograph,  $g=0002$ , and (b) HAADF image of ZnO/GaN heterointerface of the sample nucleated with VI/II = 6.0. The dots represent the Ga and Zn atoms in GaN and ZnO lattice respectively. The line represents the change in stacking sequence in GaN and ZnO lattice. Bright vertical lines in the weak beam image (a) are threading dislocations propagating from GaN.

#### 2.4 Strain control of ZnO on GaN:

Figure 23 (a) shows the triple axis  $2\theta-\omega$  scans of 0002 reflection from ZnO films on (0001) GaN/sapphire templates. As seen from the figure, the ZnO peak systematically shifts towards smaller Bragg angles with increasing VI/II ratio from 0.55 to 3 during the growth of LT nucleation layer. This shift indicates that the  $c$  lattice parameter increases from 5.198 Å to 5.217 Å. When compared with the bulk ZnO lattice constant, these values suggest that the structures grown employing VI/II ratios below 1.5 during the deposition of the LT nucleation layer are under tensile biaxial strain, irrespective of the film thickness, while the use of larger VI/II ratio during the nucleation layer results in compressive strain in the high-temperature ZnO layers. To compare the strain state of samples with similar thickness, a 175 nm thick film was also grown at a VI/II ratio of 0.85 during nucleation. Tensile biaxial strain was found to be present in this sample; however, its magnitude was higher in the thicker (365 nm) sample. Well pronounced thickness interference fringes observed for all the samples studied are indicative of relatively smooth surface and ZnO/GaN interface.

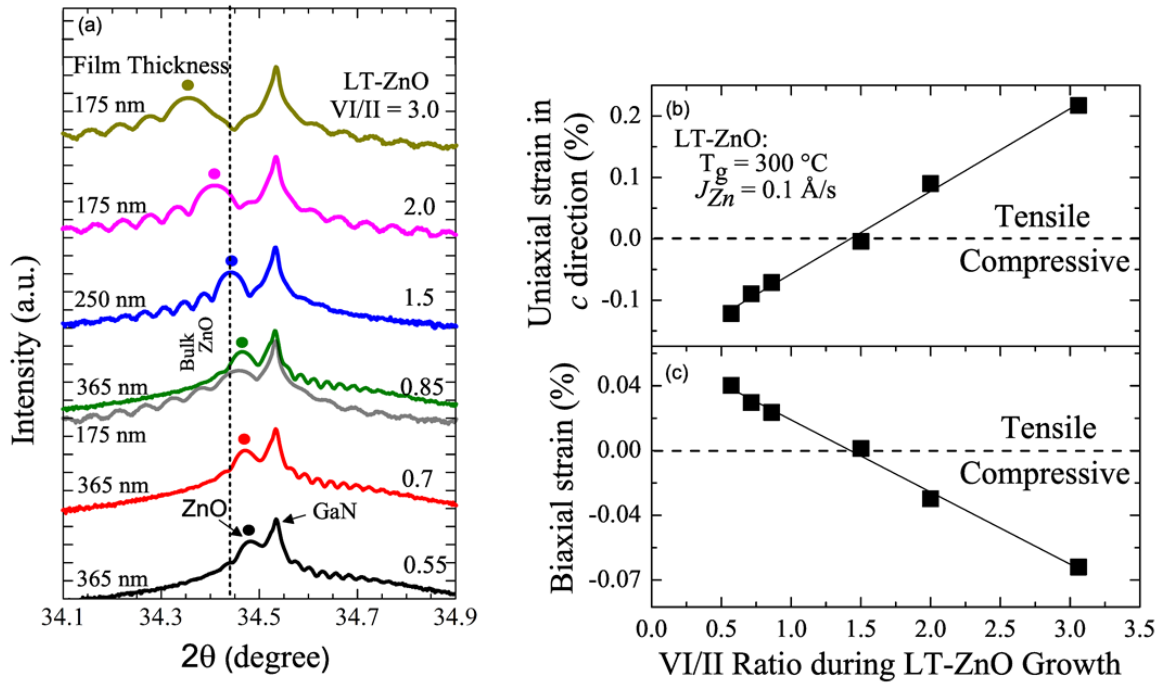


Figure 13: (a) Semi-logarithmic plot of XRD triple axis  $2\theta$ - $\omega$  diffraction patterns along the [0002] direction. From bottom to top, VI/II ratio in the LT-ZnO layer increases from 0.55 to 3.0 at a constant Zn flux of  $J_{Zn} = 0.1 \text{ \AA/s}$ . Dash line represents the Bragg angle for bulk ZnO in [0002] direction. Solid circles indicate the ZnO peak positions. Residual strain (b) measured along the c direction and (b) calculated in the biaxial plane of ZnO as a function of VI/II ratio during LT-ZnO growth. The negative and the positive sign in y-axis denote the compressive and tensile residual strain, respectively. Straight lines are used to guide the eye.

Residual strain along the c direction of ZnO lattice is calculated from the corresponding peak of X-ray  $2\theta$ - $\omega$  diffraction pattern shown in Figure 13 (a). Figure 13 (b) shows the effect of oxygen to Zn ratio during the LT-ZnO growth on the uniaxial (in the growth direction) residual strain,  $\epsilon_{\perp} = (c_f - c_b)/c_b$  of ZnO, where  $c_f$  and  $c_b$  are the thin-film (derived from XRD scans) and the bulk lattice parameter, respectively. Here, an experimentally determined bulk ZnO out-of-plane lattice parameter of  $5.204 \text{ \AA}$  have been used<sup>65</sup>. Because of the substantial broadening of the asymmetric ZnO reflection and its overlap with the very intense neighboring GaN reflection, it is difficult to discern the biaxial strain in ZnO directly with needed precision. Therefore, we have calculated the corresponding biaxial residual strain by using the Poisson ratio ( $\nu$ ) of 0.298 for thin film ZnO

<sup>66</sup>. Figure 13 (c) shows the biaxial strain ( $\epsilon_{\parallel}$ ) calculated from the corresponding uniaxial strain ( $\epsilon_{\perp}$ ) shown in Figure 13 (b) by using  $\vartheta = -\epsilon_{\parallel} / \epsilon_{\perp}$ . Conventionally, the positive and negative signs of the ordinate in Figure 13 (b) and (c) represent tensile and compressive strain, respectively. As evidenced from Figure 13 (c), the films are under tensile biaxial strain when the LT buffer is grown under Zn-rich conditions. As the VI/II ratio increases, the extent of biaxial strain reduces linearly, and the ZnO layer becomes relaxed at VI/II = 1.5. When the VI/II ratio during growth of the LT nucleation layer is larger than 1.5, the strain changes its sign, and the material becomes compressively strained in the biaxial plane. The amount of compressive strain rises linearly with increasing VI/II ratio. Thus, the residual strain in ZnO films grown at 670 °C is clearly controlled by the VI/II ratio during the growth of LT-ZnO nucleation layer.

To explain the variation in the residual strain in ZnO films with varying VI/II ratio during the growth of LT-ZnO buffer, we consider possible formation of point defects and thermal expansion mismatch of ZnO, GaN, and sapphire. As the thermal expansion mismatch between ZnO and sapphire substrate is dominant, it is reasonable to expect compressive biaxial strain in ZnO thin films due to higher thermal expansion coefficient of sapphire, <sup>67</sup>  $\alpha_{\parallel} = 8.1 \times 10^{-6} / ^{\circ}\text{C}$  and  $\alpha_{\perp} = 7.3 \times 10^{-6} / ^{\circ}\text{C}$ , compared to ZnO, <sup>68</sup>  $\alpha_{\parallel} = 3.0 \times 10^{-6} / ^{\circ}\text{C}$  and  $\alpha_{\perp} = 6.5 \times 10^{-6} / ^{\circ}\text{C}$  along c and a directions, respectively. In the regime of low VI/II ratio, Zn interstitials ( $\text{Zn}_i$ ) can be presumed as the primary cause of tensile biaxial strain in the Zn-polar material. It has been reported that Zn polarity of ZnO favors the formation of  $\text{Zn}_i$  compared to the O polar variety as Zn displacement is easier in Zn polar ZnO compared to O polar <sup>69</sup>. Furthermore, it is more likely to form  $\text{Zn}_i$  under Zn-rich growth conditions, because of the lowest formation enthalpy of zinc interstitials among intrinsic point defects <sup>70</sup>. Therefore, we suggest that once the Zn-polar nucleation layer is grown at a VI/II ratio < 1.5, which results in tensile biaxial strain, subsequent high temperature

growth leads to a gradual increase of tensile strain as the effect of thermal mismatch with the substrate is reduced as the film grows thicker. However, with increasing VI/II ratio, the density of Zn interstitials would reduce, thus reducing the tensile strain. Eventually, strain associated with thermal expansion mismatch between ZnO and GaN/sapphire will become dominant, and the material would become unstrained and then compressively strained, given that the material quality is sufficiently high. We also suggest that detailed microstructural analysis to substantiate the abovementioned arguments is needed.

## Chapter 3. Quaternary BeMgZnO by P-MBE

### 3.1 Introduction:

At a given substrate temperature, co-alloying of ZnO with BeO and MgO mutually enhance the incorporation of both Be and Mg into the wurtzite quaternary alloy<sup>41</sup>. As indicated by an arrow in Figure 14 (b), by increasing Mg content while keeping Be cell temperature the same, the in-plane lattice parameter first increases due to Mg incorporation into the lattice and approaches that of ZnO (lattice matching), but then decreases, which suggests that enhanced Be incorporation on cation sites with increasing Mg content. As a results, 5.1-eV BeMgZnO quaternary alloy has been achieved with a better structural quality compared to MgZnO or BeZnO ternaries.<sup>41</sup>.

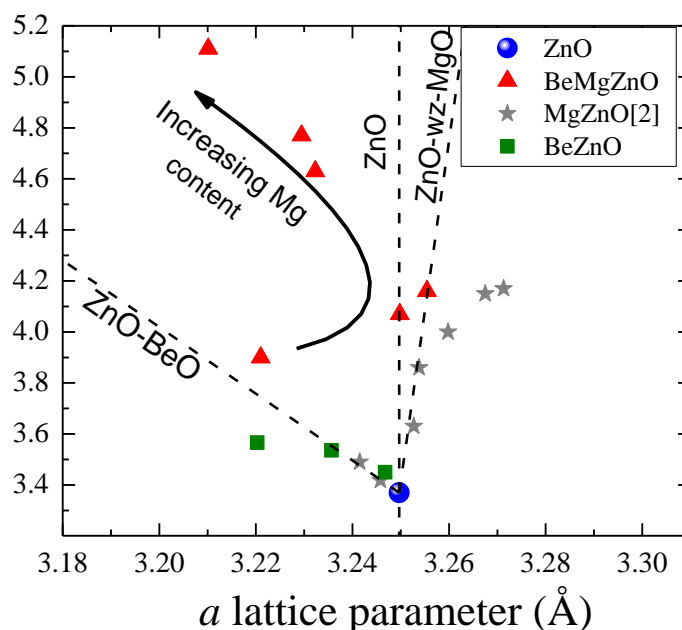


Figure 14: Bandgap vs  $a$  lattice parameter for BeMgZnO, BeZnO and MgZnO. Dashed lines are linear interpolation between wurtzite binaries.

Up until now, the growth of single crystal quaternary BeMgZnO has been limited to growths on c-plane sapphire,<sup>42,44,71,72</sup> quartz,<sup>73,74</sup> silicon<sup>73</sup> and GaN,<sup>75,76</sup> and the explored growth techniques are MBE,<sup>39,43,71,72</sup> PLD,<sup>42,44,73</sup> sputtering<sup>74,76</sup>,<sup>24,25</sup> and sol-gel synthesis.<sup>77</sup> It is important to note that in earlier reports, the growth of  $\text{Be}_x\text{Mg}_y\text{Zn}_{1-x-y}\text{O}$  was established at or below 400 °C<sup>41,71</sup>. We have achieved growth of O-polar  $\text{Be}_x\text{Mg}_y\text{Zn}_{1-x-y}\text{O}$  at temperature as high as 500 °C on (0001) GaN/sapphire templates by Plasma assisted Molecular Beam Epitaxy (P-MBE) while in parallel exploring the effect of Zn to (Be + Mg) flux ratio ( $J_r$ ) in suppression of the second phase segregation in the temperature range from 450 °C to 500 °C. Prior to the growth of quaternary  $\text{Be}_x\text{Mg}_y\text{Zn}_{1-x-y}\text{O}$ , the polarity of ZnO buffers has been inverted from Zn-polar to O-polar by employing high VI/II ratio during nucleation<sup>14</sup>. Photoluminescence (PL) at 15 K and in-situ monitoring by Reflection High Energy Electron Diffraction (RHEED) suggest formation of a wurtzite MgO-rich second phase when the Zn to (Be + Mg) flux ratio is relatively low at the

higher end of growth temperature range explored. To account for this phenomenon, we suggest a limiting phenomenon for incorporation of Mg into ZnO-rich  $\text{Be}_x\text{Mg}_y\text{Zn}_{1-x-y}\text{O}$  lattice facilitated by the natural inclination towards the growth of MgO-rich phase due to its more negative enthalpy of formation

### 3.2 O-polar BeZnO and BeMgZnO on c-sapphire

Figure 15 presents cross-sectional dark field TEM images of the  $\text{Be}_{0.10}\text{Zn}_{0.90}\text{O}$  and  $\text{Be}_{0.07}\text{Mg}_{0.30}\text{Zn}_{0.63}\text{O}$  layers. The 175-nm-thick ternary and quaternary alloys were grown at  $T_S = 400^\circ\text{C}$ , and the same oxygen to metal flux ratio was maintained during the growth. As seen for the TEM images, the  $\text{Be}_{0.10}\text{Zn}_{0.90}\text{O}$  layer exhibits non-uniform contrast, which is caused by the presence of high density of stacking faults and possible second-phase inclusions (Figure 15 (b)). The presence of high angle grain boundaries is also revealed from TEM analysis in  $\text{Be}_{0.10}\text{Zn}_{0.90}\text{O}$ , which is indicative of substantial mosaicity of the ternary material (Figure 15 (c)). In aggregate, this leads to a rough surface morphology of the  $\text{Be}_{0.10}\text{Zn}_{0.90}\text{O}$  layer and low intensity of its 0002 reflection on  $2\theta-\omega$  HRXRD scan, comparable to that from 15-nm thick low-temperature ZnO buffer [Figure 16 (b)]. As evinced from Figure 16 (a), threading dislocations originating mostly at the ZnO/sapphire interface are dominating defects in quaternary  $\text{Be}_{0.07}\text{Mg}_{0.30}\text{Zn}_{0.63}\text{O}$  alloy. Inhomogeneous contrast is likely an indicative of compositional fluctuations. Improved structural quality of the quaternary material, despite a large density of threading dislocations, is also confirmed by HRXRD, as evidenced from an order of magnitude higher intensity of its 0002 reflection compared to that from the ternary layer [Figure 16 (b)]. This finding is in agreement with the TEM micrograph in Figure 15, which clearly indicates the presence of high-angle boundaries, and therefore, misoriented blocks in BeZnO.

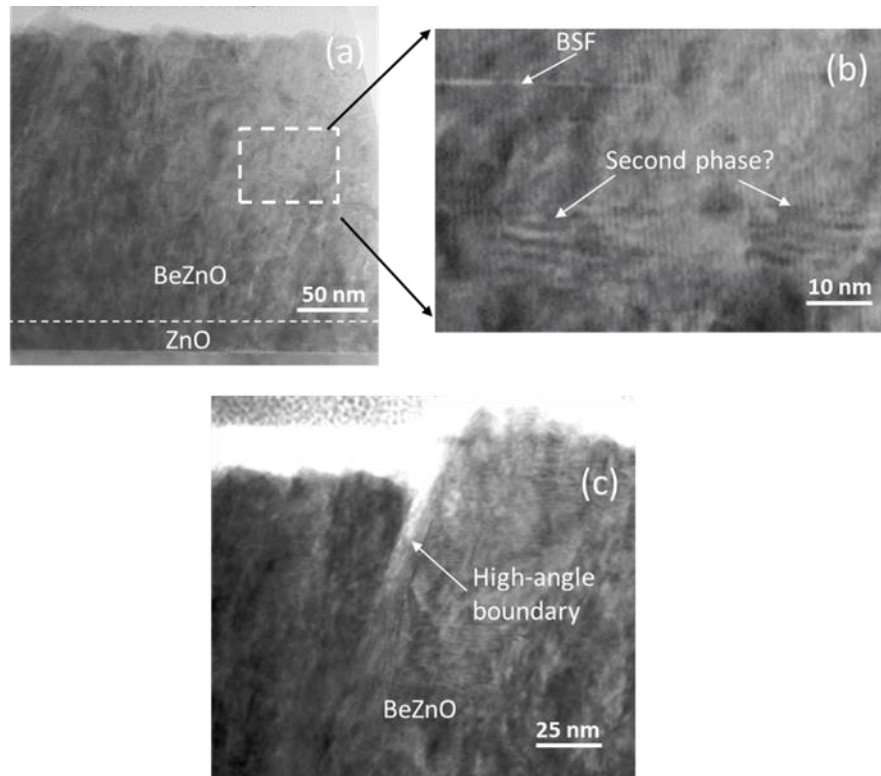


Figure 15:(a) Cross-sectional TEM image of  $\text{Be}_{0.10}\text{Zn}_{0.90}\text{O}/\text{ZnO}$  structure. (b) Stacking faults and possible second-phase inclusions and (c) high-angle grain boundaries.

The  $c$  lattice parameter of the  $\text{Be}_{0.07}\text{Mg}_{0.30}\text{Zn}_{0.63}\text{O}$  quaternary alloy ( $5.081 \text{ \AA}$ ) deduced from the HRXRD peak is smaller than that of the  $\text{Be}_{0.10}\text{Zn}_{0.90}\text{O}$  ternary material ( $5.123 \text{ \AA}$ ) suggesting that a substantial fraction of Be atoms are likely incorporated into a BeO-rich second phase or as interstitial atoms in  $\text{Be}_{0.10}\text{Zn}_{0.90}\text{O}$ . Due to the large difference in atomic radii between Be and Zn, a limited Be incorporation ( $\sim 10\%$ ) into wurtzite ZnO host lattice has been reported<sup>39,41</sup>, beyond which these potential factors reduce the structural quality. The significantly improved structural quality of the quaternary alloy suggests enhanced incorporation of both Be and Mg on the cation sites of the wurtzite ZnO host lattice, which leads to a wider range of bandgap modulation for BeMgZnO as compared to ternary BeZnO or MgZnO compounds with an additional benefit of higher crystal quality than that of BeZnO<sup>41</sup>.



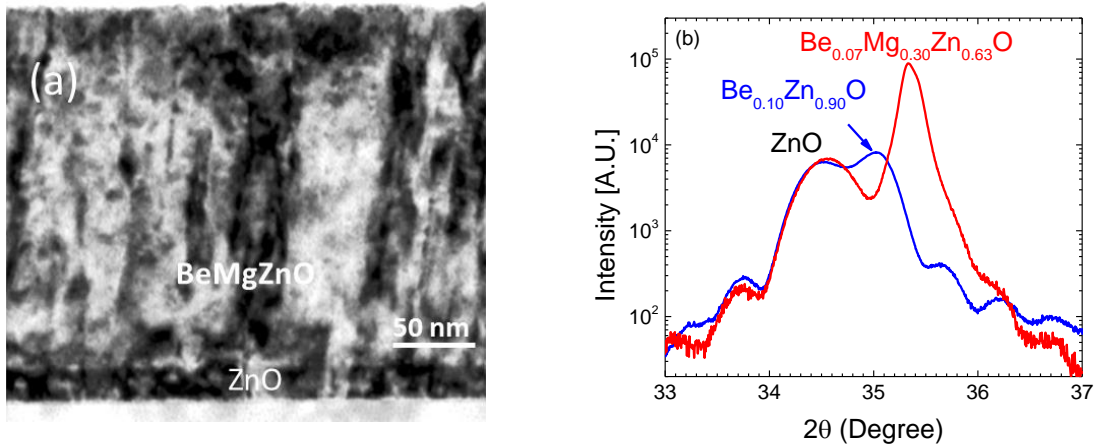


Figure 16: (a) Cross-sectional TEM image of  $\text{Be}_{0.07}\text{Mg}_{0.30}\text{Zn}_{0.63}\text{O}/\text{ZnO}$  structure showing a large density of threading dislocations ( $\sim 10^{10} \text{ cm}^{-2}$ ). (b) HRXRD  $2\theta$ - $\omega$  scans of 0002 reflection from  $\text{Be}_{0.10}\text{Zn}_{0.90}\text{O}/\text{ZnO}$  and  $\text{Be}_{0.07}\text{Mg}_{0.30}\text{Zn}_{0.63}\text{O}/\text{ZnO}$  structures.

### 3.3 Growth kinetics of O-polar BeMgZnO on (0001) GaN/sapphire template

O-polar  $\text{Be}_x\text{Mg}_y\text{Zn}_{1-x-y}\text{O}/\text{ZnO}$  heterostructures were grown on (0001) GaN/sapphire template using plasma enhanced molecular beam epitaxy (P-MBE). Highly resistive, carbon-compensated 2.5- $\mu\text{m}$  Ga-polar GaN layers were grown by metal-organic chemical vapor deposition on (0001) sapphire for this work. Prior to the growth of quaternary  $\text{Be}_x\text{Mg}_y\text{Zn}_{1-x-y}\text{O}$ , the polarity of ZnO buffers has been inverted from Zn-polar to O-polar by employing high VI/II ratio during nucleation<sup>14</sup>. The nucleation procedure is described below in more detail. Knudsen cells were used to evaporate Zn, Be, and Mg, and a radio frequency plasma source was used for reactive oxygen. Following a thermal cleaning at 625 °C for 15 minute, GaN was exposed to a Zn beam to terminate the surface with Zn adatoms. A 25 nm O-polar ZnO was then nucleated at 300 °C by maintaining high oxygen to zinc ratio (VI/II = 6) to ensure polarity inversion<sup>14</sup>. This was followed by annealing at 730 °C for 5 minutes at a reactor pressure of  $1 \times 10^{-5}$  Torr with closed oxygen plasma shutter, and a 130 nm thick ZnO buffer layer was then grown at 670 °C under oxygen rich growth conditions (VI/II ratio 6.0). The growth of a 75 nm thick quaternary

Be<sub>x</sub>Mg<sub>y</sub>Zn<sub>1-x-y</sub>O layer was initiated under oxygen rich environment at a reactor pressure  $1.5 \times 10^{-5}$  Torr.

### 3.3.1 Growth kinetics of BeMgZnO at temperature range 450° -500 °C:

In this work, two sets of samples grown at substrate temperatures of 475°C (series B) and 500 °C (series C) were compared to a control sample A grown at 450 °C. The growth conditions of samples studied are summarized in Table I. The reference sample A was grown with a Zn to (Be + Mg) ratio,  $J_r$ , of 3.9. In the first set (series B),  $J_r$  was varied from 3.9 (sample B1) to 6.2 (sample B3). For sample B2, the metal flux ratio was increased to 5, thus 29% higher compared to sample B1 or the reference sample A, by increasing Zn flux from 58 nm/h to 74 nm/h. For sample B3, the  $J_r$  ratio was further increased to 6.2, thus 59% higher compared to B1 or A, by keeping Zn flux at 74 nm/h and decreasing Be and Mg fluxes from 3 nm/h to 2 nm/h and 12 nm/h to 10 nm/h, respectively. The second set of samples (series C) was grown at 500 °C. The Zn to (Be + Mg) flux ratio was 3.9 for sample C1 (the same for sample A and B1), and for samples C2, C3 and C4, the ratio was kept 52% ( $J_r = 5.9$ ), 90% ( $J_r = 7.4$ ) and 115% ( $J_r = 8.3$ ) higher than that of sample C1 or A. For sample C2, Zn flux was increased from 58 nm/h to 88 nm/h while Be and Mg fluxes were kept same as sample C1. In sample C3, keeping the Zn flux at 88 nm/h, Be and Mg fluxes were reduced from 3 to 2 nm/h and 12 to 10 nm/h, respectively. For sample C4, the flux ratio was further increased by increasing Zn flux up to 100 nm/h. The growth time for all the quaternary samples was 1 hour. The growth rates, measured using a profilometer, are listed in Table I. With increasing substrate temperature the desorption rate of primarily Zn adatoms increases as Zn has much higher equilibrium vapor pressure (0.3 to 1 Torr) compared to Mg (.01 to .06 Torr) and Be (less than  $1 \times 10^{-8}$  Torr) within the temperature range explored.<sup>14</sup> As a result, the growth rate was reduced from 80 nm/h for sample A grown at 450 °C

to 70 nm/h for sample C1 grown at 500 °C under the same metal fluxes, consistent with the findings of Ivanov et al.<sup>15</sup>, who reported a 10% reduction within the same temperature range. Reflection High Energy Electron Diffraction (RHEED) was used to monitor *in situ* growth progression. High-resolution X-Ray diffraction (HRXRD) (Omega-2theta scans of 0002 reflection) was employed to evaluate structural quality of the Be<sub>x</sub>Mg<sub>y</sub>Zn<sub>1-x-y</sub>O alloy. Steady-state PL measurements were performed at 15 K in order to obtain emission spectra from Be<sub>x</sub>Mg<sub>y</sub>Zn<sub>1-x-y</sub>O quaternary using a frequency tripled Ti:sapphire laser (266 nm wavelength, 150 fs pulse width, 80 MHz repetition rate) as an excitation source. Be and Mg contents were estimated from the *c* lattice parameter obtained from HRXRD analysis and bandgap was measured from low temperature PL considering Stokes shift, with previously established Vegard's law with bowing parameters for the full range of compositions.<sup>6,16,17</sup> Metal fluxes were measured by using quartz thickness monitor.

Table I: Be<sub>x</sub>Mg<sub>y</sub>Zn<sub>1-x-y</sub>O growth temperature ( $T_g$ ), Zn ( $J_{Zn}$ ), Mg ( $J_{Mg}$ ), and Be ( $J_{Be}$ ) metal fluxes and their ratios,  $J_r = J_{Zn} / (J_{Be} + J_{Mg})$  and growth rate of the quaternary samples included in this study.

Sample number	$T_g$ °C	$J_{Zn}$ nm/h	$J_{Mg}$ nm/h	$J_{Be}$ nm/h	$J_r$	Growth rate nm/h
A	450	58	12	3	3.9	80 ± 10
B1	475	58	12	3	3.9	75 ± 10
B2	475	74	12	3	5.0	90 ± 10
B3	475	74	10	2	6.2	85 ± 10
C1	500	58	12	3	3.9	70 ± 10
C2	500	88	12	3	5.9	95 ± 10
C3	500	88	10	2	7.4	90 ± 10
C4	500	100	10	2	8.3	100 ± 10

Figure 17 (a) and (b) compare the double axis  $2\theta$ - $\omega$  scans of the 0002 reflection from two sets of Be<sub>x</sub>Mg<sub>y</sub>Zn<sub>1-x-y</sub>O /ZnO heterostructures grown at  $T_g = 475$  °C and 500 °C, respectively, with the reference sample A which was grown at 450 °C. As the quaternary alloy was grown on GaN

template, then deposited on a 300 nm AlN nucleation layer on sapphire using MOCVD technique, XRD reflection from GaN and AlN is observed at Bragg angle  $34.55^\circ$  and  $36.10^\circ$ , respectively. ZnO peak appears at the left shoulder of GaN peak, which is clearly resolved in triple axis scan shown in Figure 17 (c). The diffraction patterns from the first set ( $T_g = 475^\circ\text{C}$ ) are shown in Figure 17 (a). Although samples A and B1 were grown with the similar metal fluxes, the XRD pattern from sample B1, grown at substrate temperature increased by only  $25^\circ\text{C}$  from sample A, shows no reflection corresponding to the quaternary material whereas  $\text{Be}_{0.03}\text{Mg}_{0.25}\text{ZnO}$  peak at  $35.1^\circ$  is observed for sample A. Details of Be and Mg composition estimation have been described in the following paragraphs. Among the samples grown at  $475^\circ\text{C}$ , only sample B3 ( $J_r = 6.2$ ), which was grown with the Zn to (Be + Mg) flux ratio  $\sim 60\%$  higher than that of sample A or B1, shows reflection from the quaternary  $\text{Be}_{0.03}\text{Mg}_{0.20}\text{ZnO}$  alloy at  $35.03^\circ$ . An increase of Zn to (Be + Mg) ratio by 30% used for the growth of sample B2 ( $J_r = 5$ ) is not sufficient to obtain  $\text{Be}_x\text{Mg}_y\text{Zn}_{1-x-y}\text{O}$  of decent quality to register an XRD reflection. The second set of samples, grown at  $500^\circ\text{C}$ , exhibits a trend (Figure 17 (b)) similar to the first set ( $475^\circ\text{C}$ ). No reflection from the quaternary alloy is observed for sample C1 ( $J_r = 3.9$ ) and C2 ( $J_r = 5.9$ ), whereas a very weak reflection is recorded for sample C3 ( $J_r = 7.4$ ). XRD scan of sample C2 is not shown in Figure 17 (b) as it is similar to that of sample C1. Only sample C4 ( $J_r = 8.3$ ) which deposited with  $\sim 115\%$  higher Zn to (Be + Mg) ratio compared to sample A shows reflection from the quaternary  $\text{Be}_{0.03}\text{Mg}_{0.15}\text{ZnO}$  alloy. It should be noted that only the substrate temperature is varied among the samples A, B1 and C1, where only sample A shows reflection from the quaternary alloy. As shown in Figure 17 (c), to obtain similar intensity reflection from the quaternary alloy grown at  $T_g = 475^\circ\text{C}$  and  $500^\circ\text{C}$ , approximately 60% and 115 % higher Zn to (Be + Mg) flux ratio is required compared to the sample grown at  $T_g = 450^\circ\text{C}$ . Well

pronounced thickness interference fringes observed for samples are indicative of relatively smooth surface and BeMgZnO/ZnO interface. Additionally, a shift in ZnO peak position, observed in Figure 17 (c), is attributed to minor unintentional variations in either oxygen radical flux or Zn flux during the nucleation stage carried out at 300 °C. Consequently, ZnO peaks are not clearly distinguishable from the GaN peaks for samples B2, B3, C3, and C4. As reported elsewhere,<sup>14</sup> there is a strong correlation between the residual strain in the overgrown ZnO and the oxygen radical to Zn flux ratio during ZnO nucleation on GaN(0001)/ sapphire templates.

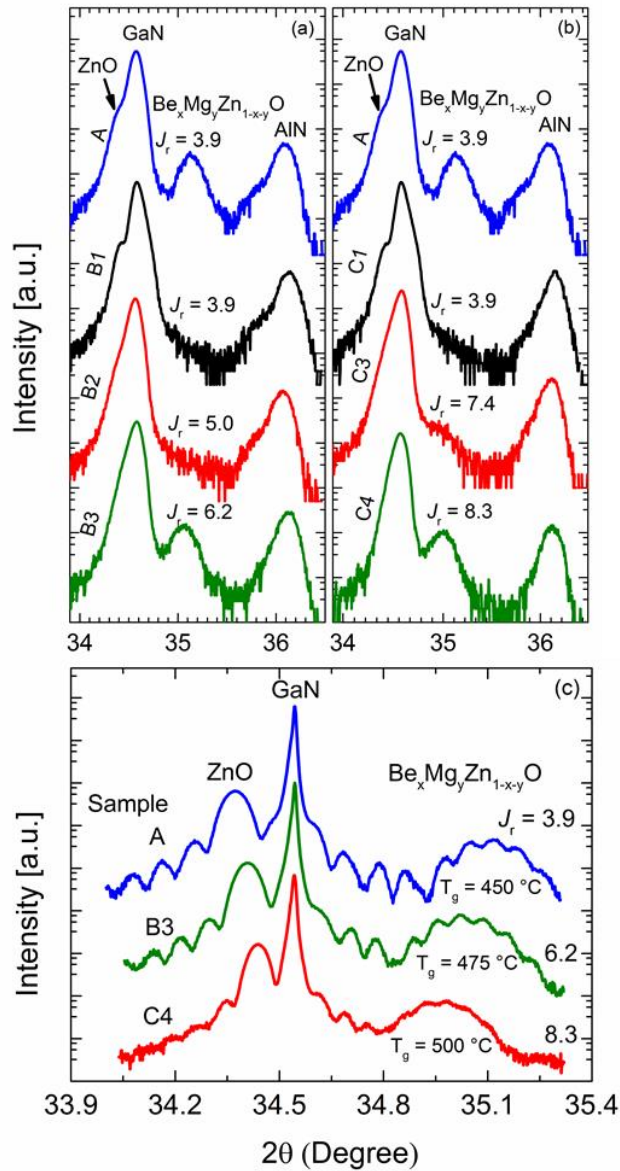


Figure 17: The Double axis  $2\theta$ - $\omega$  scans of the 0002 reflection for the samples grown using different Zn to Be and Mg flux ratios at (a) 475 °C and (b) 500 °C compared with that for reference sample A, which was grown at 450 °C. Figure (c) shows the triple axis scan of the single crystalline BeMgZnO grown at temperature range 450 °C to 500 °C.

Composition of  $\text{Be}_x\text{Mg}_y\text{Zn}_{1-x-y}\text{O}$  alloy is estimated by simultaneously solving the equations obtained from Vegard's law with bowing parameters for c lattice parameter and bandgap reported by Toporkov et al.<sup>6</sup> BeMgZnO was grown on thick GaN template which precludes measurement of the absorption edge of BeMgZnO. Optical bandgap has been estimated from 15K PL emission energy of the dominant peak considering large Stokes shift from quaternary alloy, as has been reported by Toporkov et al. Table II lists the c lattice parameter, energy of the dominant PL peak obtained through deconvolution (see Figure 19), estimated optical bandgap, and Mg and Be contents with error margins. The compositional error is associated mainly with the bandgap estimation from Stokes shift and the statistical error while fitting the PL and XRD peaks assuming Gaussian profiles. As listed in the table, Mg composition of the BeMgZnO reduces from 25% to 15% while increasing the Zn / (Be + Mg) ratio from 3.9 to 8.3 to obtain single crystalline BeMgZnO in the temperature ranging from 450 °C to 500 °C. Reduction of Mg incorporation into  $\text{Be}_x\text{Mg}_y\text{Zn}_{1-x-y}\text{O}$  lattice is expected at higher growth temperatures due to the much lower equilibrium solubility limit (~4%) of MgO into wurtzite ZnO lattice.<sup>18</sup> Be incorporation at higher growth temperature also reduces slightly as the Be flux used in this work is relatively small.

Table II: *c* lattice parameters, energy (EPL) of the dominant PL peak measured at 15 K, optical bandgaps (E<sub>g</sub>) and Be and Mg compositions for the crystalline BeMgZnO samples

Sample No.	<i>c</i> lattice parameter Å	Energy of dominant PL peak, E <sub>PL</sub> , eV	Bandgap E <sub>g</sub> eV	Mg composition %	Be composition %
A	5.109 ± 0.005	3.782 ± 0.002	3.930 ± 0.1	25 ± 1	3 ± 1
B3	5.121 ± 0.005	3.750 ± 0.002	3.882 ± 0.1	20 ± 1	3 ± 1
C4	5.129 ± 0.005	3.554 ± 0.002	3.602 ± 0.1	15 ± 1	2.5 ± 1

Table III compares the *c* lattice parameter, PL emission energy and optical bandgap of the BeMgZnO quaternary alloys discussed in the current study with those of the reported MgZnO ternary alloys.<sup>19–23</sup> In this work, even the largest *c* lattice parameter among the samples is about 5.129 Å with only ~ 15% Mg and ~ 3% Be (Sample C4) resulting in optical bandgap of 3.60 eV, which is inconsistent with the wurtzite MgZnO alloy. The smallest *c* lattice parameter reported for wurtzite MgZnO by Du et al.<sup>24</sup> is 5.136 Å for the material containing 55% Mg grown at 250 °C with a bandgap of 4.55 eV. Note that Mg incorporation into wurtzite MgZnO alloy reduces with increasing growth temperature because of the segregation of MgO rich phase.<sup>19–21,25</sup> The difference between the lattice parameters in our work (<5.129 Å) and the values reported by Ohtomo et al. (5.182 Å, [Ref.19]) and Nishimoto et al. (5.165, [Ref. 20]) for 25% Mg is far beyond any experimental error. The reduction in the *c* lattice parameter with respect to MgZnO found here is governed by its co-alloying with BeO, as it has a substantially smaller *c* lattice parameter (4.3776 Å [Ref. 10]) compared to wurtzite MgO (5.095 Å [Ref. 26]). Thus the effect of Be incorporation into the ZnO lattice is unequivocally shown by the significant reduction in the *c* lattice parameter. It is worth noting that the difference between the lattice parameters (see

Table III) for a given Mg composition in MgZnO alloy could originate from different strain conditions in the films caused by the employment of different growth techniques and substrates for the epitaxial growth. Additionally, for 25% Mg, Takagi et al.<sup>22</sup> and Laumer et al.<sup>23</sup> reported MgZnO bandgap of 3.743 eV and 3.818 eV, respectively, whereas we have found the larger value of  $3.930 \pm 0.1$  eV (Sample A), which is also consistent with Be incorporation into wurtzite lattice.

Table III: Comparison of *c* lattice parameters, PL emission energies and optical bandgaps of the crystalline Be<sub>0.03</sub>Mg<sub>y</sub>Zn<sub>0.97-y</sub>O alloys discussed here with relevant reported MgZnO thin films of similar Mg composition.

Mg composition %	<i>c</i> lattice parameter Å	PL emission energy, E <sub>PL</sub> , eV	Optical Bandgap, E <sub>g</sub> , eV
25 (This work)	5.109 ± 0.005	3.782 ± 0.002	3.930 ± 0.1
	5.182 <sup>a</sup>	-	3.743 <sup>d</sup>
	5.165 <sup>b</sup>	3.717 <sup>c</sup>	3.818 <sup>c</sup>
	5.121 ± 0.005	3.750 ± 0.002	3.882 ± 0.1
20 (This work)	5.183 <sup>a</sup>	-	3.657 <sup>d</sup>
	5.170 <sup>b</sup>	3.65 <sup>c</sup>	3.728 <sup>c</sup>
	5.129 ± 0.005	3.554 ± 0.002	3.602 ± 0.1
	5.190 <sup>a</sup>	-	3.554 <sup>d</sup>
15 (This work)	5.175 <sup>b</sup>	3.576 <sup>c</sup>	3.640 <sup>c</sup>

<sup>a</sup> Ohtomo et al. [Ref. 19]

<sup>b</sup> Nishimoto et al [Ref. 20]

<sup>c</sup> Laumer et al. [Ref. 23]

<sup>d</sup> Takagi et al [Ref. 22]

Time evolution of RHEED patterns from Be<sub>x</sub>Mg<sub>y</sub>Zn<sub>1-y</sub>O films grown with different Zn to (Be + Mg) flux ratios at different substrate temperatures is shown in Figure 18. Figure 18 (a) and 2 (b) exhibit the RHEED evolution at 20 min and 60 min, respectively, of the quaternary growth of



sample A ( $T_g = 450\text{ }^\circ\text{C}$ ). The spotty diffraction pattern at 20 min indicates a three dimensional growth mode, which remains unchanged until the end of the growth. The RHEED pattern from sample B1 at 20 min of growth (Figure 18 (c)), grown at  $475\text{ }^\circ\text{C}$ , where substrate temperature is the only parameter varied compared to sample A, indicates formation of a second phase on the growing surface. Reflections from the new phase become dominant at 60 min of growth as the separation between RHEED reflections reduces (Figure 18 (d)), compared to the RHEED pattern recorded from sample A (Figure 17 (b)). The substantial reduction in spacing between RHEED reflections, i.e., the increase in in-plane lattice parameter compared to the  $\text{Be}_{0.03}\text{Mg}_{0.25}\text{ZnO}$  layer of reference sample A suggests an initiation of second phase on the growing surface. Sample B2, where Zn to (Be + Mg) ratio is 30% higher than that of B1 does not show obvious signature of second-phase formation at 20 min. However, the elongated reflection spots tend to incline (Figure 18 (f)), as observed at 60 min of growth, which is a characteristic of increased misorientation of grains with respect to  $c$ -axis (the onset of textured growth).<sup>27</sup> The 20-min RHEED pattern from sample B3, grown with Zn to (Be + Mg) flux ratio approximately 60% higher than that used for B1, exhibits elliptical shape reflections (Figure 18 (g)) and the pattern remains unchanged until the end of the growth (Figure 18 (h)). These observations are in agreement with XRD data, as seen from Figure 17 (a), except for sample B3, no 0002 reflection from  $\text{Be}_x\text{Mg}_y\text{Zn}_{1-x-y}\text{O}$  is found for the samples from the first set. The RHEED patterns for the samples grown at  $500\text{ }^\circ\text{C}$  (series C) are shown in Figure 18 (i) to 2 (n). For sample C1, where only the growth temperature is further increased compared to samples A or B1, the degree of deformation of spotty pattern at 20 min into the growth (Figure 18 (i)) is even higher compared to sample B1 ( $T_g = 475\text{ }^\circ\text{C}$ ), indicating faster progression of the RHEED pattern. An increase in in-plane lattice parameter observed at 60 min (Figure 18 (j)), suggests the formation of a second phase on

the growing surface. RHEED progression for samples C2 and C3 (C2 is not shown in the figure) grown with the Zn to (Be + Mg) ratios increased by 52% and 90% respectively, compared to samples A or C1 are similar. For sample C3, although the 20-min RHEED pattern (Figure 18 (k)) does not reveal the formation of second phase, the 60-min pattern (Figure 18 (l)) shows elliptical spots at the onset of inclination (Figure 18 (l)) which indicate a textured growth of  $\text{Be}_x\text{Mg}_y\text{Zn}_{1-x-y}\text{O}$ . A further increase in Zn / (Be + Mg) ratio (~115% of sample A or C1) for sample C4 results in elliptical shape reflections at the 60 min of the growth, which is in agreement with X-ray diffraction (Figure 18 (b)). Therefore, in order to obtain a single phase quaternary alloy at higher growth temperature, high Zn to (Be + Mg) flux ratio is required, the higher the growth temperature, the higher the ratio necessary.

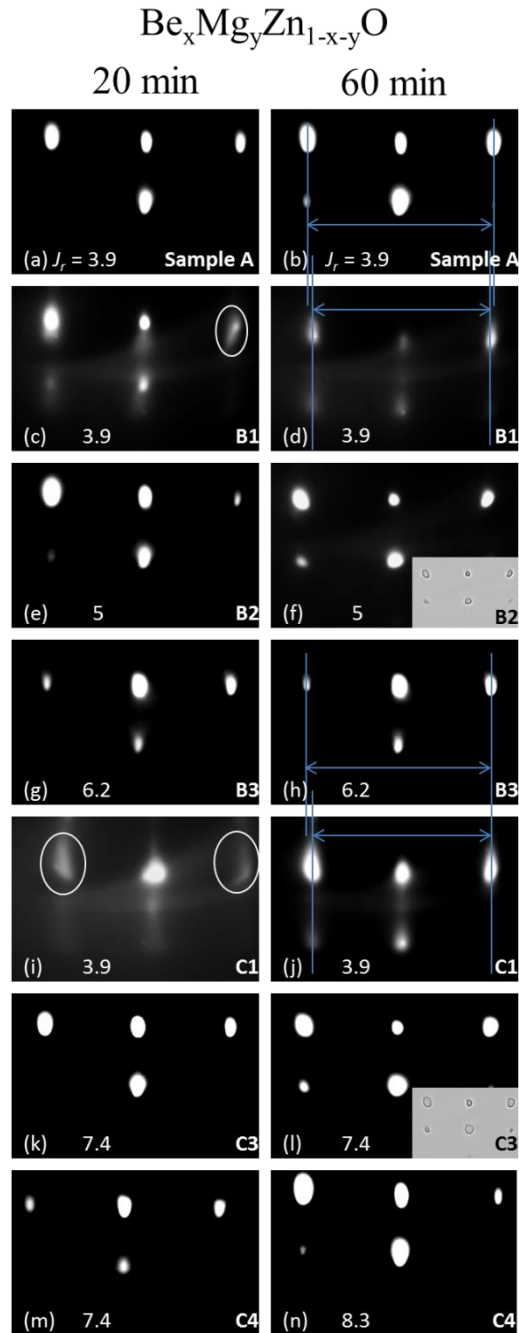


Figure 18: Left and right column shows the RHEED image taken along [1-100] azimuthal direction after 20 min and 60 min growth of  $\text{Be}_x\text{Mg}_y\text{Zn}_{1-x-y}\text{O}$  respectively. Figure (a) & (b) are for the sample A grown at  $T_g = 450^\circ\text{C}$ , figure (c) to (h) are for  $T_g = 475^\circ\text{C}$  (samples B1, B2, and B3) and figure (i) to (n) are for  $T_g = 500^\circ\text{C}$  (samples C1, C3, and C4). Zn to (Be + Mg) flux ratios ( $J_r$ ) are indicated on each figure.

### 3.3.2 Thermodynamic limitation of Mg and Be incorporation:

Figure 19 shows the PL spectra measured at 15 K. Emission energies were obtained through deconvolution using three Gaussian peaks, the results of which are shown in insets of Figure 19 (a) and (b) for samples B2 and C2, respectively. Following the deconvolution, integrated intensities of the individual peaks are shown in Figure 19 (c) for series B (squares) and C samples (circles) as a function of Zn / (Be + Mg) ratio. Among the samples in series B deposited at 475 °C, the dominant emission at ~ 3.75 eV is at least a factor of four brighter for sample B3 with  $J_r = 6.2$  than that for sample B1 with  $J_r = 3.9$ . Similar trend is observed for the samples grown at 500 °C. Sample C1 grown with  $J_r = 3.9$  does not show any emission originating from  $\text{Be}_x\text{Mg}_y\text{Zn}_{1-x-y}\text{O}$ , while the integrated intensity of the dominant 3.55 eV peak increases at least a factor of two from sample C2 to sample C4 with increasing Zn / (Be + Mg) ratio from 5.9 to 8.3. The increase in peak intensity together with a decrease in full-width at half maximum (FWHM) suggests reduced density of non-radiative recombination centers in the quaternary alloy. We speculate that these centers are primarily point defects. Therefore, increasing Zn to (Be + Mg) ratio enhances the optical quality consistently for both series of samples. Secondary emission peaks (3.95 eV and 3.60 eV for B samples, 3.67 eV and 3.46 eV for series C samples) occurring on both shoulders of the dominant one (3.75 eV for series B samples, 3.55 eV for series C samples), most likely originate from inclusions with different compositions within the quaternary matrix. These peaks are expected to diminish or merge into a single peak as the distribution of metal constituents becomes more homogeneous with increasing Zn flux, which would also result in slight shrinkage of the bandgap.

The energy of the dominant emission (Figure 19 (b)) from samples grown at 500 °C (series C) are red shifted (~3.55 eV) compared to the samples grown at 475 °C (series B) emitting at ~3.75

eV (Figure 19 (a)). This is clearly due to the reduction of mainly Mg incorporation into the wurtzite  $\text{Be}_x\text{Mg}_y\text{Zn}_{1-x-y}\text{O}$  lattice at higher growth temperature. However it is important to note that emission from the dominant peak appears almost at the same energy for a set of samples grown at the same temperature, although the Zn to (Mg + Be) ratio is increased by a substantial amount. For the samples of series B, dominant emission occurs near 3.75 eV, although the Zn to (Mg + Be) flux ratio is increased by as much as 60%. Similarly, for the samples grown at 500 °C (series C), dominant emission occurs at ~3.55 eV, although the flux ratio has been increased up to ~115%. This phenomenon can be explained by a limitation of Mg and/or Be incorporation to the wurtzite  $\text{Be}_x\text{Mg}_y\text{Zn}_{1-x-y}\text{O}$  lattice set by the growth kinetics as is discussed below.

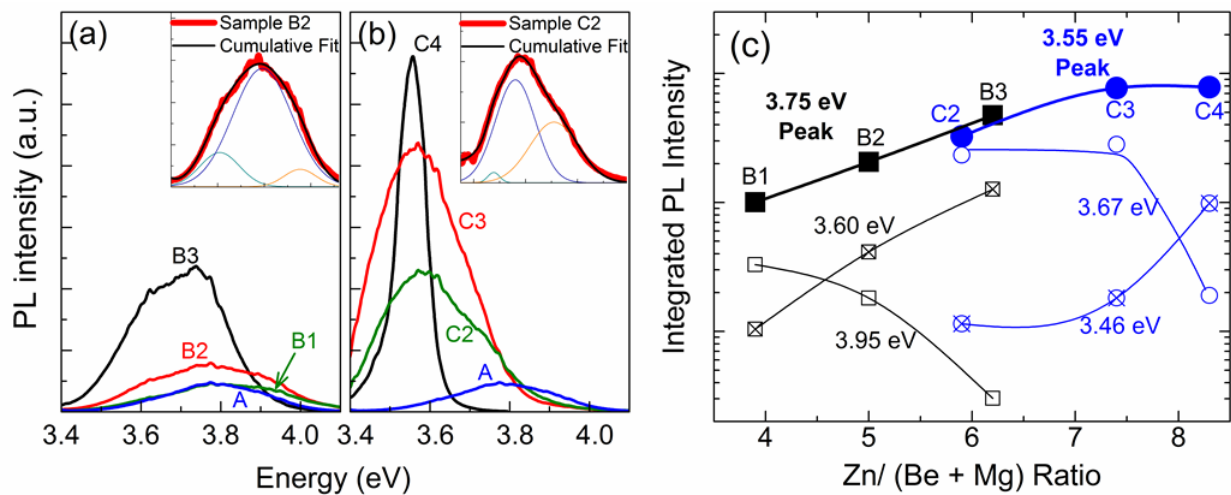


Figure 19: 15 K PL spectra from quaternary samples grown at (a) 475°C and (b) 500°C along with reference sample A grown at 450°C. As examples, insets show the deconvolution of spectra into three Gaussian peaks for (a) sample B2 and (b) sample C2. Figure (c) shows the effect of Zn / (Be + Mg) ratio on the integrated intensity of different emission peaks. Rectangular and circular symbols represent series B and series C samples, respectively. Solid lines are used as guides to the eye

Formation of a second phase is clearly evidenced by the evolution of RHEED patterns for sample B1 and C1, (Figure 18 (d) and (j), respectively), where the spacing between reflection spots is reduced compared to the single homogeneous  $\text{BeMgZnO}$  (sample A). Assuming a hexagonal structure, we have calculated interplanar distances from RHEED reflections taken

along [1-100] azimuthal direction for samples B1 and C1 as  $1.66 \pm 0.01 \text{ \AA}$  and  $1.67 \pm 0.01 \text{ \AA}$ , respectively. These values are reasonably consistent with the hypothetical interplanar distance ( $1.66 \text{ \AA}$ ) of metastable wurtzite MgO ( $a$  lattice parameter  $3.32 \text{ \AA}$ , [Ref. 6]). It is important to note that the interplanar distance of wurtzite BeO ( $1.35 \text{ \AA}$ ) is even lower than that of ZnO ( $1.63 \text{ \AA}$ ). In addition, the interplanar distances of  $1.42 \text{ \AA}$  and  $2.07 \text{ \AA}$  measured from 220 and 200 RHEED reflections, respectively, for a (001)-oriented cubic MgO grown on ZnO (0001) template in our previous work<sup>28</sup>, also rule out any possible cubic phase in samples B1 and C1. Moreover, reduction of spacing between RHEED spots has also been observed by Vashaei *et al.*<sup>29</sup> at the onset of MgO-rich wurtzite MgZnO phase separation for relatively high Mg / (Mg + Zn) ratio. However, no reflection from MgO-rich alloy was noted in the XRD scans, most plausibly due to insufficient sensitivity of our conventional XRD system.

To delve more into the abovementioned phase separation at higher substrate temperature, we must consider both thermodynamic (formation enthalpy) and kinetic (mobility of adatoms) factors. Formation enthalpy of hypothetical wurtzite MgO is calculated to be  $-5.678 \text{ eV}$  by using exchange tuned Heyd-Scuseria-Ernzerhof (HSE) hybrid functional, details of which are discussed in a future report.<sup>30</sup> The more negative formation enthalpy of wurtzite MgO compared to wurtzite ZnO ( $-3.632 \text{ eV}$ )<sup>31</sup>, and the increased surface mobility of Mg adatoms at higher growth temperatures, make the formation of wurtzite MgO-rich alloys more favorable. Additionally, nearly constant PL emission energy of the dominant peak for the samples grown at the same temperature ( $3.75 \text{ eV}$  and  $3.55 \text{ eV}$  for  $T_g = 475 \text{ }^\circ\text{C}$  and  $T_g = 500 \text{ }^\circ\text{C}$ , respectively) despite the variation of Zn / (Be + Mg) ratio in a wide range, suggests temperature controlled incorporation of Mg and possibly Be into the wurtzite  $\text{Be}_x\text{Mg}_y\text{Zn}_{1-x-y}\text{O}$  lattice. The reduced

surface mobility of Mg adatoms at relatively low growth temperatures decreases the probability of MgO-rich phase preventing the formation of MgO clusters. When the growth temperature increases, the density of Mg adatoms on the growing surface should be reduced in order to achieve single-phase material.

## Chapter 4. Zn polar BeMgZnO / ZnO heterostructure with 2DEG:

### 4.1 Introduction:

Accumulation of non-equilibrium hot longitudinal optical (LO) phonons for devices operation under high electric field, plays an adverse role. As the supplied electric power is dissipated mainly through electron –phonons coupling, it reduces the electron drift velocity.<sup>78-80</sup> Fast electron energy relaxation<sup>81</sup> and hence high electron drift velocity can be achieved through ultrafast decay of hot phonons via plasmon-LO phonon resonance<sup>82,83</sup>. Plasmon-LO phonon resonance occurs when

$$\hbar\omega_{phonon} \approx \hbar\omega_{plasmon}$$

with the plasmon frequency for 2D system described by<sup>84</sup>

$$\omega_{plasmon} = (e^2 n / m^* \epsilon)^{1/2}$$

where  $\hbar$ ,  $\omega$ ,  $e$ ,  $m^*$ ,  $\epsilon$ , and  $n$  are the reduced Planck constant, the frequency, the electron effective mass, the dielectric constant and the electron density, respectively. This translates to the resonance occurring at  $\sim 10^{19} \text{ cm}^{-3}$  for GaN (LO phonon energy of 90 meV) corresponding to a 2DEG density of  $\sim 9.4 \times 10^{12} \text{ cm}^{-2}$ . For ZnO having an LO phonon energy of 72 meV, the resonance electron density is  $\sim 7 \times 10^{18} \text{ cm}^{-3}$ .<sup>81</sup> Clearly, this electron density is impractical for bulk ZnO based thin film transistor. ZnO based HFETs with 2DEG operating near the



abovementioned resonance in ZnO is possible providing that the said high sheet electron concentration can be obtained.

So far MgZnO has been only considered for as barrier layer in ZnO based HFET structure. Such HFET structures with  $Mg_xZn_{1-x}O$  barriers have been reported to exhibit low-temperature mobilities as high as  $10^6$  cm<sup>2</sup>/V-s and unusual fractional quantum Hall effect under high magnetic fields<sup>85,86</sup> The limitation associated with the use of wurtzite  $Mg_xZn_{1-x}O$  barriers in heterostructures is the partial cancelation of spontaneous and piezoelectric polarizations caused by compressive strain in the  $Mg_xZn_{1-x}O$  barriers due to its higher in-plane lattice parameter (theoretical wurtzite MgO  $a$  lattice parameter 3.32 Å [Ref. <sup>50</sup>]) compared to ZnO (3.25 Å [Ref. <sup>50</sup>]) that limits achievable densities of 2-dimensional electron gas (2DEG) to below  $8 \times 10^{12}$  cm<sup>-2</sup> cm<sup>-2</sup>.<sup>87</sup> with moderate Mg content less than 40%,<sup>88</sup> Specifically, this level of 2DEG concentration can only be achieved by employing MgZnO barriers with very high Mg content through growth under low substrate temperatures (300 °C or less),<sup>31,36</sup> while such structures are prone to degradation under thermal treatments and under high current operations.

Because the in-plane lattice parameter,  $a$ , increases and decreases with increasing Mg and Be content (BeO  $a$  lattice parameter 2.698 Å [Ref. <sup>51</sup>]), respectively, the amount and sign of strain can be controlled by tuning the in-plane lattice parameter in BeO-MgO-ZnO solid solutions in a wide range by varying the Be/Mg ratio. Moreover, at a given temperature, co-alloying of ZnO with BeO and MgO helps each other towards an enhanced incorporation of both Be and Mg into the lattice with a better structural quality compared to their respective ternaries<sup>41</sup>. Switching the strain sign from compressive to tensile through the incorporation of Be into wurtzite lattice changes the direction of piezoelectric polarization, thus paving the way for the piezoelectric and spontaneous polarizations to be additive. Therefore, as expected, in ZnO based HFET structure,

using  $\text{Be}_x\text{Mg}_y\text{Zn}_{1-x-y}\text{O}$  as a barrier with a small amount of Be (<5%) and relatively lower Mg content (~30%), one can achieve similar 2DEG sheet carrier density ( $10^{13} \text{ cm}^{-2}$ ) which otherwise would require very high Mg content (60%) in  $\text{Mg}_x\text{Zn}_{1-x}\text{O} / \text{ZnO}$  HFET structures<sup>88</sup>. This opens the path for  $\text{Be}_x\text{Mg}_y\text{Zn}_{1-x-y}\text{O}$  growth at higher temperature with relatively lower Mg content; therefore, for achieving relatively high material quality.

We have calculated the 2 DEG sheet carrier density for both Zn-polar and O-polar ZnO for Both  $\text{BeMgZnO}$  and  $\text{MgZnO}$  as barrier considering respective piezoelectric and spontaneous polarization. Our experimentally found densities agree well the theoretical consideration.

#### 4.2 Calculation of sheet carrier density:

Figure 20 shows the HFET structure of Zn polar (Figure 20 (a) & (b)) and O polar (Figure 20 (c) & (d)) for both  $\text{BeMgZnO}$  (Figure 20 (a) & (c)) and  $\text{MgZnO}$  (Figure (b) & (d)) as barrier. Two dimensional electron gas (2DEG) channel, shown as dashed line, form at the heterointerface into the ZnO layer. Spontaneous polarization ( $P_{\text{SP}}$ ), always directed towards  $[000\bar{1}]$  direction, obtained due to different ionicity at the heterointerface. The direction of the strain induced piezoelectric polarization depends on the sign of strain. As shown in Figure 3,  $\text{MgZnO}$  has higher in plane,  $a$ , lattice parameter, when compared to  $\text{ZnO}$ , while by incorporating Be one can obtain smaller  $a$  lattice parameter from quaternary  $\text{BeMgZnO}$  alloy. As a result, thin (20 nm)  $\text{BeMgZnO}$  and  $\text{MgZnO}$  barrier layers in Zn polar HFET structure shown in Figure 20 (a) and (b), respectively, are under tensile and compressive biaxial strain. Therefore, piezoelectric polarization of quaternary  $\text{BeMgZnO}$  (Figure 20 (a)) directs toward  $[000\bar{1}]$  direction<sup>89</sup>, thus summing up with spontaneous polarization. On the other hand, piezoelectric polarization of compressively strained  $\text{MgZnO}$  (Figure 20 (b)) has an opposite direction with respect to spontaneous polarization, thus reducing the net polarization charge. In both cases, piezoelectric

polarization of ZnO is annulled due to the strain relaxation as the film thickness is relatively high (400 nm). However, in the O polar ZnO / BeMgZnO HFET structure (Figure 20 (c)), piezoelectric polarization of ZnO, works along [0001] direction<sup>89</sup> as ZnO under compressive biaxial strain, while for the ZnO / MgZnO heterostructure (Figure 20 (d)), it works opposite to [0001] direction due to tensile strained ZnO. Piezoelectric polarization of BeMgZnO

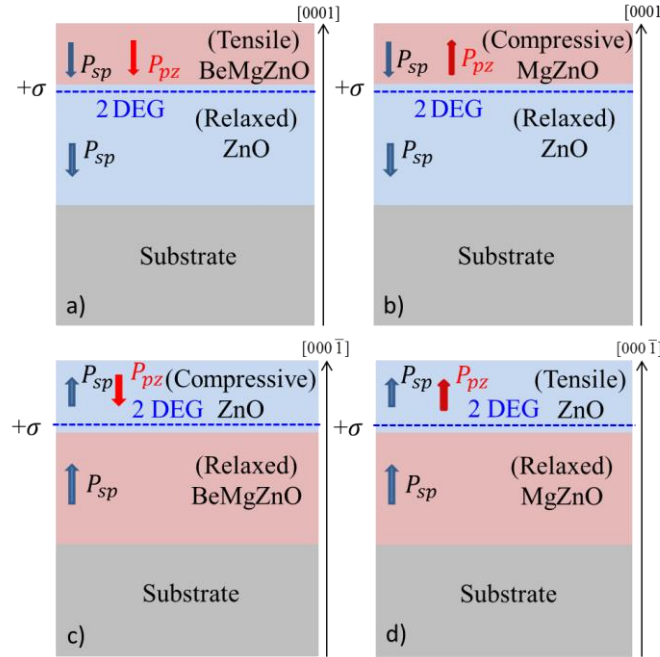


Figure 20: Polarization induced sheet charge density and directions of the piezoelectric and spontaneous polarization of Zn polar (a) BeMgZnO / ZnO, (b) MgZnO / ZnO and O-polar (c) ZnO / BeMgZnO, (d) ZnO/ MgZnO heterostructure

and MgZnO is zero due to strain relaxation of relatively thicker film. Figure 21 shows the calculated 2DEG sheet carrier density from the Zn polar HFET structures as a function of Mg incorporation for both  $Be_xMg_yZn_{1-x-y}O$  and  $Mg_yZn_{1-y}O$  barrier for Be content from 1 to 3%.

Polarization induced sheet carrier density is calculated by using the following equation

$$|\sigma| = |P_{sp}(Be_xMg_yZn_{1-x-y}O) + P_{pe}(Be_xMg_yZn_{1-x-y}O) - P_{sp}(ZnO)|$$

Lattice parameters, piezoelectric constants, elastic constant and spontaneous polarization values of BeO, MgO and ZnO used for the carrier density calculation are presented in t generation is not considered.

Table IV. Lattice parameter of the quaternary and ternary alloys are calculated using the Vegard's law, while piezoelectric and elastic constant and spontaneous polarization are estimated with linear approximation of Be and Mg composition. As seen from Figure 21, almost factor two higher sheet carrier density is expected from Be<sub>0.02</sub>Mg<sub>0.30</sub> ZnO / ZnO HFET structure compared to Mg<sub>0.30</sub> ZnO / ZnO due to the subtraction of piezoelectric component from the spontaneous polarization in the latter case. Theoretically, similar trend of 2DEG sheet carrier is expected from O-polar structures if technological limitation which includes growth quality and defect generation is not considered.

Table IV: a lattice parameters, elastic (C) and piezoelectric (e) constants, spontaneous polarization (PSP) of BeO, MgO and ZnO.

	BeO	MgO	ZnO
<i>a</i> Lattice parameter (Å)	2.698 <sup>a</sup>	3.30 <sup>c</sup>	3.250 <sup>b</sup>
C <sub>33</sub> (Gpa)	488 <sup>a</sup>	109 <sup>d</sup>	211 <sup>b</sup>
C <sub>31</sub> (Gpa)	77 <sup>a</sup>	58 <sup>d</sup>	105 <sup>b</sup>
e <sub>33</sub> * [C/m <sup>2</sup> ]	0.02 <sup>a</sup>	1.64 <sup>d</sup>	1.22 <sup>b</sup>
e <sub>31</sub> [C/m <sup>2</sup> ]	-0.02 <sup>a</sup>	-0.58 <sup>d</sup>	-0.51 <sup>b</sup>
P <sub>sp</sub> [C/m <sup>2</sup> ]	-0.045 <sup>a</sup>	-0.123 <sup>f</sup>	-0.053 <sup>e</sup>

<sup>a</sup>ref.<sup>90</sup> <sup>b</sup>ref.<sup>91</sup> <sup>c</sup>ref.<sup>92</sup> <sup>d</sup>ref.<sup>93</sup> <sup>e</sup>ref.<sup>94</sup> <sup>f</sup>ref.<sup>95</sup>

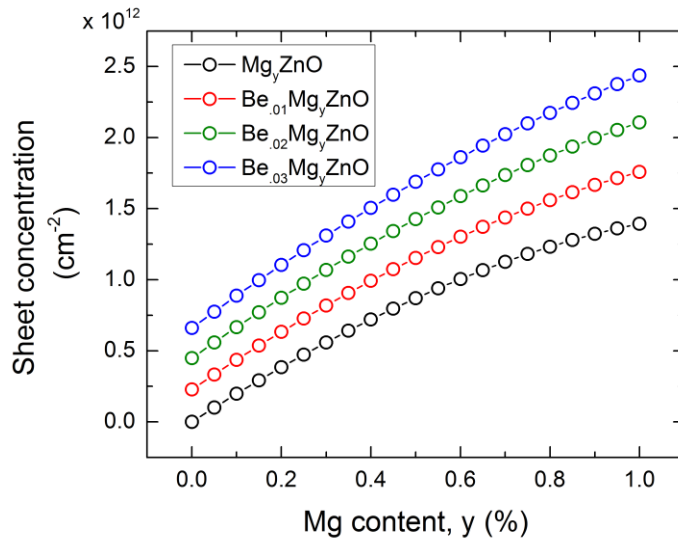


Figure 21: Calculated 2DEG sheet charge density of Zn-polar HFET structures with  $\text{Be}_x\text{Mg}_y\text{Zn}_{0.97-y}\text{O}$  with  $x = 0-3$  and  $\text{Mg}_y\text{Zn}_{1-y}\text{O}$  barriers as a function of Mg composition.

### 4.3 Experimental results:

We have investigated electrical properties of Zn-polar  $\text{BeMgZnO}/\text{ZnO}$  heterostructure grown on GaN (0001)/*c*-sapphire templates. Figure 23 (a) and b (b) compare the temperature dependence of mobility and sheet carrier density in  $\text{Be}_x\text{Mg}_y\text{Zn}_{1-x-y}\text{O}/\text{ZnO}$  heterostructure described in Table V. Sheet carrier density of all three samples was decreased by  $\sim 2.4 \times 10^{12} \text{ cm}^{-2}$  when the temperature was decreased from 293 K to 100K. This decrease in sheet density is attributed to the parallel bulk conduction channel originated from the defective LT-ZnO layer, HT-ZnO layer and also the  $\text{BeMgZnO}$  barrier, if any. Similar reduction in sheet carrier concentrations with decreasing temperature was also reported for  $\text{MgZnO}/\text{ZnO}$  heterostructures.<sup>88,96</sup> When the temperature was decreased even further, the sheet carrier constant remained nearly constant over the temperature range of 100K to 13K. The room temperature mobility of  $\text{Be}_{0.02}\text{Mg}_y\text{ZnO}/\text{ZnO}$  heterostructures are in the order of  $200 \text{ cm}^2 / \text{Vs}$ . As we reduce the temperature the mobility of heterostructure monotonically increases and the highest mobility was obtained for sample A up

to  $1838 \text{ cm}^2 / \text{Vs}$  at 13 K, which is comparable to the values reported in MgZnO/ZnO heterostructures<sup>88,97</sup>. These characteristics of nearly temperature-independent sheet carrier density, increased mobility at room temperature over the ZnO value and the temperature dependence of mobility clearly indicate the presence of two dimensional electron gas at the interface of  $\text{Be}_{0.02}\text{Mg}_y\text{ZnO}/\text{ZnO}$  heterostructure.

Table V: Structure parameters and electronic properties of  $\text{Be}_{0.02}\text{Mg}_y\text{ZnO}/\text{ZnO}$  heterostructure for sample A, B and C

Sample	$\text{Be}_{0.02}\text{Mg}_y\text{ZnO}$		Sheet concentration		Electron Mobility	
	thickness (nm)	Mg content, y	$(10^{12} \text{ cm}^{-2})$		$(\text{cm}^2/\text{Vs})$	
			293 K	13K	293 K	13K
A	30	0.21	8	5.6	242	1838
B	30	0.26	9.3	7.0	249	1635
C	20	0.26	10.0	7.7	220	1509

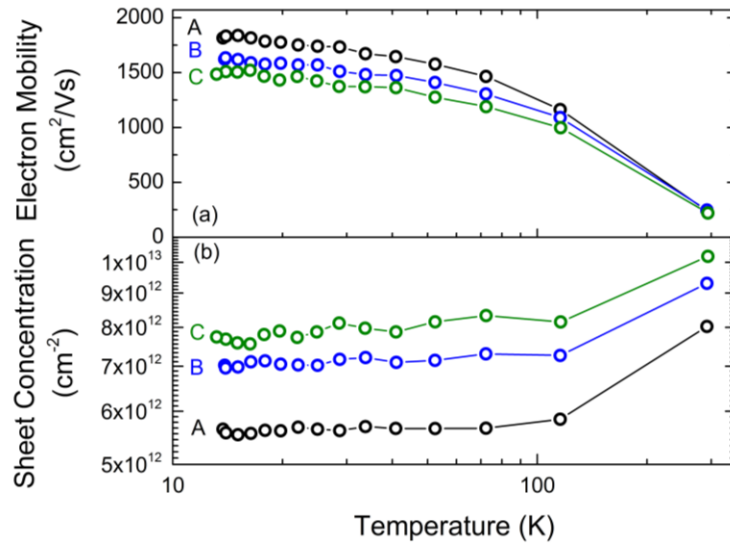


Figure 22: Hall-effect measurement of (a) electron mobility and (b) sheet concentration of two dimensional electron gas for  $\text{Be}_x\text{Mg}_y\text{ZnO}/\text{ZnO}$  samples shown in Table I over the temperature range from 13K to 293K.

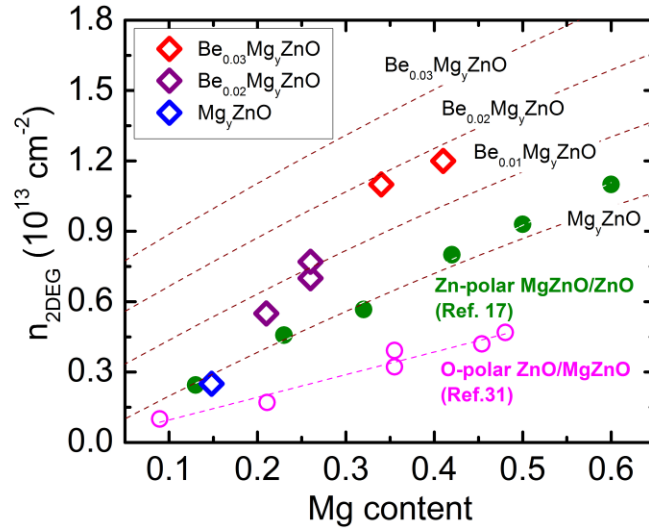


Figure 23: Comparison 2DEG sheet carrier density determined for Zn-polar  $\text{Be}_x\text{Mg}_y \text{Zn}_{1-x-y}\text{O}/\text{ZnO}$  with that in both Zn- (Tampo et al.<sup>88</sup>) and O polar  $\text{Mg}_y\text{Zn}_{1-y}\text{O}/\text{ZnO}$  heterostructures (Ullah et al<sup>98</sup>).

Figure 23 compares the 2 DEG sheet carrier concentrations as a function of Mg content in Zn-polar  $\text{Be}_x\text{Mg}_y\text{Zn}_{1-x-y}\text{O}/\text{ZnO}$  heterostructures with those in O-polar  $\text{ZnO}/\text{Mg}_y\text{Zn}_{1-y}\text{O}$  heterostructures grown in our lab (shown schematically in Figure 20 (a) and (d)) and Zn-polar  $\text{MgZnO}/\text{ZnO}$  HFET structure (Figure 20 (b)) reported by Tampo et al.<sup>88</sup>. Figure 23 also shows the polarization charge (dashed lines) computed theoretically for Be content varying for 0 to 3%. As seen from the Figure 23, the incorporation of only about 3% Be increases the 2DEG carrier density in Zn-polar  $\text{BeMgZnO}/\text{ZnO}$  heterostructures up to of  $1.2 \times 10^{13} \text{ cm}^{-2}$  containing 41% Mg in the barrier, whereas achieving the same carrier concentration in Zn-polar  $\text{MgZnO}/\text{ZnO}$  heterostructure would require the incorporation of 60% Mg into the barrier. The 2DEG concentration of  $7.7 \times 10^{12} \text{ cm}^{-2}$  obtained for the  $\text{BeMgZnO}/\text{ZnO}$  heterostructure containing 2% Be and 26% Mg in the barrier, would have required incorporation of more than 40% Mg into the

barrier in the MgZnO/ZnO heterostructure. Therefore, the incorporation of only about 2-3% Be into the barrier layer significantly increases the 2DEG density through strain engineering as discussed earlier. The observed increase in 2DEG sheet carrier concentration in heterostructures with quaternary barriers agrees well with the trend observed in the theoretical calculation, although it overestimates the sheet carrier densities. The discrepancy between calculated polarization sheet charge densities at the BeMgZnO/ZnO interface and the experimental 2DEG concentrations most likely arise from uncertainties in elastic constants and polarization parameters used, as well as errors in determining the composition (particularly, accurate determination of low concentrations of Be is challenging) and partial strain relaxation in the barrier. Also higher carrier density observed in Zn polar Mg<sub>y</sub>Zn<sub>1-y</sub>O / ZnO<sup>88</sup> compared to O-polar ZnO / Mg<sub>y</sub>Zn<sub>1-y</sub>O heterostructures, an aberration from the ideal theoretical calculation, can be explained by the advantage of Zn polar HFET structure over the O polar one. In O-polar ZnO / MgZnO structure, the thin ZnO channel grown on MgZnO buffer may have degraded quality compared to the established growth technique of epitaxial ZnO on sapphire or GaN. Therefore, electron trap generated by defect may reduce the 2DEG sheet carrier density of O-polar ZnO / Mg<sub>y</sub>Zn<sub>1-y</sub>O heterostructure.



## Chapter 5. Electrical characterization of BeMgZnO/ZnO heterostructure

### 5.1 Schottky diode on BeMgZnO:

Considerable efforts were made by some researchers to elucidate possible current transport mechanisms associated with forward-bias current in ZnO Schottky contact device.<sup>99,100</sup> The chemical reactions between the metal and the semiconductor, the surface states, the contaminants, the defects in the surface layer, and the diffusion of the metal into the semiconductor are well known problems in the formation of Schottky contacts. Strong downward surface band bending<sup>101</sup> is observed for ZnO surface which results in increased carrier concentration near the surface by orders of magnitude from the bulk carrier concentration.<sup>102</sup>

There are variety of methods reported in the literature that are used to prepare the surface of ZnO for better Schottky contact fabrication, such as HCl etching (and other acids), Ar physical etching, H<sub>2</sub>O<sub>2</sub> treatment<sup>103-105</sup>, UV Ozone and O-plasma (or mixture with He) exposure. H<sub>2</sub>O<sub>2</sub> treatment shows improved performance in comparison to HCl or H<sub>3</sub>PO<sub>4</sub> etching prior metal deposition (0.7eV for H<sub>2</sub>O<sub>2</sub> and Ohmic for HCl).<sup>106</sup> In fact, the peroxide may additionally eliminate oxygen vacancies that serve as donors on the surface of ZnO. The reported H<sub>2</sub>O<sub>2</sub> surface treatments<sup>107</sup> usually include boiling in the non-diluted peroxide. Such procedure will etch thin films with thickness in the range of microns and therefore, cannot be applied for heterostructure FET. UV

Ozone and O-plasma are used only to decrease surface conductivity and do not etch ZnO. There are few works showing results for plasma treated samples vs. not plasma treated samples.

To create Schottky barrier with undoped ZnO, a high work function can be applied to the surface of a ZnO crystal. Although many publications<sup>108</sup> show that Au has some serious problems at high temperatures (>340 K), it has widely been applied to ZnO to form Schottky barriers<sup>108–113</sup>. Other metals used for the same purpose are Ag<sup>111–116</sup>, Pd<sup>113,117</sup>, and Pt<sup>118–121</sup>.

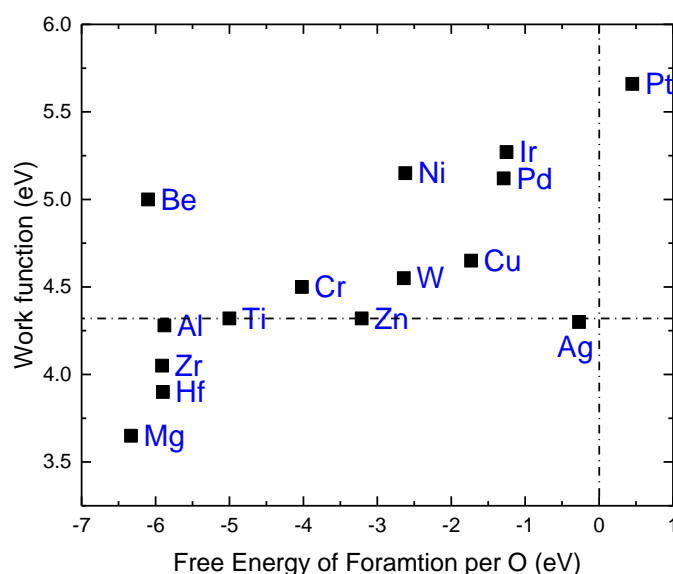


Figure 24: Free energy of formation per Oxygen atom for variety of metals as a function of metal work function

Usually Schottky contacts are achieved by depositing a high work function metal such as Pd, Pt, Ir etc (see Figure 24). In contrast, Ag has low work function of 4.26 eV. Despite that, devices fabricated with Ag metal can show rectifying behavior. This is due to interface silver oxide layer that is formed from partial oxidation of Ag with oxygen from ZnO matrix. The formed oxide layer is transparent for electrons and have higher work function in comparison to Ag. Raju et al.<sup>122</sup> reported ~5.55eV work function for PLD grown AgO which is 1.3 eV higher than of Ag

(4.26 eV). Silver oxidation with oxygen from ZnO must create high concentration of oxygen vacancies and therefore donors on the interface. It may be the case that there is a competition between the increase in number of oxygen vacancies (expected to hurt the Schottky performance) and the formation of silver oxide with higher work function than Ag (expected to benefit the Schottky performance) and overall the latter one wins. This consideration requires more detailed investigation. In spite of the fact that high-quality Schottky contacts are critical for ZnO device applications, there is little information about the Schottky contacts on BeMgZnO to date.

In order to get better understanding of the underlying mechanism of Ag / BeMgZnO Schottky diode, temperature dependent measurement is necessary. Richardson constant, Schottky barrier height inhomogeneity, conduction mechanisms, activation energy can be determined through temperature dependent I-V measurement. The temperature-dependent current-voltage (I-V-T) characteristics based on thermionic emission usually reveal a larger barrier height with increased temperature. Barrier height inhomogeneity is supposed to be responsible for this behavior. The Gaussian distribution of the barrier height is used to account for the inhomogeneity at the interface arising due to potential fluctuations in Schottky contact devices. Muller et al.<sup>123</sup> reported temperature-dependent I-V characteristics of the sputtered PdO<sub>x</sub>/ZnO Schottky diodes. The derived standard deviation of the barrier height inhomogeneity is  $\sigma=0.2$  eV and the mean barrier height is  $\phi_b^m = 1.37$  eV for PdO<sub>x</sub>/ZnO Schottky contact. A major breakthrough in the development of Schottky contacts (SCs) on untreated ZnO surfaces with remarkably low ideality factors and large effective barrier heights was achieved by Allen et al. in 2007. They reported reactively sputtered AgO<sub>x</sub>/SCs on ZnO bulk single crystals with ideality factors close to unity (1.1).<sup>124</sup> Using such SCs with nearly homogeneous barriers, it was for the first time possible to

extract an experimental value of the effective Richardson constant of ZnO of  $10 \text{ Acm}^{-2}\text{K}^{-2}$  from temperature dependent current-voltage (I-V) measurements<sup>99</sup>. The reported values for the effective Richardson constant are in the vicinity of the theoretical value of  $32 \text{ Acm}^{-2}\text{K}^{-2}$  for ZnO. Sarpatwari et al. reported  $27 \pm 7 \text{ Acm}^{-2}\text{K}^{-2}$  for nearly ideal Schottky diode with  $\text{IrO}_x$ . Kim et al.<sup>125</sup> reported  $49.0 \text{ Acm}^{-2}\text{K}^{-2}$ . The value of  $10 \pm 6 \text{ Acm}^{-2}\text{K}^{-2}$  was reported by Allen et. al,<sup>126</sup> with confirmation that thermionic emission model with barrier lowering due to image force lowering is the dominant transport mechanism for the fabricated SCs. Muller et al.<sup>123</sup> extracted the effective Richardson constant of  $7.7 \pm 4.8 \text{ Acm}^{-2}\text{K}^{-2}$ . However, to the best of this author knowledge, no temperature dependent I-V results from BeMgZnO Schottky diode have been reported so far.

In this work, we have achieved silver Schottky diode on BeMgZnO/ZnO heterostructure with remote oxygen plasma surface treatment. We have extended our analysis to include studies of current voltage characteristics in BeMgZnO/ZnO heterostructure measured at various temperatures in the range of 85-470 K. the temperature dependence of ideality factor and the barrier height is systematically investigated using thermionic emission theory on the basis of the Gaussian distribution of the barrier heights around the mean value due to barrier height inhomogeneity at the interface.

### **5.1.1 Fabrication of Ag/Be<sub>0.02</sub>Mg<sub>0.26</sub>ZnO Schottky diode:**

We explored Ag Schottky contacts on quaternary Zn polar BeMgZnO/ZnO heterostructure grown by P-MBE on GaN/sapphire template previously deposited by MOCVD technique. Zn polarity was maintained by using high VI/II ration during the nucleation growth of ZnO at  $300^\circ \text{C}$  on GaN. The thickness of the BeMgZnO was 30 nm and a presence of two dimensional has been confirmed on BeMgZnO/ ZnO heterostructure. To obtain Ohmic contact, 30 nm of Ti was

deposited by e-beam evaporation followed by a 50 nm Au deposition by thermal evaporation technique. The specific contact resistivity of Ohmic contact was found about  $2.25 \times 10^{-5} \Omega \text{ cm}^2$ . Before proceeding to Ag Schottky metal deposition by e-beam technique the BeMgZnO surface has been treated with remote oxygen plasma for 5 min with a 50 W RF power and 35 sccm oxygen flow. 50 nm of Ag metal was deposited as Schottky contact on rectangular ( $140 \mu\text{m} \times 80 \mu\text{m}$ ) and circular pad of two different diameters (140  $\mu\text{m}$  and 1 mm).

Schottky diodes were fabricated on four different BeMgZnO/ZnO heterostructures whose electron mobilities, sheet carrier concentrations, ideality factors and barrier heights at room temperature are given in Table VI

Table VI:  $\text{Be}_x\text{Mg}_y\text{Zn}_{1-x-y}\text{O}/\text{ZnO}$  samples studied for Ag Schottky diode with their electron mobility, 2 DEG sheet carrier concentration, Schottky contact area, barrier height and ideality factor at room temperature

Sample no	77 K Mobility $\text{cm}^2/\text{Vs}$	2 DEG Sheet carrier concentration $\text{cm}^{-2}$	Schottky area $\text{cm}^2$	Barrier height eV	Ideality factor
A/1067	225	$2 \times 10^{12}$	$1.54 \times 10^{-4}$ (circular)	0.93	1.81
B/1071	350	$5.5 \times 10^{12}$	$3.85 \times 10^{-4}$ (circular)	0.80	1.73
C/1226	750	$6.7 \times 10^{12}$	$7.85 \times 10^{-4}$ (circular)	0.67	2.3
D/1207	1553	$6.2 \times 10^{12}$	$1.12 \times 10^{-4}$ (rectangular)	1.07	1.22

Figure 25 shows the current-voltage (I-V) characteristics at room temperature of the BeMgZnO/ZnO HEMT based Schottky diodes shown in Table VI. The forward bias current increases exponentially with the applied-bias voltage in the intermediate voltage regime ( $0.1\text{V} \leq V \leq 1\text{V}$ ). Beyond 1 V a small increase in current is observed with the increase in forward voltage which is attributed mainly to the significant effect of the series resistance in I-V characteristics. A slight increase of the current is visible in reverse bias direction. This is explained by the voltage-dependent image force lowering effect which reduces the apparent barrier height<sup>123</sup>.

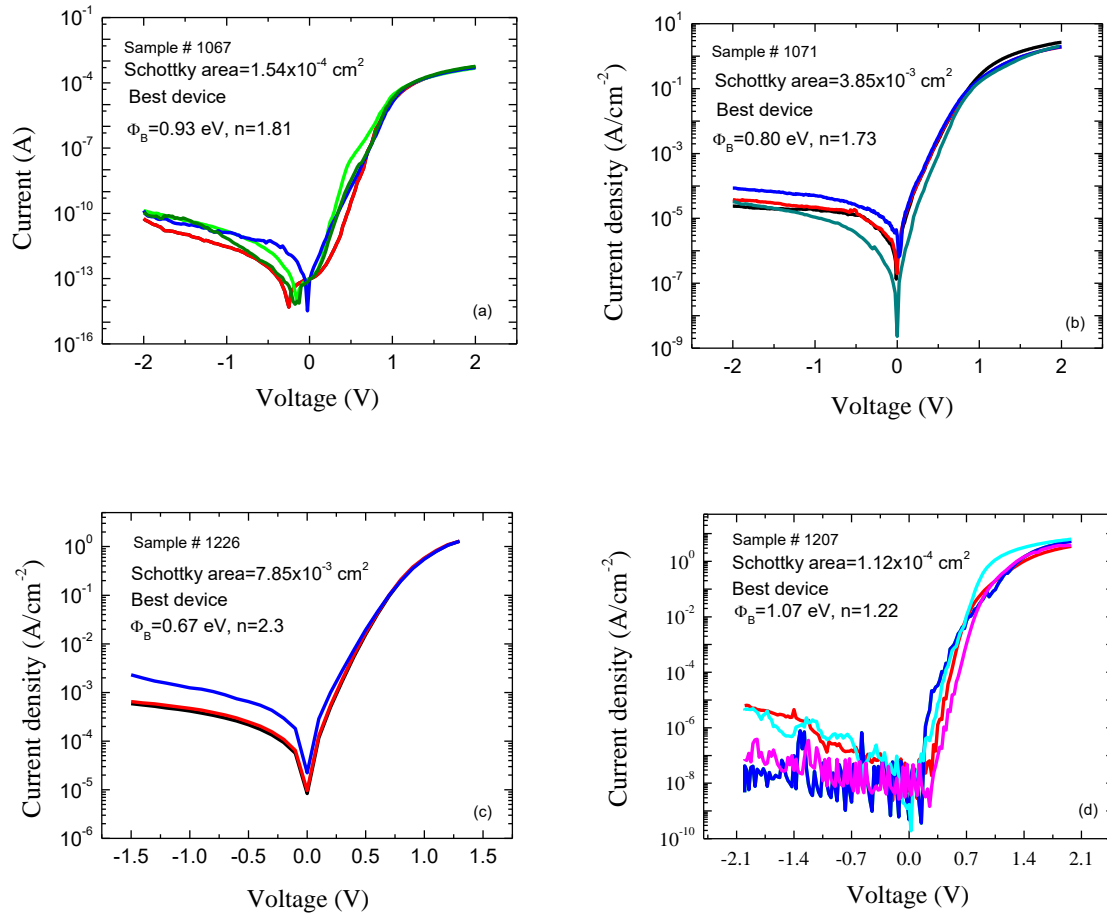


Figure 25: I-V relationship of Ag Schottky diodes on  $\text{Be}_x\text{Mg}_y\text{Zn}_{1-x-y}\text{O}/\text{ZnO}$  samples

We have analyzed the experimental (I-V) curves according to the thermionic emission theory (TE) at forward bias voltage V ( $V \geq 3kT/q$ ), in which the current-voltage characteristics can be expressed as:

$$I = I_0 \exp\left[\frac{q(V - IR_s)}{nkT}\right] \quad 14$$

where n is the ideality factor, k Boltzmann's constant, T the absolute temperature and  $R_s$  the series resistance of the diode. The saturation current  $I_0$  of the diode is given by

$$I_0 = AA^*T^2 \exp\left(\frac{-q\Phi_B}{kT}\right) \quad 15$$

where A is the Schottky contact area,  $\Phi_B$  the barrier height,  $A^*$  the effective Richardson constant defined as

$$A^* = \frac{4\pi qm^*k^2}{h^3} \quad 16$$

where h is Plank's constant,  $m^*$  is the effective electron mass. Richardson constant value is calculated for  $\text{Be}_{0.02}\text{Mg}_{0.26}\text{ZnO}$  by assuming linear approximation of theoretically calculated Richardson constant of BeO, MgO and ZnO by using the effective mass of the binary constituent listed in Table VII. The barrier height and ideality factor for each diode were obtained using the calculated Richardson constant of  $36 \text{ Acm}^{-2}\text{K}^{-2}$  while fitting the forward I-V curve over the range  $0.1\text{V} < V < 0.3 \text{ V}$  using Eqs. (1) and (2) assuming zero series resistance at this range of potential applied.

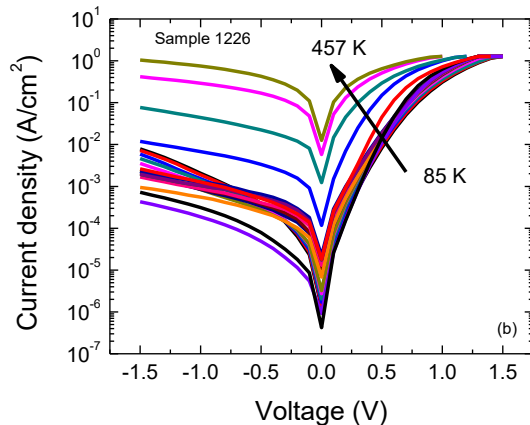
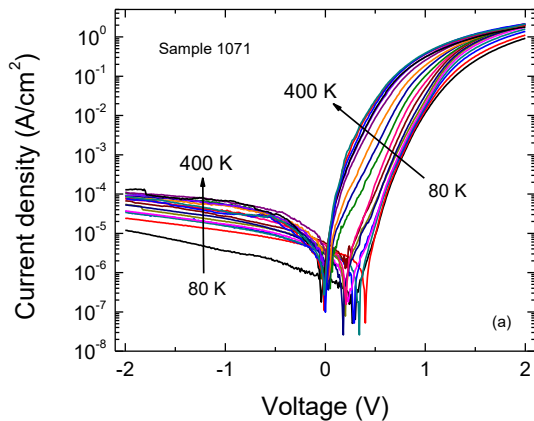
Table VII: Effective mass of II-oxides semiconductor and calculated Richardson constant using Eqn 3

	BeO	MgO	ZnO
Effective mass, $m^*$	0.58 <sup>90</sup>	0.37 <sup>127</sup>	0.27 <sup>128</sup>
Richardson constant, $A^*$	32.3	69.4	44.2

Ideality factor and apparent barrier height obtained through exponential fitting are listed in Table VI. The highest schottky barrier height  $\Phi_B = 1.07$  eV was obtained from sample D at room temperature with an ideality factor 1.22. As can be seen from Figure 25 (d) that rectification ratio as high as 8 orders of magnitude has been obtained. It has been observed consistently that the device performances were improved in the smaller Schottky junction due to less amount leakage current more homogeneous barrier.

### 5.1.2 Temperature dependent properties of BeMgZnO Schottky Diodes:

We have carried out temperature dependent I-V measurement on the Schottky diode of larger contact area. Measurements were performed at a pressure of  $10^{-6}$  Torr to avoid water vapor condensation, with the diode mounted in a cold head equipped with a LN<sub>2</sub> cooling system. A LakeShore 330 temperature controller (accuracy  $\pm 0.1$  K) and an HP 4140B DC voltage source capable to measure pA current was employed for data acquisition. Figure 26 shows the I-V curves for sample B, C and D measured at different temperature. For all samples, the forward current shows exponential behavior for orders of magnitude indicating the dominance of TE. Current at forward biases, for all samples, increases with increasing temperature as expected for TE<sup>123,126</sup>. Current at reverse bias, increases for sample B with increasing temperature while for sample C it decreases at the lower range of the temperature explored.





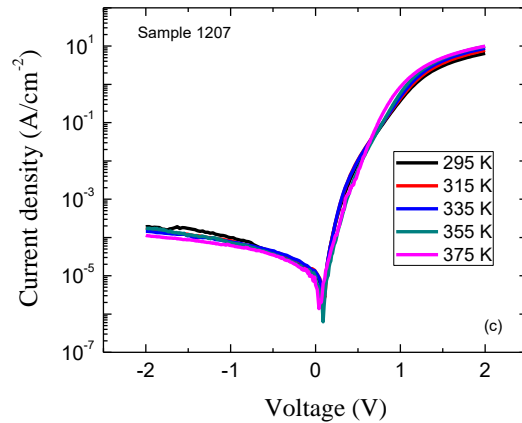
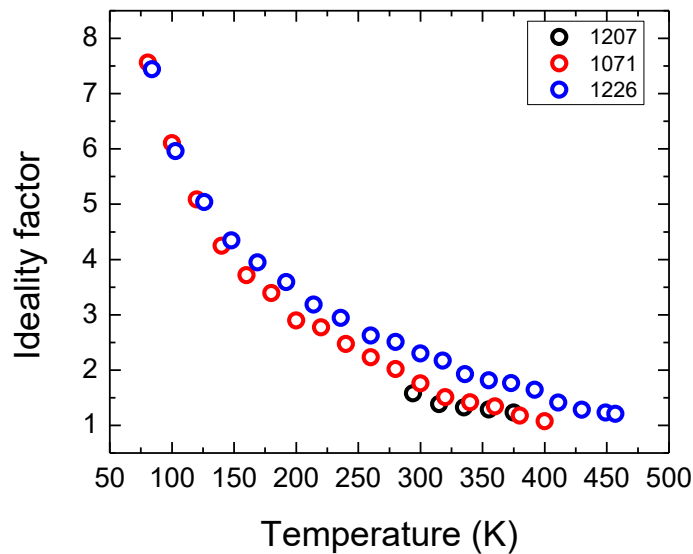


Figure 26: Temperature dependent current-voltage (I-V) measurement of Ag/Be<sub>0.02</sub>Mg<sub>0.26</sub>MgO Schottky diode at temperature range from (a) 80 K to 400K for sample B (b) 85 K to 457 K. for sample C and (c) 300 K-375 K for sample D.

The ideality factor  $n$  and apparent barrier height  $\Phi_B$  are determined from the slope and intercept of the linear region of the forward bias I-V. The ideality factor is introduced to take into account the deviation of the experimental I-V from the ideal thermionic emission theory. The variations of the ideality factor  $n$  and barrier height  $\Phi_B$  as a function of temperature are shown in Figure 27



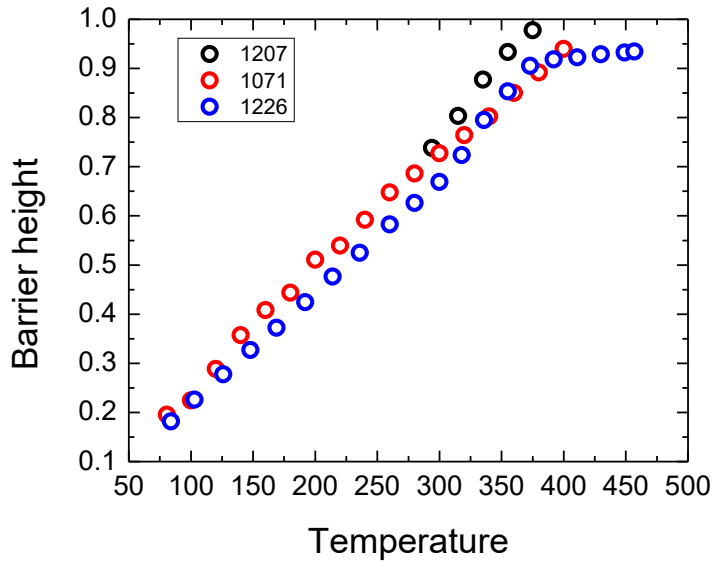


Figure 27: Temperature dependence of the (a) ideality factor and (b) barrier height for the Ag/BeMgZnO/ZnO Schottky diode.

It is noteworthy that the ideality factor and barrier height are highly dependent on temperature, that is,  $n$  decreases and  $\Phi_B$  increases with increasing temperature. As seen from Figure 27 (a), the experimental values of  $n$  strongly decrease with increasing temperature from 7.56 at 80 K, to 1.07 at 400 K for sample B, from 7.44 at 85 K to 1.20 at 457 K for sample C and 1.58 K at 295 K to 1.23 at 375 K. The barrier height also shows a strong dependence on the temperature (Figure 27 (b)). We have observe an increase of the apparent barrier with increasing temperature, where the slope increases gradually except for sample C where it becomes linearly dependent on the inverse temperature for temperatures above 360 K. The similar dependence of ideality factor and barrier height has been reported by Muller et al.<sup>123</sup> Barrier height increases from 0.20 eV at 80 K to 0.94 eV at 400 K for sample B, from 0.18 eV at 85 K to 0.93 eV at 457 K for sample C and for sample D it increases from 0.74 eV at 300 K to 0.98 eV at 375 K temperature. We have used the temperature range above room temperature for the study of lateral inhomogeneity of the

mean barrier height and standard deviation. The use of this higher temperature region also has the advantage that the current transport is well described by TE and other possible transport mechanisms such as tunneling or trap-assisted tunneling can be safely ignored<sup>129</sup>.

The high value of  $n$  at low temperature is often attributed to the existence of interface states localized at the interface and to barrier inhomogeneities.<sup>130,131</sup> This behavior can be associated with the presence of a nonuniform Schottky contact.<sup>132</sup> Such nonuniformity can be attributed to Thermionic Field Emission (TFE) and the lateral inhomogeneities of the barrier height.<sup>130,133</sup> Moreover, it is well known that the current transport mechanism across the interface is a temperature-activated process. At low temperature, the carriers are only able to overcome the lower barrier heights and tunneling through the barrier becomes dominant, whereas, with the increase in temperature, more carriers have sufficient energy to surmount the higher barriers. As a result, the apparent energy barrier height will increase with the temperature. Here we have used a model assuming a Gaussian distribution of the barrier heights as proposed by Sachs<sup>134</sup>

$$P(\bar{\Phi}_B(V_A)) = \frac{1}{\sigma(V_A)\sqrt{2\pi}} \times \exp\left(-\frac{(\bar{\Phi}_B(V_A) - \Phi_B)^2}{2\sigma^2(V_A)}\right) \quad 17$$

Here, both the mean barrier height and the standard deviation have a linear voltage dependence

$$\sigma^2(V_A) = \sigma^2(0) + \rho_3 V_A \quad 18$$

$$\bar{\Phi}_B(V_A) = \bar{\Phi}_B(0) + \rho_2 V_A \quad 19$$

where  $\rho_2$  and  $\rho_3$  are assumed to be temperature independent. The temperature dependence of the ideality factor is expressed as

$$n = \frac{1}{1 - \rho_2 + (e\rho_3 / 2k_B T)} \quad 20$$

and the barrier height is given by

$$\Phi_B = \bar{\Phi}_B - \frac{q\sigma^2}{2k_B T} \quad 21$$

Equation 21 is commonly used in literature to determine the effective barrier height  $\bar{\Phi}_B$  from apparent barrier height  $\Phi_B$  measured from  $I$ - $V$  data. In order to prove the Gaussian distribution of barrier height, the plot of  $\Phi_B$  versus  $q/2kT$  should give a straight line, the intercept of which is the effective barrier height and the slope is the variance ( $\sigma^2$ ). The standard deviation is a measure of the barrier homogeneity, i.e. the lower value of  $\sigma^2$  corresponds to a more homogeneous barrier height.

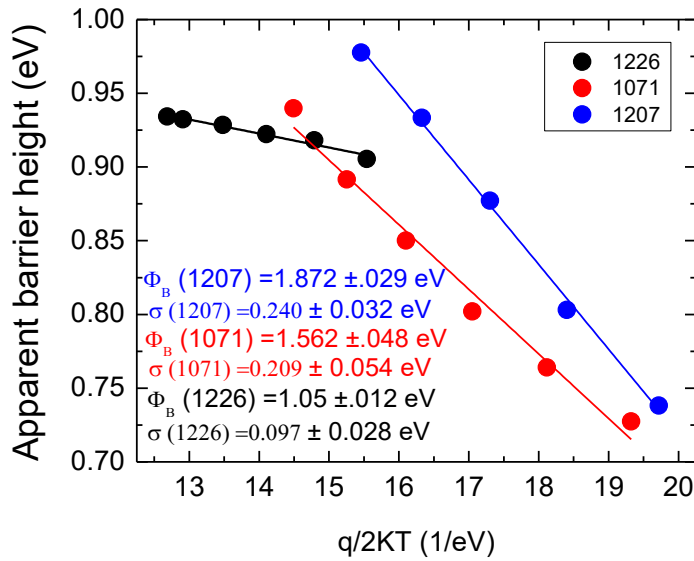


Figure 28: Barrier height versus  $q/2kT$  plot for Ag/Be<sub>0.02</sub>Mg<sub>0.26</sub>ZnO/ZnO heterostructure. Mean barrier height and standard deviation were found from the intercept and slope of the straight line.

Figure 28 is obtained by plotting the apparent barrier height as a function of  $q/2kT$ . The linear dependence of the barrier height with the inverse temperature denotes that the Ag/BeMgZnO/ZnO Schottky diodes indeed show lateral inhomogeneity of barrier height that follows Gaussian distribution. The extrapolation of the straight line at  $T^{-1} \rightarrow 0$  gives the effective barrier height ( $\bar{\Phi}_B$ )  $1.562 \pm 0.48$  eV,  $1.03 \pm 0.005$  eV and  $1.872 \pm 0.029$  eV with standard deviation  $0.209 \pm 0.054$ ,  $0.097 \pm 0.028$ ,  $0.240 \pm 0.032$  from sample B, C and D respectively.

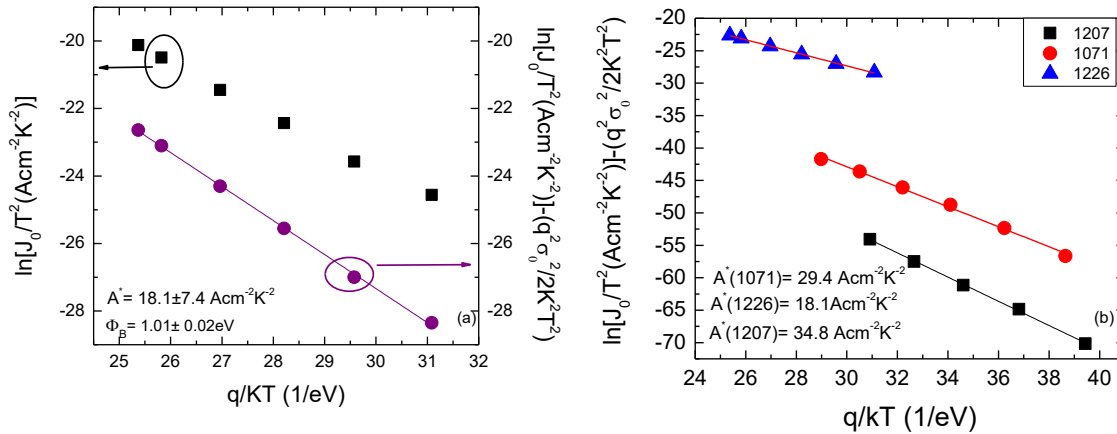


Figure 29: Richardson plot (square) of  $\ln\left(\frac{J_0}{T^2}\right)$  vs  $q/kT$  and a modified Richardson plot (circle) of  $\ln\left(\frac{J_0}{T^2}\right) - \frac{q^2\sigma^2}{2k^2T^2}$  vs  $q/kT$  together with a linear fit to determine

Equation 15 is used to construct a Richardson plot of  $\ln(I_0/T^2)$  versus  $q/kT$ , with the slope giving  $\Phi_B$  and  $A^*$  determined by the intercept. This plot is shown in Figure 29 (a) (filled square), but the temperature dependence of  $\Phi_B$  makes fitting a single slope problematic. As it is mentioned earlier, Schottky diodes usually show ideal behavior at room temperature and above, therefore we can safely ignore other current conduction mechanism except thermionic emission. Therefore, the Richardson plot is constructed using the I-V results at higher end of the temperature investigated for Ag/Be<sub>0.02</sub>Mg<sub>0.26</sub>ZnO/ ZnO Schottky diode. As can be clearly seen in the Figure 29 (a), the temperature dependence of  $\ln(J_0/T^2)$  versus  $q/kT$  plot is found to be linear. By means of fitting the experimental data, from the intercept and the slope of the straight line, the values of Richardson constant  $A^*$  and effective barrier height  $\bar{\Phi}_B$  were extracted from sample C as  $0.82 \text{ Acm}^{-2}\text{K}^{-2}$  and  $0.883 \text{ eV}$ . It is worthy to notice that the values of the conventional Richardson constant  $A^*$  are noticeably different from the theoretical value of Be<sub>0.02</sub>Mg<sub>0.26</sub>MgO ( $36 \text{ Acm}^{-2}\text{K}^{-2}$ ). The deviation from the ideal values can be ascribed to the different interface quality, which, in turn, depends on several factors such as the surface defects density resulting

from growth, surface treatment (cleaning, etching, etc.), metal deposition process (evaporation, sputtering, etc) and obviously the lateral inhomogeneity of effective barrier height. In this work, we have modified the conventional Richardson plot according to the Gaussian distribution of the barrier height by replacing the effective barrier height,  $\Phi_B$  in equation 15 by the equation 21

$$\ln\left(\frac{I_0}{AT^2}\right) - \frac{q^2\sigma^2}{2k^2T^2} = \ln(A^*) - \frac{q\bar{\Phi}_B}{kT} \quad 22$$

Filled circle in Figure 29 shows the modified Richardson plot  $\ln\left(\frac{I_0}{AT^2}\right) - \frac{q^2\sigma^2}{2k^2T^2}$  versus  $q/kT$ .

From the intercept and the slope of the straight line, the values of Richardson constant  $A^*$  and effective barrier height were extracted as  $18.1 \pm 7.4 \text{ Acm}^{-2}\text{K}^{-2}$  and  $1.01 \pm 0.02 \text{ eV}$ . The value of effective barrier height ( $\bar{\Phi}_B$ ) obtained from the modified Richardson plot are similar to that obtained from apparent barrier height,  $\Phi_B$  versus  $q/2kT$  plot in Figure 28 (a). Richardson constant value of  $29.4 \text{ Acm}^{-2}\text{K}^{-2}$  and  $34.8 \text{ Acm}^{-2}\text{K}^{-2}$  obtained from sample B and D (Figure 28 (b)), respectively, are close enough to the value calculated theoretically for  $\text{Be}_{0.02}\text{Mg}_{0.26}\text{ZnO}$  quaternary alloy.

The high ideality factor at low temperature, observed from Figure 27 (a), indicates an obvious deviation from pure thermionic emission which can be explained by thermionic field emission model. If the current transport is controlled by the thermionic field emission theory, the relationship between the current and voltage can be expressed

$$J_F = J_{SF} \exp\left(\frac{qV}{n_{tun}kT}\right) \quad 23$$

with

$$n_{tun} = \frac{E_{00}}{kT} \coth\left(\frac{E_{00}}{kT}\right) = \frac{E_0}{kT} \quad 24$$

and

$$J_{SF} = \frac{A^*T^2 q \sqrt{\pi E_{00}(\Phi_B - V + V_n)}}{kT \cosh(E_{00}/kT)} \left( \frac{qV_n}{kT} - \frac{q(\Phi_B + V_n)}{E_0} \right) \quad 25$$

where

$$V_n = \frac{kT}{q} \ln \frac{N_C}{N_D} \quad 26$$

where  $E_{00}$  is the characteristic tunneling energy that is related to the tunnel effect transmission probability:

$$E_{00} = \frac{h}{4\pi} \left( \frac{N_d}{m^* \epsilon_s} \right)^{1/2} \quad 27$$

Where  $\epsilon_s = 8.5 \epsilon_0$   $m^* = 0.27 m_0$  for  $\text{ZnO}^{90}$  and  $h = 6.626 \times 10^{-34} \text{Js}$ . The ideality factor shown in Figure 27 (a) for sample B are plotted in Figure 30 together with calculated theoretical curves. As seen in Figure 30, the measured values agree very well with theoretical curves, giving  $E_{00} = 45 \sim 50 \text{ meV}$ . Thus, this analysis strongly suggests that the TFE mechanism is somehow involved in the present BeMgZnO Schottky contacts.

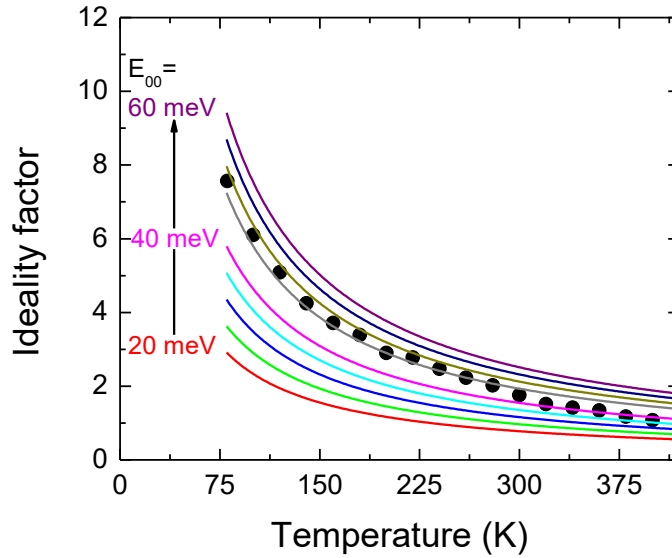


Figure 30: Calculated temperature dependence of the ideality factor for the case when the current through the junctions is dominated by the TFE with characteristic energy values  $E_{00}$  according to equation 24 (solid lines) for the Ag/BeMgZnO studied. The filled circles show the experimental temperature dependence values of the ideality factor obtained from  $I-V$  characteristics given in Figure 27(a).

According to equation 27,  $E_{00} = 45 \sim 50 \text{ meV}$  correspond to donor concentrations of  $N_D = 1.2 - 1.5 \times 10^{19} \text{ cm}^{-3}$ . Assuming a 4 nm 2DEG channel, the corresponding sheet carrier density would be

$4.8\text{-}6 \times 10^{12} \text{ cm}^{-2}$ . The 2DEG sheet carrier density for sample B measured from Hall-effect measurement is within the range of values calculated from  $E_{00}$  parameter.

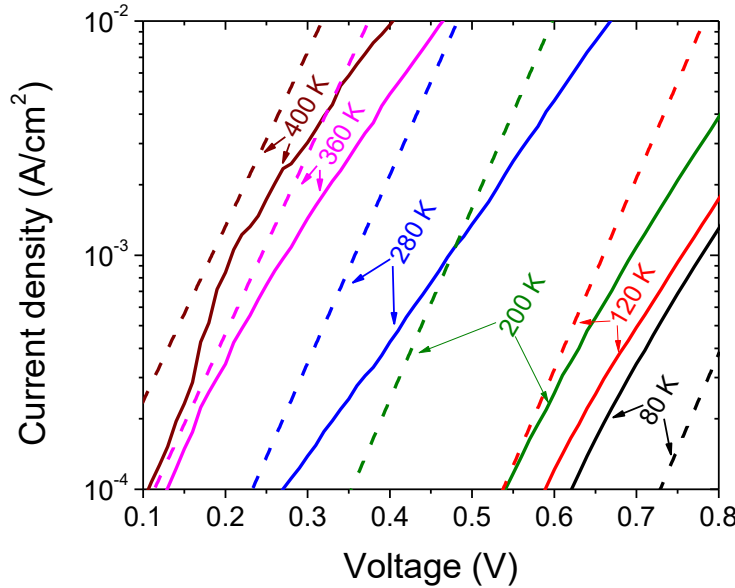


Figure 31: Calculated I-V-T curves using the TFE/FE model (dashed line) for  $E_{00} = 50 \text{ meV}$  obtained from Figure 30. Solid line shows the experimentally found I-V-T curves.

Using equation 23 to 25, we have plotted the calculated I-V curves at temperatures ranging from 80 K to 400 K (Figure 31 dashed lines) using  $E_{00} = 50 \text{ meV}$  obtained from Figure 30 and effective barrier height 1.55 eV obtained from Gaussian distribution of inhomogeneous barrier height. The theoretically calculated I-V curves matched sufficiently well with the experimentally measured I-V curves (solid lines).

The ideality factor and the barrier height measured at different temperatures can be modelled by means of Gaussian distribution of the barrier height. It has been shown that these parameters and their functions can also be explained by the dominant TFE mechanism. However, one cannot distinguish between the two possible models on the basis of the I-V characteristics only, that is, the domination of TFE can be connected with the lateral distribution of barrier height. Since the



enhancement of the transmission probability can also yield a local reduction of the barrier height. In our case, we suggest that the dominance of TFE may be connected to the Gaussian distribution of the barrier height.

## 5.2 Capacitance-voltage (CV) measurement and carrier confinement of two dimensional electron gas:

The presence of two dimensional electron gas can be understood from capacitance-voltage (C-V) profiling technique<sup>135</sup> using a multifrequency inductance, capacitance, resistivity (LCR) meter operated at room temperature between 500 kHz to 2 MHz. The C-V profiling technique allows one to measure the carrier concentration

$$N_{C-V} = \frac{C^3}{e\epsilon_0\epsilon} \frac{dV}{dC}$$

as a function of depth

$$z_{C-V} = \frac{\epsilon_0\epsilon}{C}$$

where V is the voltage applied to the Schottky contact, C is the measured differential capacitance per unit area,  $\epsilon$  is the dielectric constant of the material ( $\epsilon_0 = 8.85 \times 10^{-14}$  C/V cm;  $e = 1.602 \times 10^{-19}$  C). Differential capacitance is extracted from the differential impedance measured from LCR meter by using serial and/or parallel RC circuit model where the inductance is assumed to be negligible. More complex model consisting of several capacitance and resistance can be used as in the case of transistor to measure unknown capacitance and resistance with greater accuracy. Using the serial model, where a resistance and a capacitance is connected in series, the differential capacitance can be found using the equation

$$C = \frac{-1}{2Y\pi f}$$

whereas in parallel model, where a capacitance and a resistance is connected in parallel, the capacitance can be found using the equation

$$C = \frac{-1}{2} \frac{Y}{f\pi(X^2 + Y^2)}$$

where X and Y are the real and imaginary part of the impedance, Z, obtained from the LCR meter.

Ideally, for a noncompensated homogeneously doped semiconductor, the C-V concentration  $N_{C-V}$  should be equal to the free carrier concentration. However, in semiconductors and heterostructures, with large variation of the doping concentration (intentional or unintentional), and especially in structures with 2DEG confinement, the C-V concentration ( $N_{C-V}$ ) does not really convey the actual information of the carrier profile. Nevertheless, Kroemer et al<sup>136</sup> showed that charge conservation is fulfilled for C-V profiles, that is,

$$n_s = \int_{-\infty}^{\infty} N_{C-V}(z_{C-V}) dz_{C-V} = \int_{-\infty}^{\infty} n(z) dz$$

This property of the C-V technique is very useful for determination of the sheet carrier concentration  $n_s$  and the location of the 2DEG in HEMT heterostructure.

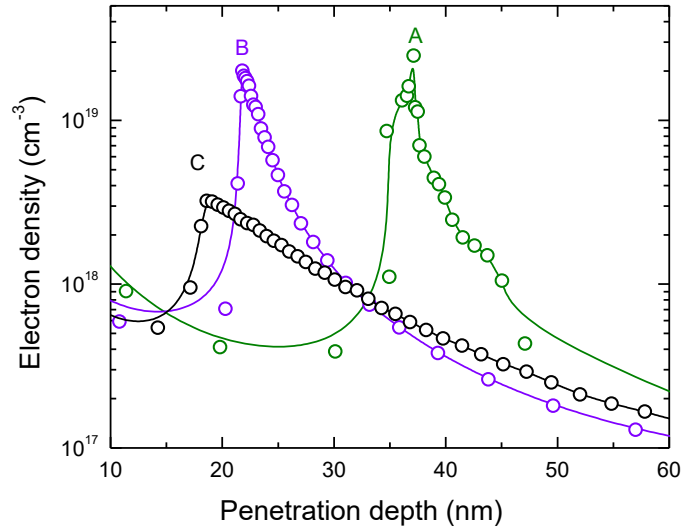


Figure 32: C-V concentration profile of  $N_{C-V}$  vs penetration depth of  $\text{Be}_x\text{Mg}_y\text{ZnO}/\text{ZnO}$  heterostructure shown in Table

Figure 32 shows electron density vs penetration depth profile of  $\text{Be}_x\text{Mg}_y\text{Zn}_{1-x-y}\text{O}/\text{ZnO}$  heterostructure samples obtained from C-V measurement. Growth condition of the samples are listed in

Table VIII. As seen from Figure 32, the depth of peak electron density confirms the confinement of two dimensional electron gas at the  $\text{BeMgZnO}$  and  $\text{ZnO}$  interface. The depth of the peak electron density correlates well with  $\text{BeMgZnO}$  thickness measured by  $\alpha$ -step profilometer. However, for all the three samples, the peak density occurred a little earlier which could be the effect of improper dielectric constant used for depth calculation and/or the error margin of

profilometer ( $\pm 10$  nm). ZnO relative dielectric constant ( $\epsilon_r = 8.5$ ) is used for depth calculation which could be different for BeMgZnO layer.

Table VIII: BeMgZnO thickness and sheet carrier concentration comparison between C-V profiling technique and Hall-effect measurement

Sample	BeMgZnO thickness nm	Sheet carrier concentration cm <sup>-2</sup>	
		Hall-effect measurement at 13 K	C-V profiling
		A	50
B	30	$7.1 \times 10^{12}$	$6.3 \times 10^{12}$
C	20	$7.7 \times 10^{12}$	$4.0 \times 10^{12}$

Sheet carrier concentrations calculated from C-V measurement are also compared with that obtained from Hall-effect measurement at 13K temperature. 2DEG sheet carrier concentration is obtained through integration around the peak electron concentration. Sheet carrier concentration obtained from C-V profiling technique shows a little lower trend in general except for sample C. In sample C, the difference of sheet concentration between C-V and Hall-effect measurement is higher, could be an effect of poor confinement of two dimensional electron gas.

### 5.3 Hot electron energy relaxation time:

The high-field electron transport is accompanied with intense LO-phonon emission by hot electrons, the emitted non-equilibrium LO phonons accumulate, and the associated phenomena are often referred to as hot-phonon effects. Essentially, very short LO-phonon lifetimes are desirable for fast electron energy relaxation and the best operation of the device.<sup>160</sup> Strong LO-phonon-plasmon coupling is the condition for the ultrafast decay of hot phonons and the associated ultrafast relaxation of the hot electron energy. Indeed, a hot electron loses a considerable amount of energy when an LO phonon is emitted, but the energy loss is compensated when an LO-phonon is reabsorbed. The reabsorption rate is controlled by the lifetime of hot-phonon decay into acoustic phonons and other vibrations. The plasmon-assisted ultrafast decay of hot noise, slowest degradation, and fastest operation of GaN-based transistors with two-dimensional electron phonons has been shown to pave the way for the lowest gas (2DEG) channels<sup>137</sup>.

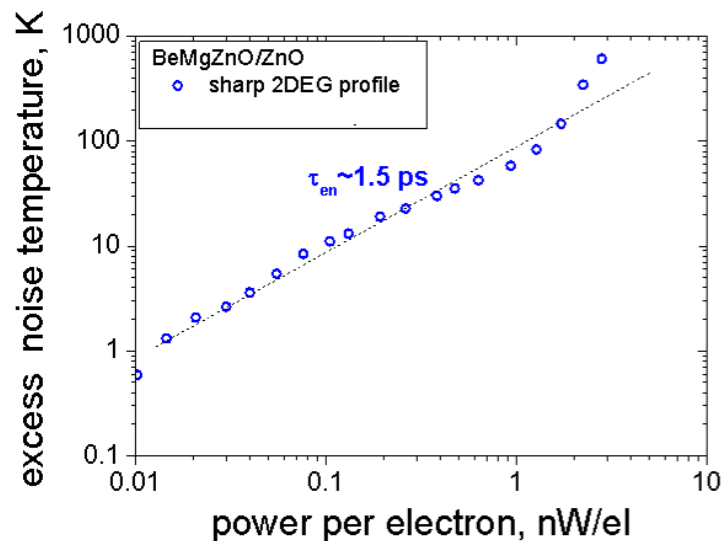


Figure 33: The dependence of excess noise temperature on power per electron for BeMgZnO/ZnO heterostructure with 2DEG

The electric power supplied to the electron gas  $P_s$  equals the dissipated power  $P_d$  because the voltage pulse is long enough for the strongly coupled subsystem of hot electrons and hot phonons to reach the quasi-steady state. The energy relaxation time approximation relates the electron gas temperature to the supplied power. The straight line in Figure 33 corresponds to the constant electron energy relaxation time. The self-heating effect is more easily avoided in 2DEG channels (100 ns pulses are short enough at the supplied power levels under discussion). The slope of the excess noise temperature versus the supplied power is used to obtain the energy relaxation time. The value of  $\tau_{en} = 1.5$  ps is extracted.

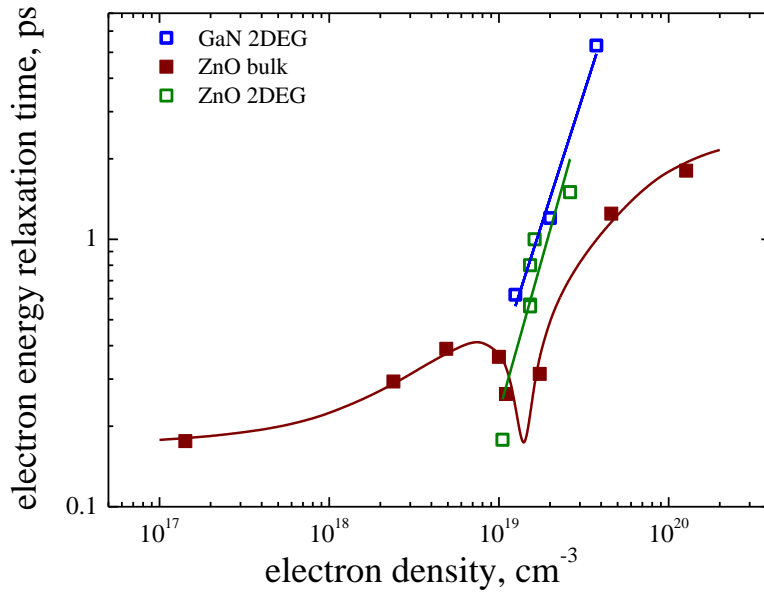


Figure 34: Electron energy relaxation time versus electron density per unit volume (blue symbol- GaN based 2DEG, green symbol-BeMgZnO/ZnO heterostructure with 2DEG, brown symbol-bulk ZnO)

We have studied the hot electron effects in the Be.Mg.ZnO/ZnO heterostructures with two-dimensional electron gas (2DEG) of different sheet carrier concentration. The results are compared with those for doped ZnO films and GaN based heterostructure with 2DEG. Figure 34 shows, in general, for a particular 2DEG sheet carrier density BeMgZnO/ZnO heterostructure

shows lower hot-electron energy relaxation time compared to AlGaIn/GaN heterostructure. The minimum energy relaxation 180 fs is obtained at  $4.2 \times 10^{12} \text{ cm}^{-2}$  two dimensional electron density. The similar sheet carrier density of GaN based heterostructure has 610 fs, a factor three higher hot-electron energy relaxation time. These findings bodes well with the theoretical prediction that ZnO based heterostructure should have shorter LO phonon life-time, due to lower LO phonon energy (70meV) compared to GaN (92meV). The value of sheet carrier density  $4.2 \times 10^{12} \text{ cm}^{-2}$ , in where the lowest hot-electron energy relaxation time is obtained, is in between the resonance density reported for GaN 2DEG channels ( $\sim 8 \times 10^{12} \text{ cm}^{-2}$ ) 2DEG channels and InGaAs 2DEG channels ( $\sim 2.5 \times 10^{12} \text{ cm}^{-2}$ )<sup>103</sup>. Therefore, this ultrafast energy relaxation indicates that LO phonon-plasmon resonance frequency for ZnO based heterostructure could be occurred near to  $4.2 \times 10^{12} \text{ cm}^{-2}$  electron sheet density. However, we do not know how sharp the resonance is. Further studies of hot-electron effects in ZnO-based channels are required on BeMgZnO/ZnO with lower 2DEG densities. To compare with the doped ZnO energy relaxation time, we have used an approach where the thickness of the channel is estimated as the width of the density profile at the Fermi level. Taking a realistic value of 4 nm, we get the average 3DEG density of  $\sim 1.05 \times 10^{19} \text{ cm}^{-3}$  for the 2DEG channel of sheet carrier density  $4.2 \times 10^{12} \text{ cm}^{-2}$ . The recent result correlates well with the doped ZnO films where the electron energy relaxation time was measured over a wide range of 3DEG densities. Although, the comparison is not straightforward because the 3DEG density is not constant in the 2DEG channel; it depends on the position in the transverse direction. The density profile resembles a rather asymmetrical Gauss function, and only some average 3DEG density can be specified for the 2DEG channel.

## Chapter 6. Conclusion

In this thesis growth of Zn polar BeMgZnO/ZnO heterostructure with two dimensional electron gas has been achieved by using molecular beam epitaxy technique. Two dimensional electron gas appeared at the BeMgZnO/ZnO heterointerface only when the Zn polarity was achieved during the nucleation growth of ZnO on GaN/sapphire template. We have demonstrated that the polarity of ZnO grown on Ga-polar (0001) GaN can be inverted from Zn-face to O-face, if the oxygen-to-Zn ratio is sufficiently high during the low temperature ZnO nucleation layer growth; even though the GaN surface is continually exposed to Zn flux before oxygen was allowed to the growth chamber. We propose that changes in stacking sequence caused by the formation of presumably one monolayer of non-stoichiometric GaO<sub>x</sub>, governed by the chemical and electronic factor at the GaN surface, may be responsible for the polarity inversion. We have also found that the VI/II ratio during LT-ZnO growth controls the sign and the extent of strain in ZnO films grown at high temperature of 670 °C on the LT nucleation layers. We further suggest that the density of Zn<sub>i</sub> varying with the VI/II ratio during nucleation growth is responsible for the change in residual strain.

We have demonstrated that when Mg and Be are co-incorporated into the wurtzite ZnO lattice the structural quality of wide-bandgap ZnO-based alloys improves due to compensation of strain, which also results in mutually enhanced incorporation of both species on cation lattice sites. This



unique feature allowed quaternary BeMgZnO alloys with bandgaps up to 5.1 eV. We have achieved growth of single crystal

We have achieved growth of single crystal O-polar  $\text{Be}_x\text{Mg}_y\text{Zn}_{1-x-y}\text{O}$  alloy at 500 °C on (0001) GaN/sapphire template. Our data revealed a thermodynamic limitation of Mg and Be incorporation in the wurtzite  $\text{Be}_x\text{Mg}_y\text{Zn}_{1-x-y}\text{O}$  lattice beyond which excess Mg and probably Be tend to initiate phase segregation. Moreover, an increase in the in-plane lattice parameter observed from evolution of RHEED pattern during quaternary growth suggests presence of a wurtzite MgO-rich layer on the growing surface. We propose that relative more negative formation enthalpy of MgO compared to ZnO and the increased surface mobility of Mg adatoms at high temperatures are responsible for the formation of MgO-rich phase. We have demonstrated that the use of sufficiently high Zn / (Be + Mg) ratio is required to suppress the second phase generation at elevated growth temperature.

In addition, our calculations indicate that the incorporation of Be in alloy barrier in ZnO-based heterostructures makes it possible to change the strain sign, and thus, align the direction of piezoelectric polarization in the same direction as spontaneous polarization vector. As a result, the piezoelectric polarization component adds up with the spontaneous polarization resulting in higher 2DEG sheet carrier density at the BeMgZnO/ZnO and ZnO/BeMgZnO interfaces in Zn-polar and O-polar heterostructures, respectively. On the experimental side, we have demonstrated high 2DEG concentrations near the plasmon-LO phonon resonance ( $\sim 7 \times 10^{12} \text{ cm}^{-2}$ ) in BeMgZnO/ZnO heterostructures with moderate Mg content and a small amount of Be. Achieving the same 2DEG concentrations in MgZnO/ZnO heterostructures would require incorporation of much higher Mg content (>40%) by using very low growth temperature, which leads to inferior material quality and poor device performance. Operation near or at the plasmon-

LO phonon resonance leads to short LO phonon lifetimes which in turn enhance carrier velocities needed for field effect transistors.

We explored Ag Schottky diode on quaternary BeMgZnO alloys and obtained a Schottky barrier height,  $\Phi_B = 1.07$  eV with an ideality factor  $n=1.22$  for a Ag/Be<sub>0.02</sub>Mg<sub>0.26</sub>ZnO Schottky diodes.

The temperature-dependent electrical characteristics of the Ag/Be<sub>0.02</sub>Mg<sub>0.26</sub>ZnO/ZnO heterostructure were studied by using temperature dependent current-voltage (I-V) measurements in the temperature range of 80-457 K. Richardson constant value of  $34 \text{ Acm}^{-2}\text{K}^{-2}$  was found experimentally which is close to the theoretical value of  $36 \text{ Acm}^{-2}\text{K}^{-2}$  known for Be<sub>0.02</sub>Mg<sub>0.26</sub>ZnO alloy.

## List of Reference

- <sup>1</sup> Ü. Özgür, Y.I. Alivov, C. Liu, A. Teke, M.A. Reshchikov, S. Doğan, V. Avrutin, S.-J. Cho, and H. Morkoç, *J. Appl. Phys.* **98**, 041301 (2005).
- <sup>2</sup> D.C. Look, *Mater. Sci. Eng. B* **80**, 383 (2001).
- <sup>3</sup> D.C. Look, D.C. Reynolds, J.W. Hemsky, R.L. Jones, and J.R. Sizelove, *Appl. Phys. Lett.* **75**, 811 (1999).
- <sup>4</sup> S.O. Kucheyev, J.S. Williams, C. Jagadish, J. Zou, C. Evans, A.J. Nelson, and A.V. Hamza, *Phys. Rev. B* **67**, 094115 (2003).
- <sup>5</sup> R.B. Green, M. Toporkov, M. d. b. Ullah, V. Avrutin, U. Ozgur, H. Morkoc, and E. Topsakal, *Microw. Opt. Technol. Lett.* **59**, 773 (2017).
- <sup>6</sup> E. Ohshima, H. Ogino, I. Niikura, K. Maeda, M. Sato, M. Ito, and T. Fukuda, *J. Cryst. Growth* **260**, 166 (2004).
- <sup>7</sup> J.-M. Ntep, S. Said Hassani, A. Lusson, A. Tromson-Carli, D. Ballutaud, G. Didier, and R. Triboulet, *J. Cryst. Growth* **207**, 30 (1999).
- <sup>8</sup> R.D. Vispute, V. Talyansky, S. Choopun, R.P. Sharma, T. Venkatesan, M. He, X. Tang, J.B. Halpern, M.G. Spencer, Y.X. Li, L.G. Salamanca-Riba, A.A. Iliadis, and K.A. Jones, *Appl. Phys. Lett.* **73**, 348 (1998).
- <sup>9</sup> K. Kobayashi, T. Matsubara, S. Matsushima, S. Shirakata, S. Isomura, and G. Okada, *Thin Solid Films* **266**, 106 (1995).
- <sup>10</sup> M. a. L. Johnson, S. Fujita, W.H. Rowland, W.C. Hughes, J.W. Cook, and J.F. Schetzina, *J. Electron. Mater.* **25**, 855 (1996).
- <sup>11</sup> P. Fons, K. Iwata, S. Niki, A. Yamada, and K. Matsubara, *J. Cryst. Growth* **201**, 627 (1999).
- <sup>12</sup> A. Ohtomo, K. Tamura, K. Saikusa, K. Takahashi, T. Makino, Y. Segawa, H. Koinuma, and M. Kawasaki, *Appl. Phys. Lett.* **75**, 2635 (1999).
- <sup>13</sup> Y. Chen, H.-J. Ko, S.-K. Hong, and T. Yao, *Appl. Phys. Lett.* **76**, 559 (2000).
- <sup>14</sup> M.B. Ullah, V. Avrutin, S.Q. Li, S. Das, M. Monavarian, M. Toporkov, Ü. Özgür, P. Ruterana, and H. Morkoç, *Phys. Status Solidi RRL – Rapid Res. Lett.* **10**, 682 (2016).
- <sup>15</sup> Y. Chen, D.M. Bagnall, H. Koh, K. Park, K. Hiraga, Z. Zhu, and T. Yao, *J. Appl. Phys.* **84**, 3912 (1998).
- <sup>16</sup> M. Sano, K. Miyamoto, H. Kato, and T. Yao, *Jpn. J. Appl. Phys.* **42**, L1050 (2003).
- <sup>17</sup> X. Du, M. Murakami, H. Iwaki, Y. Ishitani, and A. Yoshikawa, *Jpn. J. Appl. Phys.* **41**, L1043 (2002).
- <sup>18</sup> X. Wang, H. Iwaki, M. Murakami, X. Du, Y. Ishitani, and A. Yoshikawa, *Jpn. J. Appl. Phys.* **42**, L99 (2003).

- <sup>19</sup> S.-K. Hong, T. Hanada, H.-J. Ko, Y. Chen, T. Yao, D. Imai, K. Araki, and M. Shinohara, *Appl. Phys. Lett.* **77**, 3571 (2000).
- <sup>20</sup> S.-K. Hong, T. Hanada, H.-J. Ko, Y. Chen, T. Yao, D. Imai, K. Araki, M. Shinohara, K. Saitoh, and M. Terauchi, *Phys. Rev. B* **65**, 115331 (2002).
- <sup>21</sup> Y. Chen, D.M. Bagnall, Z. Zhu, T. Sekiuchi, K. Park, K. Hiraga, T. Yao, S. Koyama, M.Y. Shen, and T. Goto, *J. Cryst. Growth* **181**, 165 (1997).
- <sup>22</sup> S.O. Kucheyev, C. Jagadish, J.S. Williams, P.N.K. Deenapanray, M. Yano, K. Koike, S. Sasa, M. Inoue, and K. Ogata, *J. Appl. Phys.* **93**, 2972 (2003).
- <sup>23</sup> K. Nakahara, H. Takasu, P. Fons, K. Iwata, A. Yamada, K. Matsubara, R. Hunger, and S. Niki, *J. Cryst. Growth* **227**, 923 (2001).
- <sup>24</sup> K. Nakahara, T. Tanabe, H. Takasu, P. Fons, K. Iwata, A. Yamada, K. Matsubara, R. Hunger, and S. Niki, *Jpn. J. Appl. Phys.* **40**, 250 (2001).
- <sup>25</sup> H. Kato, M. Sano, K. Miyamoto, and T. Yao, *Jpn. J. Appl. Phys.* **42**, 2241 (2003).
- <sup>26</sup> V. Kirilyuk, A.R.A. Zauner, P.C.M. Christianen, J.L. Weyher, P.R. Hageman, and P.K. Larsen, *Appl. Phys. Lett.* **76**, 2355 (2000).
- <sup>27</sup> R. Dimitrov, M. Murphy, J. Smart, W. Schaff, J.R. Shealy, L.F. Eastman, O. Ambacher, and M. Stutzmann, *J. Appl. Phys.* **87**, 3375 (2000).
- <sup>28</sup> L.K. Li, M.J. Jurkovic, W.I. Wang, J.M. Van Hove, and P.P. Chow, *Appl. Phys. Lett.* **76**, 1740 (2000).
- <sup>29</sup> M. Sumiya, K. Yoshimura, K. Ohtsuka, and S. Fuke, *Appl. Phys. Lett.* **76**, 2098 (2000).
- <sup>30</sup> H. Kato, K. Miyamoto, M. Sano, and T. Yao, *Appl. Phys. Lett.* **84**, 4562 (2004).
- <sup>31</sup> K. Koike, K. Hama, I. Nakashima, G. Takada, K. Ogata, S. Sasa, M. Inoue, and M. Yano, *J. Cryst. Growth* **278**, 288 (2005).
- <sup>32</sup> D.M. Roessler, W.C. Walker, and E. Loh, *J. Phys. Chem. Solids* **30**, 157 (1969).
- <sup>33</sup> E.R. Segnit and A.E. Holland, *J. Am. Ceram. Soc.* **48**, 409 (1965).
- <sup>34</sup> A. Ohtomo, M. Kawasaki, T. Koida, K. Masubuchi, H. Koinuma, Y. Sakurai, Y. Yoshida, T. Yasuda, and Y. Segawa, *Appl. Phys. Lett.* **72**, 2466 (1998).
- <sup>35</sup> A.K. Sharma, J. Narayan, J.F. Muth, C.W. Teng, C. Jin, A. Kvit, R.M. Kolbas, and O.W. Holland, *Appl. Phys. Lett.* **75**, 3327 (1999).
- <sup>36</sup> X. Du, Z. Mei, Z. Liu, Y. Guo, T. Zhang, Y. Hou, Z. Zhang, Q. Xue, and A.Y. Kuznetsov, *Adv. Mater.* **21**, 4625 (2009).
- <sup>37</sup> Y.R. Ryu, T.S. Lee, J.A. Lubguban, A.B. Corman, H.W. White, J.H. Leem, M.S. Han, Y.S. Park, C.J. Youn, and W.J. Kim, *Appl. Phys. Lett.* **88**, 052103 (2006).
- <sup>38</sup> B. Cordero, V. Gómez, A.E. Platero-Prats, M. Revés, J. Echeverría, E. Cremades, F. Barragán, and S. Alvarez, *Dalton Trans.* 2832 (2008).
- <sup>39</sup> M. Chen, Y. Zhu, L. Su, Q. Zhang, A. Chen, X. Ji, R. Xiang, X. Gui, T. Wu, B. Pan, and Z. Tang, *Appl. Phys. Lett.* **102**, 202103 (2013).
- <sup>40</sup> L. Su, Y. Zhu, M. Chen, Q. Zhang, Y. Su, X. Ji, T. Wu, X. Gui, R. Xiang, and Z. Tang, *Appl. Phys. Lett.* **103**, 072104 (2013).
- <sup>41</sup> M. Toporkov, V. Avrutin, S. Okur, N. Izyumskaya, D. Demchenko, J. Volk, D.J. Smith, H. Morkoç, and Ü. Özgür, *J. Cryst. Growth* **402**, 60 (2014).
- <sup>42</sup> C. Yang, X.M. Li, Y.F. Gu, W.D. Yu, X.D. Gao, and Y.W. Zhang, *Appl. Phys. Lett.* **93**, 112114 (2008).
- <sup>43</sup> L. Su, Y. Zhu, Q. Zhang, M. Chen, X. Ji, T. Wu, X. Gui, B. Pan, Rong Xiang, and Z. Tang, *J. Phys. Appl. Phys.* **46**, 245103 (2013).
- <sup>44</sup> C. Yang, X.M. Li, X.D. Gao, X. Cao, R. Yang, and Y.Z. Li, *J. Cryst. Growth* **312**, 978 (2010).

- <sup>45</sup> J. Kolník, Ī.H. Oğuzman, K.F. Brennan, R. Wang, P.P. Ruden, and Y. Wang, *J. Appl. Phys.* **78**, 1033 (1995).
- <sup>46</sup> U.V. Bhapkar and M.S. Shur, *J. Appl. Phys.* **82**, 1649 (1997).
- <sup>47</sup> B.K. Ridley, *J. Appl. Phys.* **84**, 4020 (1998).
- <sup>48</sup> J.D. Albrecht, P.P. Ruden, S. Limpijumnong, W.R.L. Lambrecht, and K.F. Brennan, *J. Appl. Phys.* **86**, 6864 (1999).
- <sup>49</sup> A. Ohtomo, M. Kawasaki, I. Ohkubo, H. Koinuma, T. Yasuda, and Y. Segawa, *Appl. Phys. Lett.* **75**, 980 (1999).
- <sup>50</sup> M. Toporkov, D.O. Demchenko, Z. Zolnai, J. Volk, V. Avrutin, H. Morkoç, and Ü. Özgür, *J. Appl. Phys.* **119**, 095311 (2016).
- <sup>51</sup> R.M. Hazen and L.W. Finger, *J. Appl. Phys.* **59**, 3728 (1986).
- <sup>52</sup> H. Morkoç, *Handbook of Nitride Semiconductors and Devices, GaN-Based Optical and Electronic Devices*, Volume 3 edition (Wiley-VCH, Weinheim : Chichester, 2008).
- <sup>53</sup> H.A. Bethe, (1942).
- <sup>54</sup> R.T. Tung, *Mater. Sci. Eng. R Rep.* **35**, 1 (2001).
- <sup>55</sup> J.H. Werner and H.H. Güttler, *J. Appl. Phys.* **69**, 1522 (1991).
- <sup>56</sup> H. Kato, M. Sano, K. Miyamoto, and T. Yao, *J. Cryst. Growth* **275**, e2459 (2005).
- <sup>57</sup> S.K. Hong, H.J. Ko, Y. Chen, T. Hanada, and T. Yao, *J. Vac. Sci. Technol. B* **18**, 2313 (2000).
- <sup>58</sup> X. Wang, Y. Tomita, O.-H. Roh, M. Ohsugi, S.-B. Che, Y. Ishitani, and A. Yoshikawa, *Appl. Phys. Lett.* **86**, 011921 (2005).
- <sup>59</sup> A.N. Mariano and R.E. Hanneman, *J. Appl. Phys.* **34**, 384 (1963).
- <sup>60</sup> V. Potin, G. Nouet, and P. Ruterana, *Philos. Mag. A* **79**, 2899 (1999).
- <sup>61</sup> V. Potin, P. Ruterana, and G. Nouet, *J. Appl. Phys.* **82**, 2176 (1997).
- <sup>62</sup> J.E. Northrup, J. Neugebauer, and L.T. Romano, *Phys. Rev. Lett.* **77**, 103 (1996).
- <sup>63</sup> J.C. Kim and E. Goo, *J. Am. Ceram. Soc.* **73**, 877 (1990).
- <sup>64</sup> V. Potin, G. Nouet, and P. Ruterana, *Appl. Phys. Lett.* **74**, 947 (1999).
- <sup>65</sup> H. Karzel, W. Potzel, M. Köfferlein, W. Schiessl, M. Steiner, U. Hiller, G.M. Kalvius, D.W. Mitchell, T.P. Das, P. Blaha, K. Schwarz, and M.P. Pasternak, *Phys. Rev. B* **53**, 11425 (1996).
- <sup>66</sup> A. Waag, T. Gruber, K. Thonke, R. Sauer, R. Kling, C. Kirchner, and H. Röss, *J. Alloys Compd.* **371**, 77 (2004).
- <sup>67</sup> W.M. Yim and R.J. Paff, *J. Appl. Phys.* **45**, 1456 (1974).
- <sup>68</sup> S.J. Pearton, D.P. Norton, K. Ip, Y.W. Heo, and T. Steiner, *J. Vac. Sci. Technol. B* **22**, 932 (2004).
- <sup>69</sup> D.C. Look, J.W. Hemsky, and J.R. Sizelove, *Phys. Rev. Lett.* **82**, 2552 (1999).
- <sup>70</sup> S.B. Zhang, S.-H. Wei, and A. Zunger, *Phys. Rev. B* **63**, 075205 (2001).
- <sup>71</sup> L. Su, Y. Zhu, D. Yong, M. Chen, X. Ji, Y. Su, X. Gui, B. Pan, R. Xiang, and Z. Tang, *ACS Appl. Mater. Interfaces* **6**, 14152 (2014).
- <sup>72</sup> L. Su, Y. Zhu, Q. Zhang, M. Chen, T. Wu, X. Gui, B. Pan, R. Xiang, and Z. Tang, *Appl. Surf. Sci.* **274**, 341 (2013).
- <sup>73</sup> C. Yang, X.M. Li, W.D. Yu, X.D. Gao, X. Cao, and Y.Z. Li, *J. Phys. Appl. Phys.* **42**, 152002 (2009).
- <sup>74</sup> J.-H. Park, H.B. Cuong, S.-H. Jeong, and B.-T. Lee, *J. Alloys Compd.* **615**, 126 (2014).
- <sup>75</sup> M.B. Ullah, V. Avrutin, T. Nakagawara, S. Hafiz, I. Altuntaş, Ü. Özgür, and H. Morkoç, *J. Appl. Phys.* (2017).
- <sup>76</sup> H.Y. Lee, H.Y. Chang, L.R. Lou, and C.T. Lee, *IEEE Photonics Technol. Lett.* **25**, 1770 (2013).

- <sup>77</sup> R. Vettumperumal, S. Kalyanaraman, and R. Thangavel, *J. Sol-Gel Sci. Technol.* **68**, 334 (2013).
- <sup>78</sup> A. Matulionis, *Phys. Status Solidi A* **203**, 2313 (2006).
- <sup>79</sup> L. Ardaravičius, J. Liberis, O. Kiprijanović, A. Matulionis, M. Wu, and H. Morkoç, *Phys. Status Solidi RRL – Rapid Res. Lett.* **5**, 65 (2011).
- <sup>80</sup> A. Dyson and B.K. Ridley, *J. Appl. Phys.* **109**, 054509 (2011).
- <sup>81</sup> E. Šermukšnis, J. Liberis, M. Ramonas, A. Matulionis, M. Toporkov, H.Y. Liu, V. Avrutin, Ü. Özgür, and H. Morkoç, *J. Appl. Phys.* **117**, 065704 (2015).
- <sup>82</sup> A. Matulionis, J. Liberis, E. Šermukšnis, L. Ardaravičius, A. Šimukovič, C. Kayis, C.Y. Zhu, R. Ferreyra, V. Avrutin, Ü. Özgür, and H. Morkoç, *Microelectron. Reliab.* **52**, 2149 (2012).
- <sup>83</sup> A. Dyson and B.K. Ridley, *J. Appl. Phys.* **103**, 114507 (2008).
- <sup>84</sup> J.H. Leach, C.Y. Zhu, M. Wu, X. Ni, X. Li, J. Xie, Ü. Özgür, H. Morkoç, J. Liberis, E. Šermukšnis, A. Matulionis, T. Paskova, E. Preble, and K.R. Evans, *Appl. Phys. Lett.* **96**, 133505 (2010).
- <sup>85</sup> J. Falson, Y. Kozuka, J.H. Smet, T. Arima, A. Tsukazaki, and M. Kawasaki, *Appl. Phys. Lett.* **107**, 082102 (2015).
- <sup>86</sup> A. Tsukazaki, S. Akasaka, K. Nakahara, Y. Ohno, H. Ohno, D. Maryenko, A. Ohtomo, and M. Kawasaki, *Nat. Mater.* **9**, 889 (2010).
- <sup>87</sup> Y. Kozuka, A. Tsukazaki, and M. Kawasaki, *Appl. Phys. Rev.* **1**, 011303 (2014).
- <sup>88</sup> H. Tampo, H. Shibata, K. Maejima, A. Yamada, K. Matsubara, P. Fons, S. Kashiwaya, S. Niki, Y. Chiba, T. Wakamatsu, and H. Kanie, *Appl. Phys. Lett.* **93**, 202104 (2008).
- <sup>89</sup> O. Ambacher, J. Smart, J.R. Shealy, N.G. Weimann, K. Chu, M. Murphy, W.J. Schaff, L.F. Eastman, R. Dimitrov, L. Wittmer, M. Stutzmann, W. Rieger, and J. Hilsenbeck, *J. Appl. Phys.* **85**, 3222 (1999).
- <sup>90</sup> T. Hanada, in *Oxide Nitride Semicond.*, edited by P.T. Yao and P.D.S.-K. Hong (Springer Berlin Heidelberg, 2009), pp. 1–19.
- <sup>91</sup> H. Morkoç and Ü. Özgür, in *Zinc Oxide* (Wiley-VCH Verlag GmbH & Co. KGaA, 2009), pp. 1–76.
- <sup>92</sup> Q. Xu, X.-W. Zhang, W.-J. Fan, S.-S. Li, and J.-B. Xia, *Comput. Mater. Sci.* **44**, 72 (2008).
- <sup>93</sup> P. Gopal and N.A. Spaldin, *J. Electron. Mater.* **35**, 538 (2006).
- <sup>94</sup> S.-H. Jang and S.F. Chichibu, *J. Appl. Phys.* **112**, 073503 (2012).
- <sup>95</sup> M. Yano, K. Hashimoto, K. Fujimoto, K. Koike, S. Sasa, M. Inoue, Y. Uetsuji, T. Ohnishi, and K. Inaba, *J. Cryst. Growth* **301–302**, 353 (2007).
- <sup>96</sup> A. Tsukazaki, A. Ohtomo, T. Kita, Y. Ohno, H. Ohno, and M. Kawasaki, *Science* **315**, 1388 (2007).
- <sup>97</sup> J.D. Ye, S. Pannirselvam, S.T. Lim, J.F. Bi, X.W. Sun, G.Q. Lo, and K.L. Teo, *Appl. Phys. Lett.* **97**, 111908 (2010).
- <sup>98</sup> M.B. Ullah, M. Toporkov, V. Avrutin, Ü. Özgür, D.J. Smith, and H. Morkoç, in (2017), p. 101050J–101050J–14.
- <sup>99</sup> M.W. Allen, X. Weng, J.M. Redwing, K. Sarpatwari, S.E. Mohny, H. von Wenckstern, M. Grundmann, and S.M. Durbin, *IEEE Trans. Electron Devices* **56**, 2160 (2009).
- <sup>100</sup> S. Müller, H. von Wenckstern, F. Schmidt, D. Splith, R. Heinhold, M. Allen, and M. Grundmann, *J. Appl. Phys.* **116**, 194506 (2014).
- <sup>101</sup> R. Heinhold, G.T. Williams, S.P. Cooil, D.A. Evans, and M.W. Allen, *Phys. Rev. B* **88**, 235315 (2013).
- <sup>102</sup> L.J. Brillson and Y. Lu, *J. Appl. Phys.* **109**, 121301 (2011).

- <sup>103</sup> R.-H. Chang, K.-C. Yang, T.-H. Chen, L.-W. Lai, T.-H. Lee, S.-L. Yao, and D.-S. Liu, *J. Nanomater.* **2013**, e560542 (2013).
- <sup>104</sup> C.S. Singh, G. Agarwal, G. Durga Rao, S. Chaudhary, and R. Singh, *Mater. Sci. Semicond. Process.* **14**, 1 (2011).
- <sup>105</sup> S.K. Mohanta, A. Nakamura, G. Tabares, A. Hierro, Á. Guzmán, E. Muñoz, and J. Temmyo, *Thin Solid Films* **548**, 539 (2013).
- <sup>106</sup> S.K. Mohanta, A. Nakamura, G. Tabares, A. Hierro, Á. Guzmán, E. Muñoz, and J. Temmyo, *Thin Solid Films* **548**, 539 (2013).
- <sup>107</sup> R. Schifano, E.V. Monakhov, U. Grossner, and B.G. Svensson, *Appl. Phys. Lett.* **91**, 193507 (2007).
- <sup>108</sup> F.D. Aurret, S.A. Goodman, M. Hayes, M.J. Legodi, and H.A. van Laarhoven, *Appl. Phys. Lett.* **79**, 3074 (2001).
- <sup>109</sup> B.J. Coppa and R.F. Davis, *Appl. Phys. Lett.* **82**, 400 (2003).
- <sup>110</sup> N. Ohashi, J. Tanaka, T. Ohgaki, H. Haneda, M. Ozawa, and T. Tsurumi, *J. Mater. Res.* **17**, 1529 (2002).
- <sup>111</sup> A.Y. Polyakov, N.B. Smirnov, E.A. Kozhukhova, and V.I. Vdovin, *Appl. Phys. Lett.* **83**, 1575 (2003).
- <sup>112</sup> C.A. Mead, *Phys. Lett.* **18**, 218 (1965).
- <sup>113</sup> R.C. Neville and C.A. Mead, *J. Appl. Phys.* **41**, 3795 (1970).
- <sup>114</sup> S. Liang, H. Sheng, Y. Liu, Z. Huo, Y. Lu, and H. Shen, *J. Cryst. Growth* **225**, 110 (2001).
- <sup>115</sup> H. Sheng, S. Muthukumar, N.W. Emanetoglu, and Y. Lu, *Appl. Phys. Lett.* **80**, 2132 (2002).
- <sup>116</sup> J.C. Simpson and J.F. Cordaro, *J. Appl. Phys.* **63**, 1781 (1988).
- <sup>117</sup> S.V. Slobodchikov, K.M. Salikhov, E.V. Russu, and Y.G. Malinin, *Semiconductors* **35**, 464 (2001).
- <sup>118</sup> S.-H. Kim, H.-K. Kim, and T.-Y. Seong, *Appl. Phys. Lett.* **86**, 112101 (2005).
- <sup>119</sup> K. Ip, B.P. Gila, A.H. Onstine, E.S. Lambers, Y.W. Heo, K.H. Baik, D.P. Norton, and S.J. Pearton, *Appl. Phys. Lett.* **84**, 5133 (2004).
- <sup>120</sup> K. Ip, B.P. Gila, A.H. Onstine, E.S. Lambers, Y.W. Heo, K.H. Baik, D.P. Norton, S.J. Pearton, S. Kim, J.R. LaRoche, and F. Ren, *Appl. Surf. Sci.* **236**, 387 (2004).
- <sup>121</sup> K. Ip, Y.W. Heo, K.H. Baik, D.P. Norton, S.J. Pearton, S. Kim, J.R. LaRoche, and F. Ren, *Appl. Phys. Lett.* **84**, 2835 (2004).
- <sup>122</sup> N.R.C. Raju, K.J. Kumar, and A. Subrahmanyam, *J. Phys. Appl. Phys.* **42**, 135411 (2009).
- <sup>123</sup> S. Müller, H. von Wenckstern, F. Schmidt, D. Splith, R. Heinhold, M. Allen, and M. Grundmann, *J. Appl. Phys.* **116**, 194506 (2014).
- <sup>124</sup> M.W. Allen, S.M. Durbin, and J.B. Metson, *Appl. Phys. Lett.* **91**, 053512 (2007).
- <sup>125</sup> H. Kim, A. Sohn, and D.-W. Kim, *Semicond. Sci. Technol.* **27**, 035010 (2012).
- <sup>126</sup> M.W. Allen, X. Weng, J.M. Redwing, K. Sarpatwari, S.E. Mohny, H. von Wenckstern, M. Grundmann, and S.M. Durbin, *IEEE Trans. Electron Devices* **56**, 2160 (2009).
- <sup>127</sup> Q. Yan, P. Rinke, M. Winkelkemper, A. Qteish, D. Bimberg, M. Scheffler, and C.G. Van de Walle, *Appl. Phys. Lett.* **101**, 152105 (2012).
- <sup>128</sup> M.W. Allen, M.M. Alkai, and S.M. Durbin, *Appl. Phys. Lett.* **89**, 103520 (2006).
- <sup>129</sup> A. Lajn, H. von Wenckstern, M. Grundmann, G. Wagner, P. Barquinha, E. Fortunato, and R. Martins, *J. Appl. Phys.* **113**, 044511 (2013).
- <sup>130</sup> A. Ahaitouf, H. Srour, S.O.S. Hamady, N. Fressengeas, A. Ougazzaden, and J.P. Salvestrini, *Thin Solid Films* **522**, 345 (2012).
- <sup>131</sup> A. Tataroglu and Ş. Altındal, *Microelectron. Eng.* **85**, 233 (2008).

- <sup>132</sup> R.F. Schmitsdorf, T.U. Kampen, and W. Mönch, J. Vac. Sci. Technol. B Microelectron. Nanometer Struct. Process. Meas. Phenom. **15**, 1221 (1997).
- <sup>133</sup> F. Iucolano, F. Roccaforte, F. Giannazzo, and V. Raineri, J. Appl. Phys. **102**, 113701 (2007).
- <sup>134</sup> R.G. Sachs, Phys. Rev. **69**, 611 (1946).
- <sup>135</sup> C.O. Thomas, D. Kahng, and R.C. Manz, J. Electrochem. Soc. **109**, 1055 (1962).
- <sup>136</sup> H. Kroemer, W. Chien, J.S. Harris, and D.D. Edwall, Appl. Phys. Lett. **36**, 295 (1980).
- <sup>137</sup> A. Matulionis, Semicond. Sci. Technol. **28**, 074007 (2013).



## Vita

**Date of birth:** November 1, 1988

**Citizenship:** Bangladesh

### Education:

2017	Ph.D.	Electrical Engineering Virginia Commonwealth University
2011	B.Sc.	Electrical and Electronic Engineering Bangladesh University of Engineering and Technology

### Publication list (in chronological order):

Peer reviewed journal papers:

- [1] K. Ding, **M.B. Ullah**, V. Avrutin, Ü. Özgür, H. Morkoç, Investigation of high density two-dimensional electron gas in Zn-polar BeMgZnO/ZnO heterostructures, Appl. Phys. Lett. *In review*
- [2] **M.B. Ullah**, V. Avrutin, T. Nakagawara, S. Hafiz, I. Altuntaş, Ü. Özgür, H. Morkoç, Growth Kinetics of O-polar  $\text{Be}_x\text{Mg}_y\text{Zn}_{1-x-y}\text{O}$  Alloy: Role of Zn to Be and Mg Flux Ratio as a Guide to Growth at High Temperature, Journal of App phys, 121, (2017) 185704 (2017)
- [3] M. Toporkov, **M.B. Ullah**, D. Demchenko, V. Avrutin, H. Morkoç, Ü. Özgür, Effect of oxygen-to-metal ratio on incorporation of metal species into quaternary BeMgZnO alloy grown by plasma assisted molecular beam epitaxy on (0001)-Sapphire, Journal of crys growth, 467 (2017) 145-149

- [4] N. Lewinski, V. Avrutin, T. Izadi, **B. Ullah**, U. Ozgur, H. Morkoc, E. Topsakal, Cytocompatibility of ZnO Epitaxial Thin Films, Toxicology Letters. (2017), *Under review*
- [5] R. Green, M. Toporkov, **M.B. Ullah**, V. Avrutin, U. Ozgur, H. Morkoc, E. Topsakal, An Alternative Material for Transparent Antennas for Commercial and Medical Applications, Microwave and Optical Technology Letters, 59, (2017),773-777
- [6] **M.B. Ullah**, V. Avrutin, S.Q. Li, S. Das, M. Monavarian, M. Toporkov, Ü. Özgür, P. Ruterana, H. Morkoç, Polarity control and residual strain in ZnO epilayers grown by molecular beam epitaxy on (0001) GaN/sapphire, Phys. Stat. Sol. (RRL). 10 (2016) 682–686. **Featured in Phys. Status Solidi RRL 9/2016.**

Peer reviewed conference papers:

- [1] **M.B. Ullah**, M. Toporkov, V. Avrutin, U. Ozgur, D.J. Smith, H. Morkoc, Quaternary BeMgZnO by plasma-enhanced molecular beam epitaxy for BeMgZnO/ZnO heterostructure devices, in SPIE: 2017: pp, 101050J-101050J-14
- [2] M. Toporkov, **M.B. Ullah**, S. Hafiz, T. Nakagawara, V. Avrutin, H. Morkoc, U. Ozgur, Exciton localization and large Stokes shift in quaternary BeMgZnO grown by molecular beam epitaxy, in SPIE : 2016: pp. 974910-974910–12.